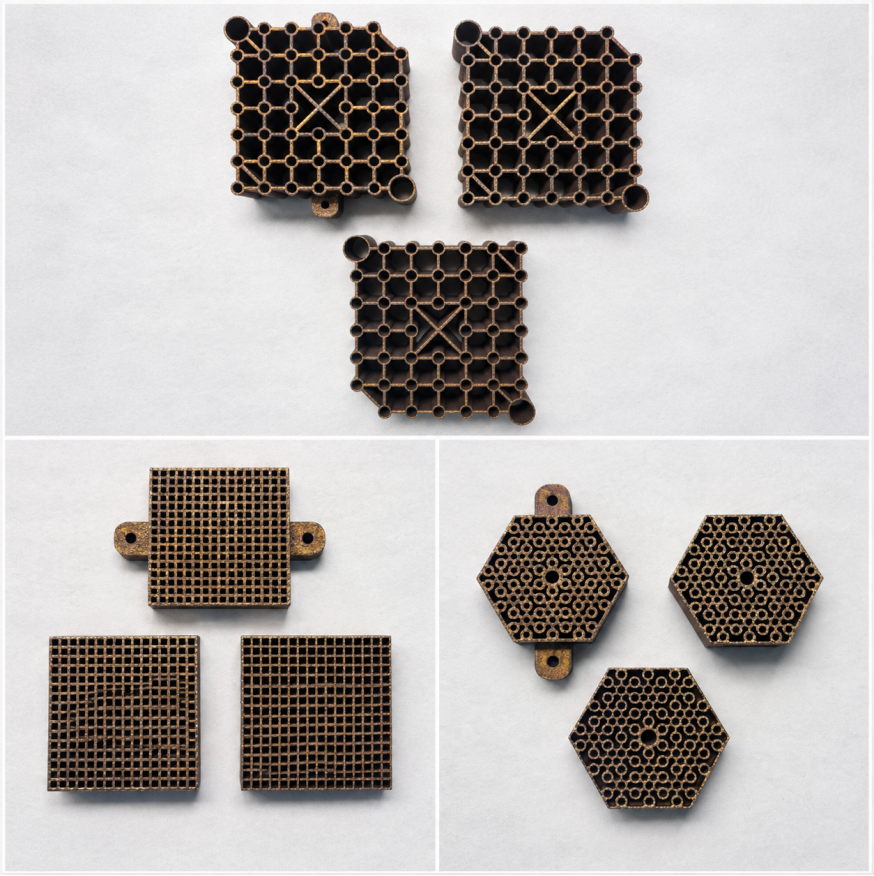
CHALMERS
UNIVERSITY OF TECHNOLOGY



Precision in Metal Additive Manufacturing Using Laser Powder Bed Fusion

Investigation of Process Parameters Influencing Dimensional Accuracy and Surface Quality

Master's thesis in Product Development

NOBLE JOSEY

DEPARTMENT OF INDUSTRIAL AND MATERIALS SCIENCE
CHALMERS UNIVERSITY OF TECHNOLOGY
Gothenburg, Sweden 2026
www.chalmers.se

Master's thesis 2026

Precision in Metal Additive Manufacturing Using Laser Powder Bed Fusion

Investigation of Process Parameters Influencing Dimensional Accuracy and Surface Quality

NOBLE JOSEY



CHALMERS
UNIVERSITY OF TECHNOLOGY

Department of Industrial and Materials Science
Product Development
Chalmers University of Technology
Gothenburg, Sweden 2026

Precision in Metal Additive Manufacturing Using Laser Powder Bed Fusion
Investigation of Process Parameters Influencing Dimensional Accuracy and Surface Quality
NOBLE JOSEY

© NOBLE JOSEY, 2026.

Supervisor: Saeed Khademzadeh, RISE Research Institutes of Sweden
Examiner: Professor Lars Nyborg, Department of Industrial and Materials Science

Master's Thesis 2026
Department of Industrial and Materials Science
Chalmers University of Technology
SE-412 96 Gothenburg
Sweden
Telephone +46 31 772 1000

Cover: Image captured after Print 3, in which full sample geometries were printed with the baseline parameters.

Typeset in LaTeX
Printed by Chalmers Reproservice
Gothenburg, Sweden 2026

Precision in Metal Additive Manufacturing Using Laser Powder Bed Fusion
Investigation of Process Parameters Influencing Dimensional Accuracy and Surface Quality

Noble Josey
Department of Industrial and Materials Science
Chalmers University of Technology

Abstract

Laser Powder Bed Fusion (PBF-LB) is the most widespread metal additive manufacturing technology, enabling complex metallic components with high design freedom for high-precision applications. However, achieving sufficient dimensional accuracy and surface quality remains a challenge, particularly for geometrically sensitive features where the final geometry is strongly influenced by contour (border) scan tracks.

This thesis investigates the influence of contour-related process parameters, including contour laser power, scan speed, beam compensation, and number of border passes, on dimensional accuracy and side-skin surface characteristics in PBF-LB manufacturing of 316L stainless steel. Benchmark geometries and test coupons, based on features relevant to nuclear components, were used to represent the geometric conditions of interest to the targeted industrial application. The specimens were manufactured on an SLM 280 system at RISE (Research Institutes of Sweden). A tiered design of experiments approach was combined with dimensional and surface measurements, and statistical analysis to investigate how contour parameters and feature geometry govern the resulting deviation.

Beam compensation was the dominant factor, shifting dimensions by approximately ± 2 mm per mm of applied offset, with opposite effects on internal and external features. Contour scan speed was about four times weaker, and contour laser power was not significant within the tested range. The dimensional error remained constant -0.05 to -0.07 mm regardless of feature size, so the larger relative error on thinner walls reflects percentage scaling rather than a physical size effect. No single compensation value suited both feature classes, with suitable values ranging from 0.026 to 0.108 mm. Confocal measurements showed the same division, internal bore surfaces being rougher than external walls with mean S_a about 1.9 µm higher.

Overall, the results show that the effect of contour parameters depends strongly on feature geometry. The identified relationships and compensation guidelines provide a foundation for further process development within the ongoing industrial collaboration at RISE, as well as for subsequent validation and application to more complex and production-scale components.

Keywords: Laser Powder Bed Fusion, Additive Manufacturing, Dimensional Accuracy, Contour Parameters, Surface Quality, Beam Compensation, Design of Experiments, Process Optimisation.

Acknowledgements

I would like to express my sincere gratitude to my supervisor, Saeed Khademzadeh at RISE Research Institutes of Sweden, for his guidance and support throughout this project. His expertise in additive manufacturing and valuable insights greatly contributed to the experimental design and direction of this work. I am equally grateful to my examiner, Professor Lars Nyborg at the Department of Industrial and Materials Science, Chalmers University of Technology, for his constructive feedback and critical perspective throughout the project.

I am deeply grateful to all the colleagues and technical staff at RISE Research Institutes of Sweden who supported me throughout the experimental work. I would especially like to thank Melina da Silva for her administrative support and help in settling into the group; Stefan Ewaldsson for his guidance in build preparation and machine operation, and for training me in the SLM 280 system, the PBF-LB process and sample preparation; Johan Fast Berglund for training and support in confocal microscopy and surface measurements; and August Gasslander for his assistance with optical microscopy. I am also grateful to Arvid Svanberg and Mikael Eriksson for their support and guidance throughout the project. I would also like to acknowledge my fellow master's thesis students at RISE, Ronald Benny, Syed Ali, Mohamed Magdy and Uday Sai, for making the experience insightful and memorable.

At Chalmers, I would like to thank the Department of Industrial and Materials Science for their assistance with heat treatment and wire EDM cutting of the specimens for this project.

Finally, I would like to thank my family and friends for their encouragement and support throughout my studies at Chalmers.

Noble Josey, Gothenburg, 2026

List of Acronyms

Below is the list of acronyms used throughout this thesis, in alphabetical order:

AFM	Abrasive Flow Machining
AM	Additive Manufacturing
ASTM	American Society for Testing and Materials
BC	Beam Compensation (also denoted δ)
BWR	Boiling Water Reactor
CAD	Computer-Aided Design
CB	Cube Benchmark (geometry family identifier)
CCD	Central Composite Design
C_TW	Cross Thin Wall (geometry family identifier)
CT	Computed Tomography
CY	Cylinder (geometry family identifier)
DfAM	Design for Additive Manufacturing
DoE	Design of Experiments
EDM	Electrical Discharge Machining
HX	Hexagonal Porous Plate (geometry family identifier)
ID	Inner Diameter
ISO	International Organization for Standardization
LoF	Lack of Fit
LOM	Light Optical Microscopy
MD	Mid Diameter
OD	Outer Diameter
OH	Overhang (geometry family identifier)
PBF-LB	Laser Powder Bed Fusion
PWR	Pressurised Water Reactor
RISE	Research Institutes of Sweden
RMSE	Root Mean Square Error
RQ	Research Question
RSM	Response Surface Methodology
SD	Standard Deviation
SLM	Selective Laser Melting
SQ_F	Square Grid Filter (geometry family identifier)
TW	Thin Wall (geometry family identifier)
UT	Upper Tie Plate (geometry family identifier)
VED	Volumetric Energy Density

Nomenclature

Below is the nomenclature of process parameters, measured responses and statistical quantities that have been used throughout this thesis.

Process Parameters

P	Laser power (W). Subscript c denotes the contour (border) exposure
v	Laser scan speed (mm/s). Subscript c denotes the contour exposure
h	Hatch distance (mm)
t	Layer thickness (mm)
δ	Beam compensation (BC), inward offset of the laser path from the nominal CAD boundary (mm)
n_b	Number of border (contour) passes (–)
E_V	Volumetric energy density, $E_V = P/(v\,h\,t)$ (J/mm^3)
E_L	Linear energy density, $E_L = P/v$ (J/mm)
θ	Surface inclination angle measured from the build platform (°)

Measured Responses

d_{nom}	Nominal (CAD) dimension of a feature (mm)
d_{meas}	Measured dimension of the fabricated feature (mm)
Δ	Signed dimensional deviation, $\Delta = d_{meas} - d_{nom}$ (mm). Negative denotes undersize
$\Delta\%$	Signed relative deviation, $\Delta\% = 100\,\Delta/d_{nom}$ (%)
$\lvert\Delta\%\rvert$	Absolute relative deviation (%)
S_a	Arithmetic mean height of the scale-limited surface (µm), ISO 25178-2
S_z	Maximum height of the scale-limited surface (µm), ISO 25178-2
S_{10z}	Ten-point height of the scale-limited surface (µm), ISO 25178-2

S_{sk}	Skewness of the scale-limited surface (–), ISO 25178-2
S_q	Root mean square height of the scale-limited surface (µm), ISO 25178-2
S_{dr}	Developed interfacial area ratio (%), ISO 25178-2

Statistical Quantities

y	Modelled response
x_i	Coded level of factor i
β_0	Model intercept
β_i	Linear (main effect) coefficient of factor i
β_{ii}	Quadratic coefficient of factor i
β_{ij}	Two-factor interaction coefficient between factors i and j
ε	Residual error term
R^2	Coefficient of determination
R^2_{adj}	Adjusted coefficient of determination
s	Root mean square error of the fitted model (mm)
s_{pe}	Pure-error standard deviation estimated from centre-point replicates (mm)
p	Probability value of a statistical significance test
α	Significance level (set to 0.05 throughout)
r	Pearson correlation coefficient
n	Number of observations

Contents

List of Figures **xvii**

List of Tables **xix**

1 Introduction **1**
1.1 Background . . . 1
1.2 Problem description . . . 2
1.3 Objectives . . . 2
1.4 Scope and limitations . . . 3
1.5 Thesis structure . . . 4
1.6 Ethical considerations during documentation . . . 4

2 Literature Review **5**
2.1 Laser powder bed fusion process . . . 5
2.1.1 Scan regions: hatch, contour and down-skin . . . 6
2.1.2 Melt pool behaviour and melting regimes . . . 8
2.1.3 316L stainless steel in PBF-LB . . . 9
2.2 Surface roughness in PBF-LB . . . 9
2.2.1 Surface roughness mechanisms . . . 9
2.2.2 Side-skin roughness and contour parameter effects . . . 11
2.2.3 Surface metrology for additive manufacturing . . . 12
2.3 Dimensional accuracy in PBF-LB . . . 13
2.3.1 Sources of dimensional deviation . . . 13
2.3.2 Thin-wall dimensional behaviour . . . 14
2.3.3 Contour parameters and dimensional control . . . 14
2.4 Design for Additive Manufacturing: benchmark geometries for PBF-LB 15
2.5 Design of Experiments and process optimisation . . . 16
2.6 Nuclear fuel assembly applications . . . 17
2.7 Gaps identified in existing literature . . . 17

3 Methods **19**
3.1 Research methodology overview . . . 19
3.2 Baseline geometry characterisation . . . 21
3.2.1 Baseline parameter sets . . . 21
3.2.2 Implications for the Design of Experiments . . . 22
3.3 Material description . . . 22
3.4 Benchmark geometry design . . . 22

3.5 Design of Experiments . . . 27
3.5.1 Tiered allocation of experimental effort . . . 27
3.5.2 Factor selection and levels . . . 27
3.5.3 Response variables . . . 29
3.6 Build plate layout . . . 30
3.7 Build preparation . . . 30
3.8 Manufacturing procedure . . . 31
3.9 Post-processing . . . 34
3.10 Dimensional characterisation . . . 35
3.10.1 Feature grouping . . . 36
3.11 Surface characterisation . . . 36
3.11.1 Coverage limitation . . . 38
3.12 Statistical analysis . . . 39

4 Results **41**
4.1 Manufacturing observations . . . 41
4.2 Consolidated dataset and data integrity . . . 42
4.2.1 Design verification . . . 42
4.3 The dimensional error is a constant offset, not a scaling error . . . 43
4.4 Beam compensation is the controlling factor . . . 44
4.4.1 Pooled response across geometry families . . . 44
4.4.2 Feature class splits the response in two . . . 45
4.4.3 Compensation values and their reachability . . . 46
4.4.4 The unified relation: $\Delta = a \pm 2 \times \mathrm{BC}$ . . . 47
4.4.5 Zero-crossing beam compensation by feature class . . . 48
4.5 Scan speed, laser power and number of borders . . . 49
4.5.1 Contour scan speed . . . 49
4.5.2 Contour laser power . . . 50
4.5.3 Number of borders . . . 50
4.5.4 Curvature . . . 50
4.6 Where contour control ends: the cube benchmark . . . 51
4.7 Wall-to-wall uniformity is not controllable by contour parameters . . . 53
4.8 Process limit: bore closure . . . 54
4.9 Surface characterisation results . . . 55
4.9.1 Scope of the confocal dataset . . . 55
4.9.2 Vertical wall roughness and energy density dependence . . . 55
4.9.3 Internal versus external surface roughness . . . 57
4.9.4 Overhang surfaces . . . 59
4.10 Summary of verified results . . . 60
4.11 Gaps in the current dataset . . . 60

5 Discussion **63**
5.1 Central observation: approximately constant offset . . . 63
5.2 Response depends on feature class more than feature size . . . 64
5.2.1 Why a slope of 2 makes sense . . . 64
5.2.2 The practical conflict . . . 65
5.2.3 Evidence from an independent measurement approach . . . 66

5.3 Feature range where contour optimisation can be relevant 66
5.4 Residual geometric dependence 67
5.5 Parameter hierarchy exhibited in the results 68
5.5.1 Scan speed 68
5.5.2 Laser power 69
5.5.3 Number of borders 69
5.5.4 Curvature 70
5.6 Limitation of contour optimisation 70
5.7 Surface quality 71
5.7.1 Overhang down-skin surfaces 71
5.7.2 Thin-wall and upper tie plate surfaces 71
5.7.3 Context within the literature 72
5.8 Process design guidelines 72
5.8.1 Compensation for external features 72
5.8.2 Compensation for internal features 73
5.8.3 Surface finish guidelines 74
5.8.4 Recommended starting range for parameters 75
5.8.5 Implications for nuclear industry components 76
5.9 Limitations of the current study 77

6 Conclusion **79**
6.1 RQ1: Which border scanning parameters most strongly influence dimensional accuracy and surface quality on precision-critical PBF-LB geometries? 79
6.2 RQ2: How do these parameters affect geometric and surface quality for different features? 80
6.3 RQ3: Can response surface modelling identify contour process windows that satisfy dimensional accuracy requirements, and what surface-quality constraints apply within those windows? 81
6.4 Principal contributions 81
6.5 Validity envelope 82

7 Future Work **83**
7.1 Extending the current analysis 83
7.2 Confirmation builds 84
7.3 Extending the parameter space 84
7.4 Addressing process uniformity 84
7.5 Beyond dimensional and surface characterisation 85

Bibliography **87**

A Baseline characterisation data **I**
A.1 Baseline characterisation I
A.1.1 Geometries characterised I
A.1.2 Dimensional accuracy findings I
A.1.3 Surface quality findings II

B DoE measurement data and fitted models V
B.1 Fitted model summary V
B.2 Measurement data from the DoE print VI
B.2.1 Cube benchmark: absence of contour response VI
B.2.2 Upper tie plate (UT) VI
B.2.3 Square grid filter (SQ_F) VII
B.2.4 Thin walls (TW) VII
B.2.5 Cross walls (C_TW) VIII
B.2.6 Cube benchmark (CB) IX
B.2.7 Cylinder matrix (CY) X
B.2.8 Confocal surface measurement data XI

List of Figures

2.1 Schematic of the PBF-LB process (not to scale). 6
2.2 The down-skin region. (a) Cross-sectional schematic of down-skin formation. (b) Illustration of down-skin heat conduction. 7
2.3 Exposure regions of a single layer. (a) Cross-sectional view of the different scan regions in an ideal part with multiple borders. (b) Beam compensation δ shifts the contour track inward so that the melt pool edge, rather than its centre, lies on the CAD boundary. . . 7
2.4 Illustration of stair-stepping for an inclined and a vertical surface. . . 10
2.5 Side-skin formation schematic. (a) Below the dross threshold, consolidated tracks carry adhered, partially melted particles. (b) At excessive contour energy, wider, unstable melt tracks and dross dominate. . 11
2.6 As wall thickness falls, the hatch region shrinks until the thinnest walls are built entirely from border tracks, making them the most direct probe of contour parameters. 14
2.7 Increasing BC moves the contour path towards the solid on both sides of a feature, so (a) walls shrink and (b) bores grow. 15

3.1 Overall experimental workflow. 20
3.2 Upper tie plate-inspired geometries. 24
3.3 Square grid filter-inspired geometries. 24
3.4 DoE test coupon TW. 25
3.5 DoE test coupon C_TW. 25
3.6 DoE test coupon CY. 25
3.7 DoE test coupon OH. 26
3.8 DoE test coupon set CB. 26
3.9 Full geometry HX. 27
3.10 Build plate layout for Print 2, showing the seven DoE zones, part placement and the rear-to-front gas flow direction within the SLM 280 chamber. 30
3.11 SLM 280 PBF-LB machine used for the experimental builds. 31
3.12 Close-up of failed geometries (Print 1). 32
3.13 Build plate with failed parts (Print 1). 32
3.14 Successfully fabricated DoE coupons on the build plate in the as-printed condition (Print 2). 33
3.15 Full-scale geometries for the post-processing study on the build plate (Print 3). 34

3.16 LOM set-up: (a) Leica M205 C during calibration; (b) screenshot of annotation performed in the Leica software. 35
3.17 Confocal microscopy set-up used in the experiments. 37
3.18 An example of report generation in MountainsMap. 38

4.1 Thin-wall measurements shown in two ways. (a) Signed deviation remains nearly constant across wall thickness. (b) The same deviation appears larger as a percentage for thinner walls. The orange curve shows the expected percentage error for a constant absolute deviation. 44
4.2 Feature-class cancellation on the square grid filter 46
4.3 Beam compensation slopes (signed Δ per mm of BC) for all nine dimensional responses. External features (walls, outer diameters) cluster around a mean slope of -1.93; internal features (bores, pores) cluster around $+1.67$. The dashed lines indicate the theoretical expectation of ± 2. 48
4.4 Zero-crossing beam compensation values by feature class, ordered from smallest to largest. 49
4.5 Factor effect sizes against the noise floor. 51
4.6 Wall-to-wall uniformity in the upper tie plate. (a) Each line spans the five wall deviations of one run; the lines shift down with compensation but keep the same length. (b) Within-run range against compensation. 53
4.7 Surface roughness (S_a) of the five TW samples grouped by contour linear energy density. 56
4.8 Paired comparison of wall and bore surfaces 58

List of Tables

3.1 Parameter sets used for the baseline print. 21
3.2 Benchmark geometry families and their identifiers. 23
3.3 Design of experiments by geometry family. All designs are orthogonal, with a largest absolute pairwise factor correlation of 0.000 in every case. 28
3.4 Dimensional response variables by geometry family, and the feature group assigned for analysis. 36

4.1 Consolidated dataset: runs, factors and measurement counts by geometry family. 42
4.2 Mean signed deviation and mean absolute relative deviation by nominal wall thickness, thin-wall family. The deviation in millimetres is essentially constant; the percentage deviation is not. 43
4.3 Mean signed deviation (mm) by beam compensation level, pooled across all other factors, for the thin-wall, cross-wall and upper tie plate families. 44
4.4 Beam compensation slope by feature class, upper tie plate family. Slopes are signed Δ in mm per mm of applied compensation. 45
4.5 Beam compensation required for zero signed deviation, by feature class and number of borders, evaluated at 150 W and 350 mm/s. The tested range was 0.04–0.10 mm. 46
4.6 Beam compensation value at zero mean deviation for each feature class, computed from the per-geometry linear fits. Values are for the centre-point conditions (150 W, 350 mm/s) where applicable. 49
4.7 Cube benchmark: measured deviation by feature class and outcome of the fitted contour model. 52
4.8 Overview of confocal surface measurements acquired across three geometry families. 55
4.9 Per-sample averages of confocal surface parameters on the TW vertical wall faces (each value is the mean of six individual wall measurements on that sample). 56
4.10 Paired comparison of bore (internal) and wall (external) surfaces measured on the same five upper tie plate coupons. p-values from paired t-tests, $n = 5$. 57

4.11 Confocal surface measurements on the eleven overhang down-skin specimens, with the down-skin border settings of each. All values in µm except S_{sk} (dimensionless). Specimens marked † are the centre-point replicates. 59

5.1 Compensation guidelines for external features. 73
5.2 Compensation guidelines for internal features 74
5.3 Surface finish guidelines by surface type 75

A.1 Baseline thin-wall surface roughness (mean values from stitched confocal measurements). II

B.1 Summary of fitted dimensional models. V
B.2 Upper tie plate: factor settings and measured bore diameters (mm). . VI
B.3 Upper tie plate: factor settings and measured wall thicknesses (mm). VII
B.4 Square grid filter: factor settings and measured pore and wall dimensions (mm). VII
B.5 Thin walls: factor settings and measured thicknesses (mm), walls A–C (nominal 0.5, 0.7, 0.9 mm). VIII
B.6 Thin walls: factor settings and measured thicknesses (mm), walls D–F (nominal 1.1, 1.3, 1.5 mm). VIII
B.7 Cross walls: factor settings and measured thicknesses (mm), nominal 0.5, 0.7, 0.9 mm. Four measurements per wall. IX
B.8 Cross walls: factor settings and measured thicknesses (mm), nominal 1.1, 1.3, 1.5 mm. Four measurements per wall. IX
B.9 Cube benchmark: factor settings and measured dimensions (mm), steps and holes. IX
B.10 Cube benchmark: factor settings and measured dimensions (mm), notches and slot lengths. IX
B.11 Cube benchmark: factor settings and measured dimensions (mm), bores and fillets. X
B.12 Cylinder matrix: factor settings and measured outer and inner diameters (mm). X
B.13 Overhang struts: down-skin border parameters. XI
B.14 Upper tie plate: confocal areal surface parameters, with the factor settings of each measured run. XI
B.15 Thin walls: confocal areal surface parameters for each of the six wall thicknesses on five measured coupons. XI
B.16 Overhang struts: confocal areal surface parameters on the down-skin surface. XII

1

Introduction

1.1 Background

PBF-LB has established itself as one of the most industrially significant metal additive manufacturing technologies, enabling fabrication of near-net-shape metallic components with high geometric complexity directly from digital CAD models [2, 3]. The process operates by selectively melting thin layers of metallic powder using a focused laser beam, with each layer built upon the previous one until the complete component is formed. PBF-LB offers substantial advantages over conventional manufacturing in terms of design freedom, material efficiency, and the ability to produce geometries such as internal channels, lattice structures, and thin-walled features that are difficult or impossible to achieve through subtractive methods [8, 9].

Despite these capabilities, dimensional accuracy and surface quality remain persistent challenges that limit the adoption of PBF-LB for precision-critical applications [4, 7]. PBF-LB manufactured components typically exhibit higher surface roughness than conventionally machined parts due to partially melted powder adhesion, stair-stepping effects, and melt pool instability [18, 20]. Dimensional deviations from the nominal CAD geometry arise from thermal shrinkage, residual stress accumulation, melt pool spreading, and beam offset inaccuracies [7, 2]. These effects become increasingly severe for thin-wall structures and geometrically sensitive features, where limited thermal mass and localised heat accumulation amplify process instability [34, 29].

The external geometry of a PBF-LB component is primarily defined by contour (border) scan tracks, which are the laser passes that trace the outer boundary of each sliced layer. While extensive research has addressed the influence of hatch parameters and volumetric energy density on bulk material properties, comparatively fewer studies have systematically investigated how border-specific parameters such as contour laser power, contour scan speed, beam compensation, and number of borders influence dimensional accuracy and surface morphology [10, 13, 15].

Recent industrial demonstrations of additively manufactured fuel assembly components, discussed in Section 2.6, establish the relevant feature scale for the targeted industrial study: mostly thin walls of a few hundred micrometres, at which the

process parameters governing geometric quality must be understood.

1.2 Problem description

Achieving dimensional accuracy and surface quality remains a challenge in PBF-LB, particularly for precision-sensitive geometries containing thin walls, small openings and other features with tight dimensional tolerances. Although PBF-LB process parameters can be adjusted to improve geometric accuracy, the resulting dimensional response is not necessarily linear across different feature geometries.

Therefore, in the industrial scenario considered in this project, where nuclear components are required to meet high standards of precision and quality in the as-printed condition, selecting process parameters that provide reliable geometric fidelity across a range of feature types presents a practical challenge. Contour-related parameters are particularly important because they directly influence the formation of the part boundary. However, the relationship between these parameters and the resulting dimensional accuracy is affected by the geometry being fabricated, making it difficult to define a single parameter setting that is suitable for all features.

Previous PBF-LB research has extensively investigated process parameter optimisation for bulk material properties and overall part quality [31, 40, 32], while contour-specific effects on dimensional accuracy across different feature geometries remain insufficiently understood, as highlighted by the four specific gaps reviewed in Section 2.7.

1.3 Objectives

The primary aim of the thesis is to improve the dimensional precision and surface quality of PBF-LB manufactured parts for 316L stainless steel while maintaining or improving productivity and build rate. The work therefore investigates how process parameters, especially border-related ones, can be used to improve the part quality of precision-critical components without compromising productivity. The resulting parameter-response relationships are further translated into quantified and applicable design guidelines to support a robust workflow for industrial PBF-LB applications.

The work also aims to address the following research questions:

1. Which border scanning parameters most strongly influence dimensional accuracy and surface quality on precision-critical PBF-LB geometries?
2. How do these parameters affect geometric and surface quality for different features?
3. Can response surface modelling identify contour process windows that satisfy dimensional accuracy requirements, and what surface-quality constraints apply within those windows?

To answer the identified research questions, the project was structured around the following objectives.

- Study the PBF-LB process and its relation to dimensional accuracy and surface roughness mechanisms, with particular focus on border parameter effects.
- Characterise baseline geometries printed with standard productivity and precision parameter sets to identify quality drivers and deviation trends.
- Design benchmark test geometries representative of precision-critical nuclear fuel assembly features, decomposed into isolated unit-cell-level specimens suitable for systematic evaluation, including a graded wall-thickness series capable of distinguishing a constant offset from a scaling error, and coupons carrying both internal and external features.
- Develop a tiered Design of Experiments methodology for border parameter investigation across geometries of varying complexity, with beam compensation treated as a primary factor rather than a fixed constant.
- Manufacture all benchmark geometries on an SLM 280 PBF-LB system with per-part border parameter assignment enabling all runs within a single build.
- Characterise dimensional deviation using optical measurement techniques and surface roughness using confocal microscopy (S_a, S_z, S_{10z}, S_{sk}), reporting signed deviation in absolute units throughout.
- Establish parameter-response relationships through response surface modelling to identify significant border parameters, interaction effects, and geometry-dependent behaviour, and verify model adequacy.
- Develop process guidelines for border parameter selection applicable to precision PBF-LB manufacturing of 316L stainless steel, stated with an explicit validity envelope.

1.4 Scope and limitations

This work focuses specifically on border scanning parameters (contour laser power, contour scan speed, beam compensation, and number of borders), while maintaining constant hatch, down-skin, and volume parameters across all experimental runs. This deliberate constraint isolates border parameter effects from hatch-related variability, enabling detailed attribution of measured responses to contour parameter changes. It also means that contour-hatch interaction, identified in the literature as governing the transition zone between the border-defined surface and the bulk fill [10], is outside the present scope.

The study is limited to fabrication of 316L stainless steel on an SLM 280 PBF-LB system, in line with the interests of RISE's industrial collaborators. While 316L was selected for its broad processing window and relevance to nuclear applications, the results may not directly transfer to other alloy systems with different thermal properties or melt pool behaviour.

The work investigates dimensional accuracy and surface quality as the primary re-

sponse variables. Mechanical testing (tensile, fatigue, fracture), detailed metallurgical investigation, porosity measurement, residual stress analysis and in-situ process monitoring are outside the scope of this thesis. Heat treatment and wire EDM are performed as part of the sample preparation workflow, but their effects on material properties are not systematically studied.

The benchmark geometries are unit-cell-level test features derived from nuclear fuel assembly components. While these features capture the manufacturing challenges of full-scale components, the results should be validated on complete component geometries before direct industrial implementation.

1.5 Thesis structure

The report is structured to present the project and its progression through the following sections:

Chapter 2 reviews PBF-LB process fundamentals, roughness and dimensional-accuracy mechanisms, and DoE methodology, concluding with the research gaps addressed. Chapter 3 describes the baseline characterisation that motivated the study, the benchmark geometry design, the tiered DoE, manufacturing and characterisation procedures. Chapters 4 and 5 present and discuss the results. Chapters 6 and 7 state the conclusions and the directions for further work.

1.6 Ethical considerations during documentation

This thesis was conducted in accordance with established principles of responsible research and research integrity, following the European Code of Conduct for Research Integrity [1].

AI tools were used in this thesis to support language refinement, proofreading, and clarity of written communication. The research design, experimental work, analysis, interpretation, and conclusions are entirely the author's own work.

2

Literature Review

This chapter reviews the established understanding of PBF-LB process fundamentals, surface roughness trends, dimensional accuracy challenges, and process optimisation methodologies relevant to the present work. The review focuses specifically on the influence of different process parameters, especially border scanning behaviour, as these form the basis of the experimental investigation described in Chapter 3. Section 2.7 draws the reviewed material together into the specific gaps that this thesis addresses.

2.1 Laser powder bed fusion process

Laser Powder Bed Fusion, designated PBF-LB/M in ISO/ASTM 52900 [44] and also referred to as Selective Laser Melting (SLM), is a metal additive manufacturing process in which a high-energy laser selectively melts thin layers of metallic powder according to sliced CAD data [2, 8]. A galvanometer scanner directs the laser over the powder bed; after each layer, the platform lowers by one layer thickness and the recoater spreads fresh powder across the build platform for subsequent laser scanning. The process repeats until the complete component is fabricated. A schematic of the process is shown in Figure 2.1.

PBF-LB has experienced rapid industrial growth over the past decade, driven by its capability for lightweight topology-optimised design, part consolidation, and mass customisation in aerospace, biomedical, automotive, and energy industries [2, 9]. Despite these advantages, several manufacturing challenges continue to limit its broader adoption, including dimensional inaccuracy, poor surface quality, residual stress accumulation, distortion, and process variability [4, 7]. These challenges become particularly critical for precision-sensitive components where even small geometric deviations may affect part functionality or assembly compatibility, or increase production cost compared with subtractive methods.

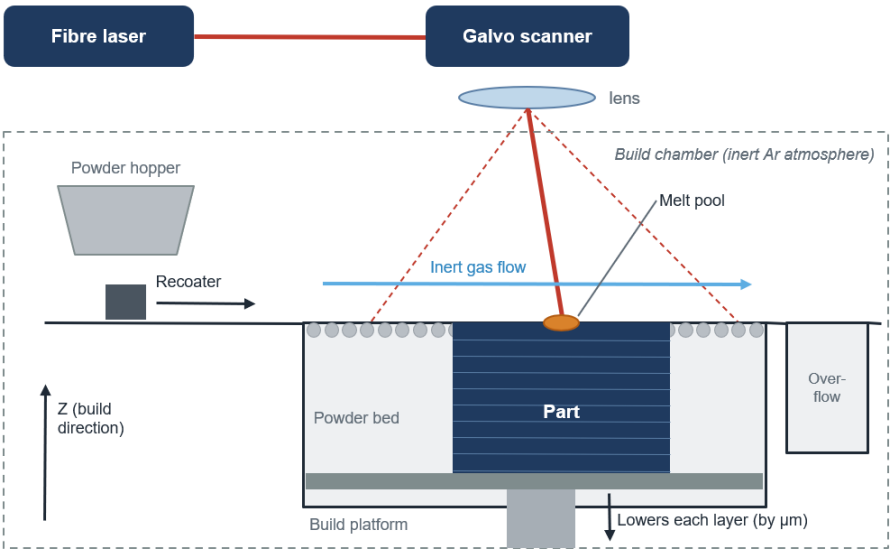


Figure 2.1: Schematic of the PBF-LB process (not to scale).

2.1.1 Scan regions: hatch, contour and down-skin

A single sliced layer is not exposed uniformly during scanning. Commercial PBF-LB systems divide each layer into distinct exposure regions, each with its own independently assignable parameter set. This can lead to different exposure times depending on the cross-section, and hence to varying structural integrity, with interacting effects when the whole part is consolidated. The *hatch* (or volume) region fills the interior of the cross-section with parallel scan vectors and governs bulk density and microstructure. The *contour* (or border) region consists of one or more passes tracing the outer boundary of the cross-section, and it is these passes that define the external geometry and the side-skin surface of the part, as seen in Figure 2.3. A *down-skin* region may additionally be defined for the first solidified layers above unsupported powder, especially for inclined features, as shown in Figure 2.2, and the *up-skin* region is the outermost top layer of a printed part.

The distinction matters for the present work because the hatch and border regions are scanned with different objectives. Hatch optimisation targets density, build rate and mechanical properties, and has been the overwhelming focus of the PBF-LB parameter literature [31, 40, 32]. Contour optimisation targets dimensional fidelity and surface finish, which are properties of the boundary rather than of the volume. A parameter set that produces excellent bulk density says nothing about whether the part is the right size, as the external geometry is mainly determined by the border scans.

Two border-specific parameters, beam compensation and number of borders, are highlighted here as the primary subjects of the DoE performed in this study. These are considered in addition to the commonly defined contour laser power and scan speed, which can be independently specified for border and hatch regions, resulting in different energy input and exposure conditions. The influence of beam compensation and number of borders on the resulting geometry is therefore investigated

alongside these conventional process parameters. *Beam compensation* (also termed beam offset or contour offset) is the inward displacement of the contour scan vector from the nominal CAD boundary, applied to account for the finite width of the melt pool: without it, the melt pool would straddle the CAD boundary and the part would be oversized by approximately one melt pool half-width on each side. The *number of borders* determines how many concentric contour passes are executed, and hence how far the contour-defined zone extends inward from the surface. For thin features, these two settings, together with the contour power and speed, can jointly determine the entire cross-section. An illustration of how these parameters are reflected in the printed geometry is shown in Figure 2.3.

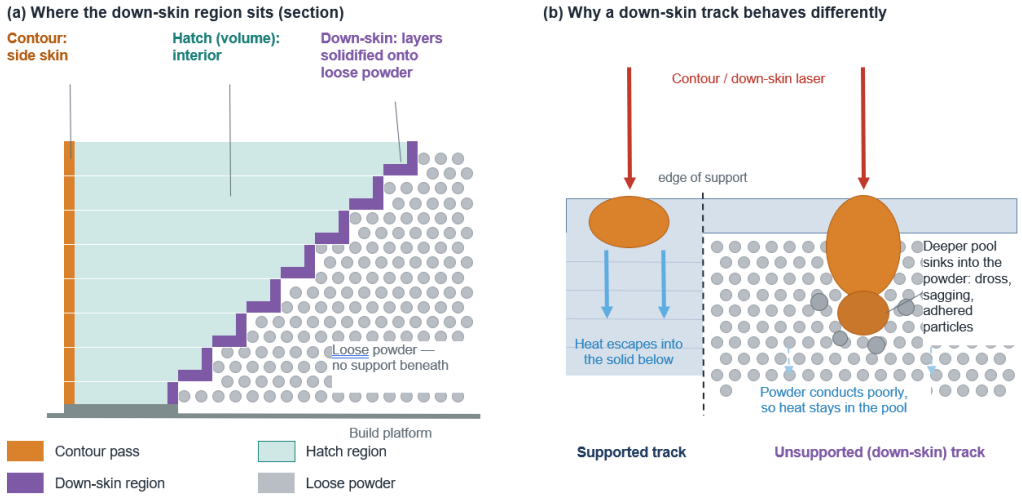


Figure 2.2: The down-skin region. (a) Cross-sectional schematic of down-skin formation. (b) Illustration of down-skin heat conduction.

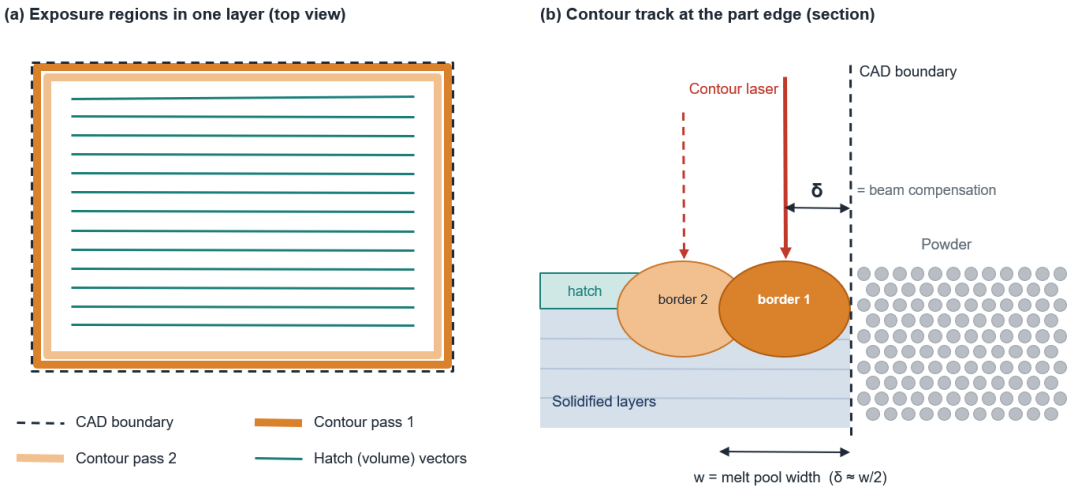


Figure 2.3: Exposure regions of a single layer. (a) Cross-sectional view of the different scan regions in an ideal part with multiple borders. (b) Beam compensation δ shifts the contour track inward so that the melt pool edge, rather than its centre, lies on the CAD boundary.

2.1.2 Melt pool behaviour and melting regimes

The PBF-LB process is governed by complex interactions between laser energy, powder particles, melt pool dynamics, and thermal transport phenomena [5]. When the laser scans the powder bed, energy is transferred at the point of contact, where the metallic powder absorbs thermal energy from the laser spot and undergoes rapid melting, forming a melt pool whose characteristics strongly determine the resulting dimensional accuracy, surface quality, and microstructure of the fabricated component.

The melt pool behaviour depends on many process parameters, including laser power, scan speed, hatch distance, layer thickness, and beam diameter. The interaction between these parameters determines the volumetric energy density (VED) supplied to the powder bed, commonly expressed as:

$$E_V = \frac{P}{v \cdot h \cdot t} \tag{2.1}$$

where P is the laser power (W), v is the scan speed (mm/s), h is the hatch distance (mm), and t is the layer thickness (mm) [31].

Equation 2.1 is, however, not the appropriate metric for contour scanning. A contour pass is a single track with no hatch spacing, so the meaningful energy metric is the linear energy density,

$$E_L = \frac{P}{v} \tag{2.2}$$

expressed in J/mm. This distinction is more than notational. Volumetric energy density is a grouped parameter that can be held constant by compensating changes in power and speed, yet the resulting melt pools differ [33]. For contour work, where a single track determines the boundary, the power-to-speed ratio and the resulting single-track width are the physically relevant quantities. The tested parameter ranges in this thesis are therefore reported mainly in terms of E_L, along with other parameters relevant to the specific geometry.

Three primary melting regimes are commonly identified in PBF-LB: conduction mode, transition mode, and keyhole mode melting [4]. Conduction mode is generally associated with stable melt pools and good dimensional accuracy, whereas keyhole mode introduces porosity and instability due to vaporisation-induced recoil pressure [5]. Zhang et al. [33] quantified this transition for 316L through single-track experiments, observing a shift from keyholing to conduction mode as scan speed increased at constant power. Two of their further findings bear directly on contour scanning: at constant linear energy density the melt pool dimensions still shrank with increasing scan speed while instability grew, and the presence of a powder layer amplified melt pool instability and surface irregularity through enhanced absorption. Because a contour track is exposed with powder on its outer side, the second observation is directly relevant to side-skin formation.

Melt pool width determines track overlap and bonding between adjacent tracks, while instabilities within the melt pool can lead to balling phenomena in which

molten tracks break into discontinuous beads due to surface tension effects [6]. Such phenomena also negatively affect surface quality and dimensional consistency, and on contour tracks they directly determine the external geometry of the component. Lack-of-fusion porosity arising from insufficient overlap has been modelled by Tang et al. [36] as a geometric consequence of melt pool dimensions relative to hatch spacing and layer thickness, and the same geometric reasoning applies to the placement of a contour track relative to the part boundary.

2.1.3 316L stainless steel in PBF-LB

316L stainless steel is widely used in PBF-LB due to its good weldability, corrosion resistance, and established processing behaviour [30, 31]. The material can achieve high density under suitable processing conditions and is therefore commonly used for process development and optimisation studies.

PBF-LB-processed 316L typically exhibits a fine cellular-dendritic microstructure resulting from rapid solidification, with elongated grains and crystallographic texture influenced by the local thermal history and scanning conditions [30, 31]. The thermal conditions can also vary with feature geometry, particularly near free surfaces and in thin sections [34, 35]. Such geometry-dependent thermal behaviour may influence melt pool characteristics and dimensional response.

The present work focuses on dimensional accuracy and surface topography rather than microstructural or porosity characterisation. Consequently, these aspects are not investigated experimentally but provide relevant background for understanding the process behaviour of 316L.

2.2 Surface roughness in PBF-LB

Surface roughness remains one of the major limitations of PBF-LB fabricated components. Compared to conventionally machined surfaces and other AM technologies, PBF-LB parts typically exhibit significantly higher roughness values due to the layer-wise fabrication mechanism and partially melted powder adhesion [18, 20].

2.2.1 Surface roughness mechanisms

The surface morphology of PBF-LB components is affected by multiple interacting factors including layer thickness, scan strategy, surface orientation, laser incidence angle, powder particle morphology, and border scanning parameters [18, 19]. Understanding these mechanisms is essential for contour-focused process optimisation because border tracks define the external surfaces of the component.

Stair-stepping: One of the dominant contributors to surface roughness on inclined surfaces is the stair-stepping effect caused by the layer-wise consolidation of material in the build direction (Z-axis). As shown in Figure 2.4, for a planar surface inclined at angle θ to the build platform and built from layers of thickness t, each layer

edge produces a right-triangular step whose altitude, measured perpendicular to the nominal inclined surface, is

$$R_t = t \cos\theta, \tag{2.3}$$

and since the resulting profile is approximately triangular, the arithmetic mean deviation is one quarter of the peak-to-valley height,

$$R_a = \frac{t \cos\theta}{4}. \tag{2.4}$$

These expressions give the correct limits: stair-stepping vanishes for a vertical wall ($\theta = 90°$), which is the orientation of every surface characterised in this work.

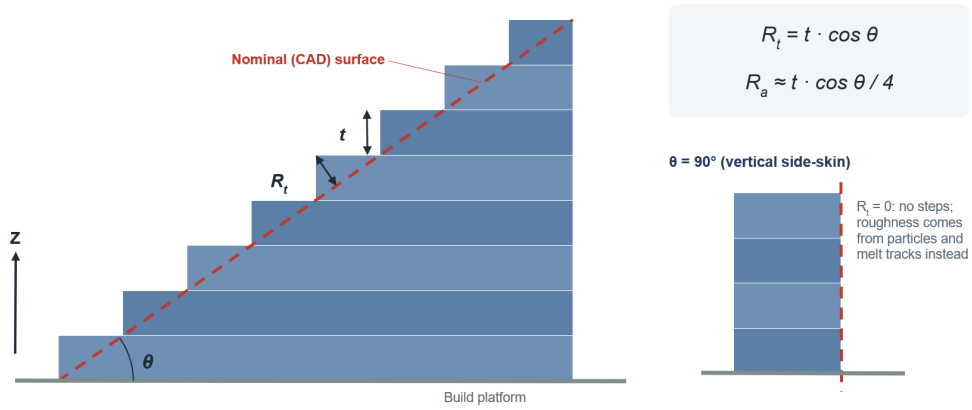


Figure 2.4: Illustration of stair-stepping for an inclined and a vertical surface.

Equations 2.3 and 2.4 describe an ideal geometric limit and consistently underestimate measured roughness, because they account for neither adhered particles nor melt track irregularity. Vu et al. [24] addressed these effects for 316L wall structures by decomposing surface roughness into contributions from the staircase effect, laser penetration into the underlying layer, and adhered powder particles. Their results showed that wall thickness had a negligible effect on surface characteristics over 1.5–5 mm, whereas slope angle was statistically significant for all measured characteristics. Comparable orientation-dependent models have also been developed for SLM by Strano et al. [18] and for AlSi10Mg by Boschetto et al. [19], both identifying build angle as among the strongest predictors of surface quality.

While these existing models predict roughness as a function of build angle, this study holds angle constant at standard support-free orientations and instead investigates how border scanning parameters influence surface quality at those fixed angles. This reflects the intended application: nuclear fuel assembly components that will be designed for AM with self-supporting geometries, making border parameter optimisation at fixed orientations the industrially relevant question.

Particle adhesion and spatter: Partially melted powder particles adhering to the solidified boundary are a second major contributor, and are the dominant one on vertical surfaces where stair-stepping is geometrically absent. During laser melting,

vaporisation of material generates recoil pressure that can eject molten droplets and powder particles away from the melt pool [5]; these spatters may subsequently reattach to the surface. Powder particles in the immediate vicinity of the melt track may also be partially sintered by conducted heat without being fully consolidated, and remain attached to the surface.

Fox et al. [22] showed that changes in surface roughness parameters, particularly peak count, mean spacing, and mean height, can help distinguish between surfaces dominated by partially melted particles and those dominated by re-solidified melt track material. These parameters can therefore provide an indication of the dominant surface formation mechanism. This distinction is important when interpreting the effect of process parameters, as the two mechanisms respond differently to changes in energy input. Increasing the energy density can reduce the adhesion of partially melted particles by promoting greater consolidation of the surrounding powder, while simultaneously increasing melt track irregularity and the formation of dross, as seen in Figure 2.5.

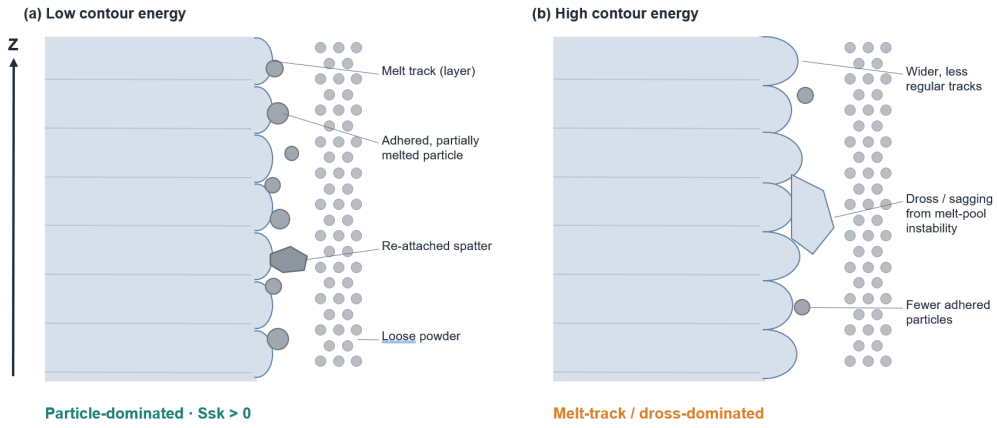


Figure 2.5: Side-skin formation schematic. (a) Below the dross threshold, consolidated tracks carry adhered, partially melted particles. (b) At excessive contour energy, wider, unstable melt tracks and dross dominate.

2.2.2 Side-skin roughness and contour parameter effects

Side-skin surfaces are the vertical faces of printed components and are of particular importance in precision applications because they are directly shaped by contour scanning parameters and because stair-stepping does not contribute to them.

Patel et al. [13] investigated side-skin surface characteristics in PBF-LB of Ti-6Al-4V and reported a robust correlation between both core and border parameters and side-skin surface morphology. Their key quantitative result is directly motivating for the present work: core power and velocity interactions gave S_a in the range 11–26 µm, whereas tuning the *border* parameters brought S_a below 10 µm with visibly reduced adhered and partially fused powder. Border parameters are therefore not a secondary refinement to hatch optimisation but the primary lever on side-skin finish. Zhang and Yuan [11] examined vertical surface roughness in 316L specifically and

identified an energy-density-dependent change in the dominant surface mechanism. At low contour energy density, of order 2 J/mm^2, roughness is dominated by solidified melt tracks and partially re-melted adhered particles; at high energy density, of order 5 J/mm^2, dross formation dominates. They proposed a multi-layer melt pool instability mechanism for dross on vertical, not merely down-facing, surfaces, and achieved S_a below 15 µm using low energy density and reduced laser power. In subsequent work, Zhang and Yuan [10] examined the interaction of contour and hatch parameters on vertical surface roughness. They found that under low-VED hatch conditions the contour offset distance has a negligible effect on vertical surface roughness provided the contour energy density remains below a threshold, while raising contour energy density triggers melt pool instability and dross that degrade the finish. They further demonstrated that a low contour energy density with an appropriate offset distance, combined with a contour-first scan strategy, effectively suppresses dross, so that side-skin roughness can be tuned largely independently of the hatch parameters. This result is one of the principal justifications for the experimental design adopted in this thesis, in which hatch parameters are deliberately held constant while contour parameters are varied.

Habeeb and Chou [15] investigated contour offset as a process variable for Ti6Al4V geometries with inclined slopes and found that its influence on surface roughness depended on surface orientation. Their results showed a trade-off between the surface quality of up- and down-facing surfaces, with partially melted particle accumulation remaining an important contributor to down-facing roughness. In subsequent work [16] the same authors reported lower surface roughness with post-contouring compared with pre-contouring, demonstrating that both contour parameters and scan ordering can influence surface topography.

An important caution against over-generalising contour rules comes from Glaubitz et al. [14], who examined contour parameters, melt pool behaviour and surface roughness across multiple PBF-LB platforms and two alloys. Unstable contour melt pools produced both the highest S_a and the greatest maximum valley depth. For IN718, increasing the stable contour melt pool width reduced roughness; for AlSi10Mg, melt pool width was not correlated with roughness at all. They concluded that melt pool width alone is an insufficient predictor of side-skin finish across alloys and platforms, which implies that contour parameter guidelines must be established per material and per machine rather than transferred.

Re-melting strategies offer a further route to improved side-skin quality. Yasa et al. [17] demonstrated that laser re-melting can improve density and surface quality by re-melting adhered particles and stabilising melt tracks, although at the cost of substantially increased build time; excessive re-melting energy may also increase thermal distortion, indicating that a balance must be found through systematic optimisation.

2.2.3 Surface metrology for additive manufacturing

Townsend et al. [20] provided a comprehensive review of surface texture metrology for metal additive manufacturing, emphasising that areal surface parameters

are considerably more representative of AM surface behaviour than traditional profile-based parameters. The argument is straightforward: AM surfaces are three-dimensional, spatially non-uniform and directionally anisotropic, so a single extracted profile samples an arbitrary line through a structured field and its parameters vary with the choice of line. Their review recommends confocal microscopy and focus-variation techniques for AM surface characterisation. The characterisation methodology adopted in the present thesis follows these recommendations.

The relevant areal parameters are defined in ISO 25178-2 [42]. Those used in this thesis are S_a, S_z, S_{10z} and S_{sk}, which are further discussed in Section 3.11.

Thompson et al. [21] describe ASTM F3624-23, which provides guidance on measuring and characterising PBF metal surface texture, including recommended measurement areas and filtering conditions, while ISO 25178-600 [43] and Leach [23] provide the broader framework for optical surface topography.

2.3 Dimensional accuracy in PBF-LB

Dimensional accuracy is a critical requirement for the industrial implementation of PBF-LB, particularly in applications such as aerospace, biomedical, and nuclear engineering where tight dimensional tolerances are required [25, 26]. The dimensional accuracy of a PBF-LB component is influenced by process parameters, thermal behaviour, material properties, and geometric characteristics.

2.3.1 Sources of dimensional deviation

Deviations from the nominal CAD geometry can arise from several interconnected sources, which can broadly be classified according to their dependence on feature size.

Size-dependent effects include thermal shrinkage during solidification and cooling, as well as residual-stress-induced distortion. Repeated thermal cycling during layer deposition can generate complex residual stress distributions and result in warping and geometric deviation [7]. Such effects are commonly addressed through global scaling corrections applied before slicing.

Other sources of dimensional deviation are associated more directly with boundary formation, including melt pool spreading beyond the intended scan path, beam offset, and adhesion of partially melted powder. These effects are typically addressed through local or feature-specific corrections.

This distinction is relevant to the present work because scaling and offset corrections address different sources of dimensional deviation. Reporting deviation relative to the nominal feature size may also obscure this distinction. The present study therefore evaluates signed dimensional deviation in absolute units to investigate how dimensional error varies with feature size and to assess the applicability of offset-based compensation.

2.3.2 Thin-wall dimensional behaviour

Thin-wall structures are particularly sensitive in terms of dimensional accuracy because a given dimensional deviation represents a larger proportion of a smaller feature, while their limited thermal mass and heat dissipation can also alter melt pool behaviour.

Wu et al. [27] investigated the fabrication limits of thin structures across Ti–6Al–4V, IN718, and AlSi10Mg and reported minimum wall thicknesses of approximately 100 µm under optimised design and processing conditions. Their work demonstrates the strong influence of geometry and process conditions on the manufacturability of thin features.

For 316L, López-García et al. [28] investigated straight walls and lattice struts across a range of feature sizes using optical microscopy, focus-variation microscopy, and micro-computed tomography. Their results showed increasing dimensional errors for smaller features, with substantially greater relative deviations observed for the thinnest walls and struts. These results provide a relevant comparison for the thin-wall series investigated in the present work.

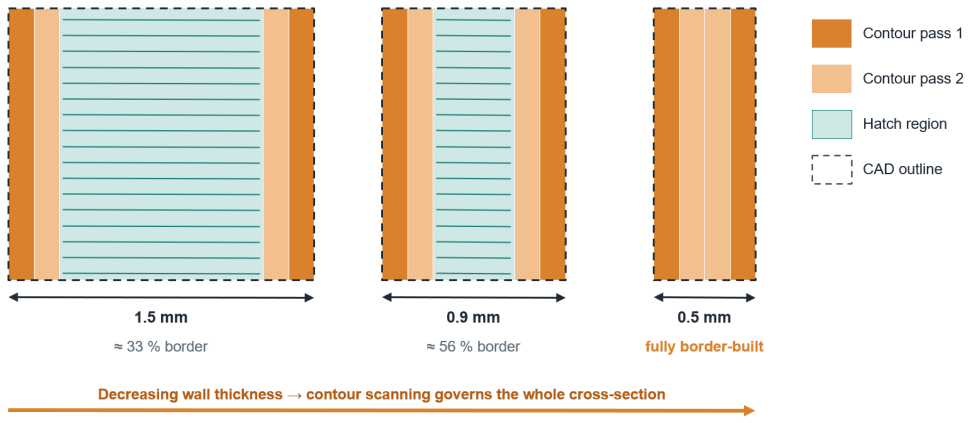


Figure 2.6: As wall thickness falls, the hatch region shrinks until the thinnest walls are built entirely from border tracks, making them the most direct probe of contour parameters.

Gaikwad et al. [29] highlighted the importance of the ratio between border and hatch scanning for thin-wall features. As wall thickness decreases, border scanning increasingly dominates the cross-section, and sufficiently thin features may be produced almost entirely from contour tracks. Thin walls therefore provide a suitable geometry for investigating the influence of border-specific process parameters, as illustrated in Figure 2.6.

2.3.3 Contour parameters and dimensional control

Zhang and Yuan [12] investigated the dimensional accuracy of thin-wall 316L geometries and reported that increasing contour laser power enlarged the melt pool and

promoted lateral melt pool migration, resulting in increased dimensional deviation and surface defects. They also showed that applying an inward contour offset could reduce the scanned region and improve dimensional accuracy.

Where compensation has been varied systematically, as by Habeeb and Chou [15], the response measured was surface roughness rather than dimensional deviation. Beam compensation therefore needs to be investigated against both responses.

The type of feature being measured is also important. Dimensional accuracy studies commonly focus on external features such as walls, struts, cylinders, and cubes. Since compensation affects internal and external boundaries in opposite geometric directions, as seen in Figure 2.7, evaluating both feature classes under identical process conditions is important when developing general compensation strategies.

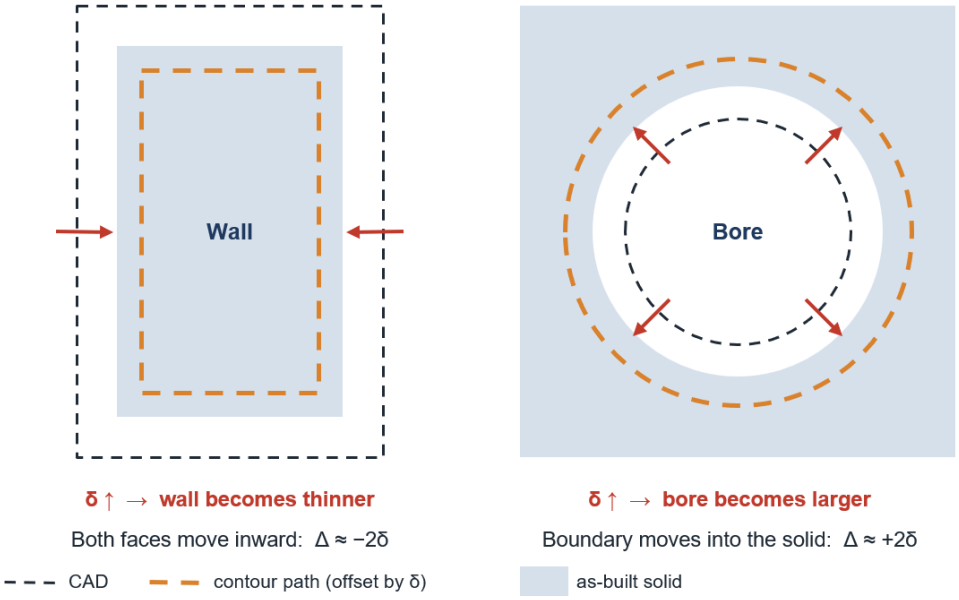


Figure 2.7: Increasing BC moves the contour path towards the solid on both sides of a feature, so (a) walls shrink and (b) bores grow.

2.4 Design for Additive Manufacturing: benchmark geometries for PBF-LB

Design for Additive Manufacturing (DfAM) involves adapting component geometry to exploit the capabilities of additive manufacturing while accounting for process limitations [8, 37].

Benchmark geometries are widely used to evaluate PBF-LB manufacturability and geometric capability. Maleki et al. [25] reviewed a range of benchmark features, including struts, lattice structures, thin walls, holes, internal channels, and bulk geometries, and highlighted that different feature types exhibit different manufacturing sensitivities. Gradl et al. [26] similarly demonstrated that parameter sets

suitable for bulk geometries do not necessarily provide adequate accuracy for thin or intricate features.

Thomas [37] developed design rules using benchmark features including thin walls, holes, cylinders, and overhangs, demonstrating their usefulness for evaluating process sensitivity across different geometric conditions. Standardised test artefacts for assessing the geometric capability of additive manufacturing systems are defined in ISO/ASTM 52902 [45], while ISO/ASTM 52911-1 [46] provides design guidance for laser-based powder bed fusion of metals.

These findings support the use of multiple representative geometries in the present study. The selected geometries are based on features relevant to the targeted nuclear fuel assembly application and are intended to represent different geometric conditions for evaluating the influence of contour process parameters on dimensional accuracy and surface characteristics. They also motivate the feature-specific approach adopted in the DoE, where different geometry classes are investigated for their sensitivity to contour parameters. As discussed in the literature, parameter sets optimised for bulk geometries do not necessarily provide adequate performance for thin sections or intricate features [26, 25].

2.5 Design of Experiments and process optimisation

PBF-LB involves multiple interacting process variables, making systematic experimental approaches important for understanding parameter-response relationships [38]. DoE enables several factors to be varied simultaneously while reducing the number of experiments compared with conventional one-factor-at-a-time approaches.

Response Surface Methodology (RSM) is widely used for process optimisation because it enables the effects of multiple continuous factors and their interactions to be modelled. Second-order models can capture both linear trends and curvature in the parameter-response relationship [39, 38].

Read et al. [40] demonstrated the application of DoE and response surface methods to PBF-LB process optimisation, establishing relationships between process parameters and material properties. Gajera et al. [41] also applied RSM to PBF-LB parameters for dimensional accuracy, but their study focused primarily on conventional bulk process parameters rather than contour-specific parameters. Therefore, a study applying a similar DoE approach specifically to contour parameters is required, because contour parameters can interact with each other and with feature geometry. The relationship between beam compensation and the parameters governing melt pool width, such as laser power and scan speed, is of particular interest because, as seen in the literature, changes in melt pool dimensions can alter the boundary position relative to the CAD geometry.

2.6 Nuclear fuel assembly applications

The industrial application motivating this work is the nuclear fuel assembly sector, with components such as upper tie plates, spacer grids, and debris filter plates. These components combine thin-walled, perforated, and lattice features with demanding dimensional requirements, making them relevant examples of precision-critical PBF-LB applications.

The geometric features of these components provide reference geometries for the present study. Rather than reproducing complete fuel assembly components, representative benchmark geometries are used to investigate process-geometry relationships under controlled experimental conditions.

Two industrial developments demonstrate the growing interest in metal additive manufacturing for this component class. In 2022, Framatome reported the installation of a fuel assembly containing 3D-printed stainless-steel ATRIUM 11 upper tie plate grids at Vattenfall's Forsmark 3 reactor [47, 48]. Separately, Westinghouse and Carnegie Mellon University demonstrated PBF-LB production of PWR spacer grids in Inconel 718 [49].

These developments illustrate the potential for additive manufacturing to produce complex fuel assembly geometries while also highlighting the importance of dimensional precision and surface quality. The present work addresses a subset of these challenges by investigating contour-related process parameters using representative benchmark geometries.

2.7 Gaps identified in existing literature

The literature reviewed above supports four specific gaps that the present work addresses.

1. Border parameters are under-studied. PBF-LB parameter optimisation is predominantly focused on hatch parameters and bulk properties, while the influence of contour parameters on dimensional accuracy remains less explored [31, 40, 32].
2. Beam compensation is rarely treated as a design factor. It is commonly fixed as a machine setting, leaving its relationship with other contour parameters insufficiently characterised.
3. Dimensional deviation is not consistently reported as a signed quantity. This makes it difficult to distinguish constant dimensional offsets from proportional scaling effects and to define appropriate compensation strategies.
4. Internal and external features are rarely evaluated together. Consequently, differences in their response to contour parameters and compensation remain insufficiently characterised.

This thesis addresses these gaps through a systematic investigation of relevant process parameters, geometric conditions, and feature types. The results provide a

basis for identifying process–geometry relationships and developing improved design guidelines for precision PBF-LB manufacturing.

3

Methods

3.1 Research methodology overview

The methodology adopted in this thesis was developed to systematically investigate the influence of border scanning parameters on dimensional accuracy and surface quality of precision-sensitive geometries manufactured by PBF-LB in 316L stainless steel.

The overall research approach consisted of several interconnected stages. Initially, a comprehensive literature review was conducted to establish the current understanding of PBF-LB process-property relationships, with particular emphasis on contour parameter effects, thin-wall fabrication behaviour, and surface roughness mechanisms. The findings from this review informed the selection of process parameters, geometry design, and experimental design methodology. Concurrently with the literature review, a set of baseline geometries was manufactured at RISE using the standard productivity (60 µm) and precision (30 µm) parameter sets provided by Nikon SLM Solutions, and was characterised for dimensional accuracy and surface quality. These findings motivated the investigation of border parameters at the 60 µm layer thickness, with the aim of improving precision while retaining the productivity advantages of the standard workflow.

The experimental work followed a sequential workflow designed around the DoE structure:

1. Literature review and identification of research gaps in border parameter optimisation.
2. Baseline characterisation of geometric deviation and surface roughness to identify representative features, establish reference values, and define suitable response ranges for the subsequent experiments.
3. Development of representative full-part geometries inspired by nuclear fuel assembly components, followed by decomposition into isolated test geometries and coupons for controlled investigation of contour process parameters.
4. Design of the DoE framework in JMP, including factor selection, level definition, and experimental run generation.

5. Build plate layout design with spatial zoning according to DoE type.
6. Build preparation in Materialise Magics, including part placement and support generation, with process parameter assignment through the SLM Build Processor.
7. PBF-LB manufacturing using the SLM 280 system.
8. Post-build processing, including powder removal, wire EDM sample separation, heat treatment, and sample preparation for surface characterisation.
9. Dimensional characterisation using light optical microscopy.
10. Surface roughness characterisation using confocal microscopy.
11. Consolidation and preparation of measurement data, followed by preliminary analysis in Excel to identify trends, assess dataset suitability, and prepare the data for statistical modelling.
12. Statistical analysis in JMP using response surface modelling to evaluate the influence of process parameters on dimensional accuracy and surface roughness.

The workflow was structured such that each manufactured specimen remained directly traceable to its corresponding DoE factor levels, enabling systematic parameter-response analysis. The overall experimental workflow is summarised in Figure 3.1. Detailed descriptions of the baseline characterisation, geometry development, DoE, manufacturing, characterisation, and statistical analysis are provided in the following sections.

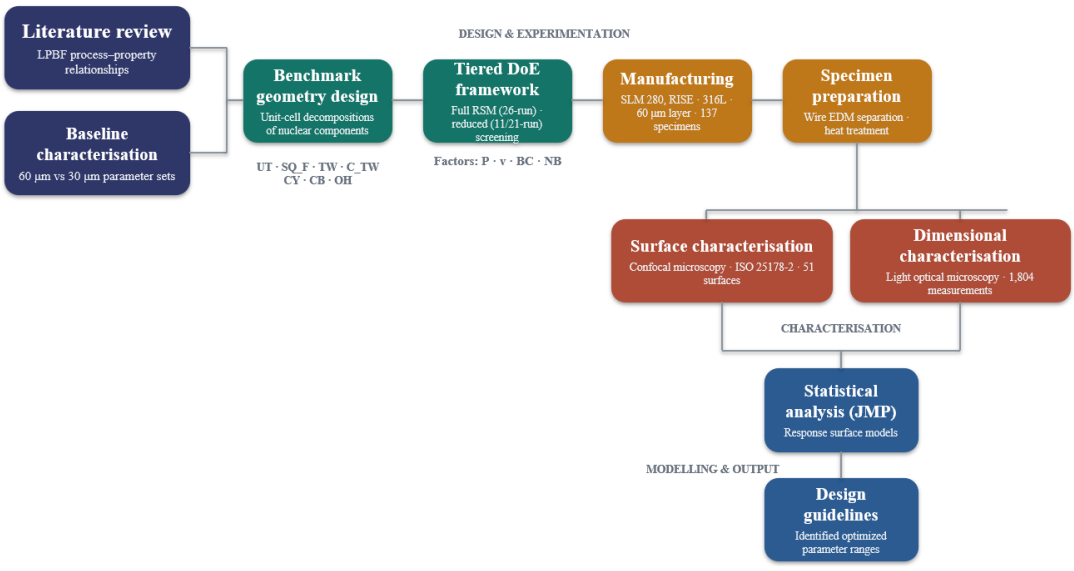


Figure 3.1: Overall experimental workflow.

3.2 Baseline geometry characterisation

Before the Design of Experiments campaign was undertaken, a baseline characterisation study was conducted on a set of test geometries that had been printed at RISE prior to the start of this thesis. The baseline specimens were manufactured from 316L stainless steel powder using an SLM 280 laser powder bed fusion system with a nominal build platform of 280 × 280 mm. Two workflows were compared: the productivity workflow (60 µm layer thickness) and the precision workflow (30 µm layer thickness). The purpose of this study was to compare dimensional accuracy and surface quality between the two workflows, identify which geometric features were most sensitive to process parameter differences, and determine where process optimisation could yield the greatest improvement.

3.2.1 Baseline parameter sets

Table 3.1 presents the two parameter sets used for the baseline print; both sets were included in the same build, with replicate specimens for comparison. The principal difference is the layer thickness: 60 µm for productivity and 30 µm for precision. The hatch parameters differ accordingly, with the productivity workflow using higher laser power (350 W vs 200 W) and higher scan speed (950 mm/s vs 800 mm/s) to maintain throughput at the thicker layer. Notably, the border parameters also differ: while both use 150 W border laser power and a single border pass, the border scan speed is 350 mm/s for productivity and 500 mm/s for precision, resulting in a higher linear energy density at the contour for the productivity workflow (0.43 J/mm vs 0.30 J/mm).

Table 3.1: Parameter sets used for the baseline print.

Parameter	Productivity	Precision
Layer thickness	60 µm	30 µm
Laser power — Hatch	350 W	200 W
Scan speed — Hatch	950 mm/s	800 mm/s
Hatch distance	0.12 mm	0.12 mm
Number of borders	1	1
Laser power — Border	150 W	150 W
Scan speed — Border	350 mm/s	500 mm/s
Linear energy density — Border	0.43 J/mm	0.30 J/mm
Volumetric energy density — Hatch	51 J/mm^3	69 J/mm^3
Beam compensation	0.07 mm	0.08 mm

Stress-relief heat treatment was performed at 350 °C for 2 hours. Following heat treatment, geometries were separated from the build plate by wire EDM and characterised for dimensional deviation and surface roughness. A detailed description of the baseline geometries, dimensional accuracy results, and surface characterisation findings is provided in Appendix A.

3.2.2 Implications for the Design of Experiments

The baseline characterisation study yielded three key findings that directly shaped the subsequent Design of Experiments campaign:

- Border-controlled dimensions are the primary source of geometric deviation. Width dimensions governed by the contour scan showed significantly larger errors than length dimensions governed by scan path length and hatch spacing. This confirmed that a DoE focused on border parameters, such as contour laser power, contour scan speed, beam compensation, and number of borders, would target the most impactful process variables, consistent with the literature review.
- The productivity workflow requires optimisation to achieve precision-grade quality. While the productivity parameter set offers shorter fabrication times through its thicker 60 µm layer, it produced higher extreme surface roughness and, for certain features, larger dimensional deviation than the precision workflow. Since industrial adoption favours the productivity workflow for its throughput advantage, optimising its border parameters to close the quality gap was identified as the primary objective for the DoE.
- Internal and external features respond in opposite directions to beam compensation. Thin walls (external features) were undersized while grooves (internal features) were oversized, and the magnitude of deviation differed between the two workflows. This observation motivated the feature-class split analysis adopted throughout Chapter 4, where internal and external responses are modelled separately rather than pooled.

3.3 Material description

Gas-atomised virgin 316L stainless steel powder was used as the feedstock material throughout the study. The powder was supplied for use with the Nikon SLM 280 system and exhibited a predominantly spherical particle morphology, supporting consistent powder flow and layer deposition. The 316L powder batch was specified for the industrial project and was of nuclear grade, intended for research on nuclear component applications. No powder selection, material optimisation, or mechanical property characterisation was within the scope of this work; the material and powder condition were kept constant throughout the experimental campaign.

3.4 Benchmark geometry design

The benchmark geometries used in this study were designed by decomposing nuclear fuel assembly components into isolated unit-cell-level test features. This approach enabled the measured responses (dimensional deviation and surface roughness) to be attributed more directly to individual DoE factor levels, which would be difficult to achieve using complex full-scale components where multiple geometric effects interact simultaneously.

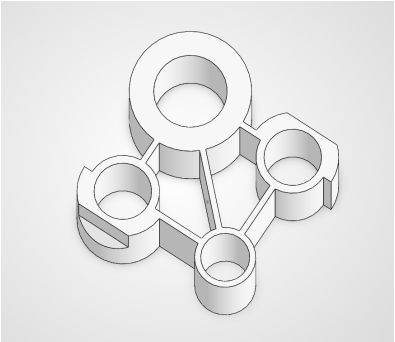
The initial design scope included full-scale versions of three customer-relevant geometries, namely an upper tie plate lattice, a hexagonal porous plate, and a square grid filter, alongside purpose-built test coupons. As the DoE and characterisation strategy were further developed, it was decided to allocate the full-scale geometries to a separate build (Print 3), with five replicates of each, for a post-processing surface treatment study within the broader industrial project but outside the scope of this thesis. For the DoE build, the upper tie plate and square grid filter were redesigned as compact unit-cell test coupons that retained the characteristic features of their respective full-scale parts, including struts, bores, node intersections, pores, webs, and corners, while remaining small enough to manufacture in the quantities required by the experimental design. The hexagonal porous plate was not included in the DoE because its dominant geometric features, namely cylindrical channels and thin plate walls, were already represented by the cylinder matrix, thin-wall, and unit-cell UT and SQ_F coupons.

The DoE geometry set comprised seven families, each selected to interrogate specific aspects of border parameter sensitivity; the hexagonal porous plate (HX) is included in Table 3.2 for completeness but was built only in Print 3.

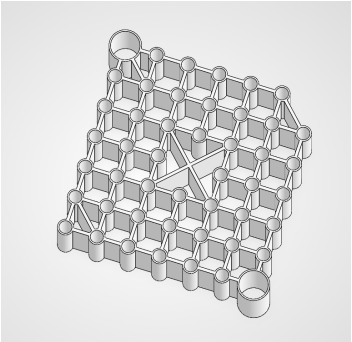
Table 3.2: Benchmark geometry families and their identifiers.

ID	Geometry family	Primary sensitivity probed
UT	Upper tie plate (unit cell)	Strut width, bore ID/MD/OD, internal walls
SQ_F	Square grid filter (unit cell)	Pore size, web wall thickness, corner fidelity
TW	Thin walls	Wall thickness deviation vs. nominal, 0.5 to 1.5 mm
C_TW	Cross walls	Wall thickness at intersection nodes
CY	Cylinder matrix	OD/ID deviation, small-bore closure limit
CB	Cube benchmark set	Edge radii, different types of holes, grooves, notches
OH	Angled overhangs	Down-skin surface texture at 45°
HX	Hexagonal porous plate	Hexagonal pore accuracy, plate thickness

Upper Tie Plate (UT) A unit-cell test coupon derived from the ATRIUM 11 upper tie plate lattice used in BWR fuel assemblies, as shown in Figure 3.2. The coupon preserves the characteristic features of the full-scale part, such as thin struts, node intersections, bores, and open lattice cells, all of which are dominated by border scanning behaviour. It combines internal surfaces (bores) and external surfaces (struts and walls) within a single coupon, which proved to be the decisive property for the central result of this thesis. Five full-part replicates were manufactured in Print 3 for the post-processing study, and 26 test coupon replicates in Print 2 for the DoE study.



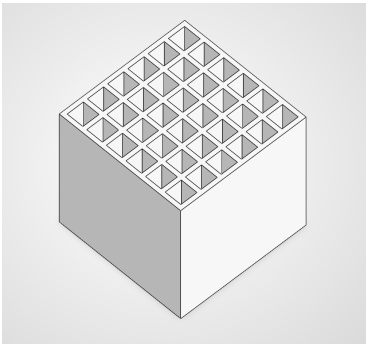
DoE test coupon UT



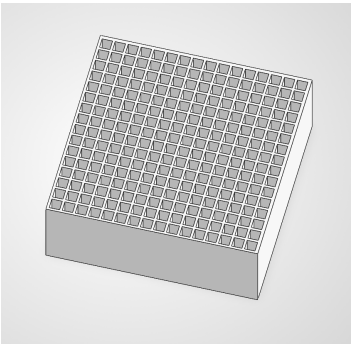
Full geometry UT

Figure 3.2: Upper tie plate-inspired geometries.

Square Grid Filter (SQ_F) A unit-cell test coupon derived from BWR fuel assembly spacer/debris filter grid geometry, as shown in Figure 3.3. The coupon contains square perforations with varying hole sizes, preserving the corner sharpness, hole dimensional accuracy, and hatch-to-border transition fidelity characteristics of the full-scale part. Because the coupon contains both pores (which respond as internal features) and webs (which respond as external features), it was analysed with the same feature-group split as the upper tie plate.



DoE test coupon SQ_F



Full geometry SQ_F

Figure 3.3: Square grid filter-inspired geometries.

Thin Walls (TW) Vertical thin-wall structures with nominal wall thicknesses of 0.5, 0.7, 0.9, 1.1, 1.3 and 1.5 mm, attached to a common base, as shown in Figure 3.4. These geometries are critical because at 0.5 mm wall thickness with two borders, the contour track width fills essentially the entire wall cross-section and the part becomes entirely border-built, with no hatch region. This makes thin walls the most direct probe of border parameter effects, and the graded thickness series makes it possible to test directly whether the dimensional error is a constant offset or a proportional (scaling) error. In total, 21 test coupon replicates were fabricated in Print 2 for the DoE study.

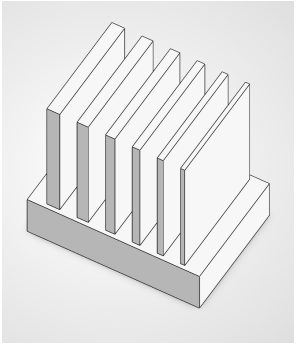


Figure 3.4: DoE test coupon TW.

Cross Walls (C_TW) Intersecting thin walls forming X-junctions at 0.5–1.5 mm thickness, as shown in Figure 3.5. These features isolate the behaviour at wall intersection nodes, where melt pool interactions between two converging border passes can produce localised overheating, oversizing, or material accumulation. Eleven test coupon replicates were fabricated in Print 2 for the DoE study.

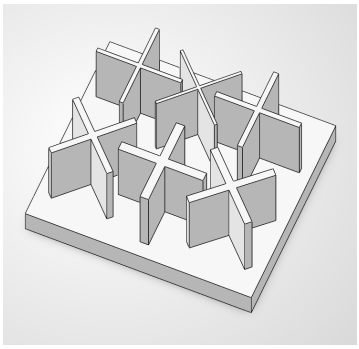


Figure 3.5: DoE test coupon C_TW.

Cylinder Matrix (CY) Sets of cylindrical features with varying outer and inner diameters, arranged as groups of five pads per set, as shown in Figure 3.6. Circularity error and OD/ID deviation are the primary response variables. Eleven test coupon replicates were fabricated in Print 2 for the DoE study.

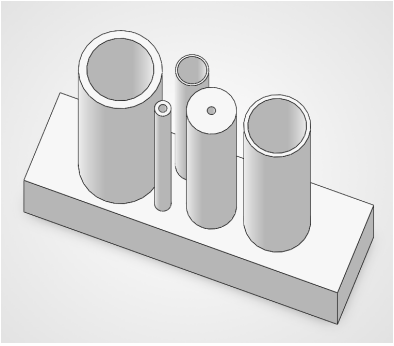


Figure 3.6: DoE test coupon CY.

Angled Overhangs (OH) Square cross-section struts oriented at 45° from the horizontal, as shown in Figure 3.7. These features evaluate down-skin surface quality

at a fixed overhang angle. Eleven test coupon replicates were fabricated in Print 2 for the DoE study.

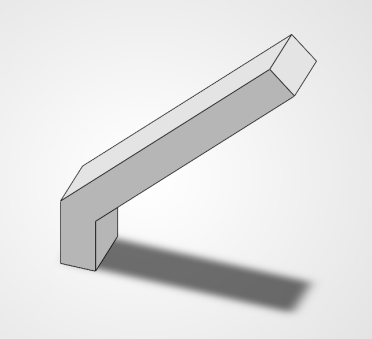


Figure 3.7: DoE test coupon OH.

Cube Benchmark Set (CB) Cubes ($15 \times 15 \times 15$ mm) incorporating edge fillets (0, 0.5, 1 and 3 mm radii), blind and through holes, grooves and notches (100°–150° included angle), and teardrop features, as shown in Figure 3.8. Eleven replicate sets were fabricated in Print 2 for the DoE study.

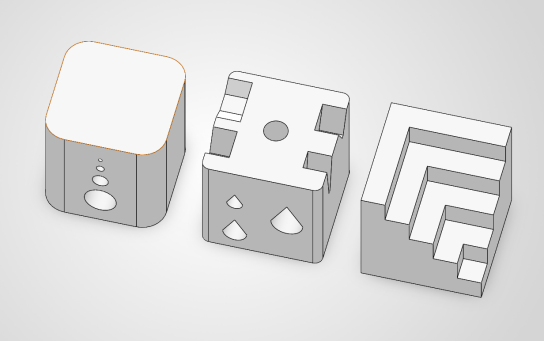


Figure 3.8: DoE test coupon set CB.

Hexagonal Porous Plate (HX) Inspired by VVER-440 fuel assembly filter plate geometry, this feature contains hexagonal perforations in a thin plate structure. The combination of straight-edged hole boundaries meeting at 120° vertices and thin plate webs makes it sensitive to both beam compensation and border scan speed. The geometry is shown in Figure 3.9. Five replicates were manufactured in Print 3 for the post-processing study.

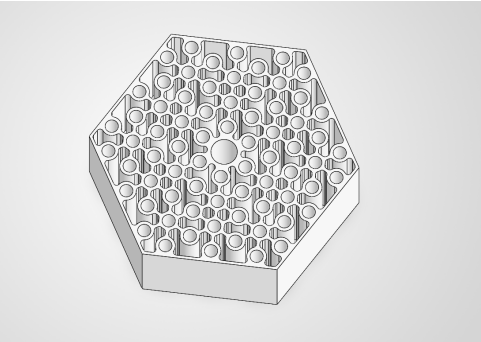


Figure 3.9: Full geometry HX.

All geometries were designed with support-free orientation where possible. Each sample was assigned an engraved identification code on its base (e.g., `UT_01` for upper tie plate run 1, `TW_S01` for thin wall set 01, `CY_S1_P1` for cylinder set 1 pad 1) to enable unambiguous traceability between DoE run parameters and characterisation measurements.

3.5 Design of Experiments

3.5.1 Tiered allocation of experimental effort

Seven geometry families were investigated within a single build campaign, which required experimental effort to be allocated rather than distributed evenly. Different designs were therefore assigned according to the expected response complexity and the application relevance of each geometry [38].

The upper tie plate (UT) and square grid filter (SQ_F) represent the features of primary application interest and received a response-surface design capable of resolving curvature and two-factor interactions. The thin-wall series (TW) received an orthogonal factorial design with centre replication, sufficient to resolve main effects and interactions across a graded feature-size series. The cylinder matrix (CY), cross walls (C_TW), cube benchmarks (CB) and 45° angular struts (OH) received three-factor factorial designs with centre replication, able to establish the direction and magnitude of main effects but not curvature.

3.5.2 Factor selection and levels

Hatch parameters were held constant throughout, following the baseline characterisation, after which it was decided to optimise the productivity workflow by isolating the border parameters and subjecting only them to a detailed DoE. The factors varied are therefore contour-specific.

Three geometries share a common contour factor set: contour laser power, contour scan speed, beam compensation and number of borders. The remaining geometries vary a reduced or substituted factor set appropriate to the feature they probe. The overhang series (OH) varies down-skin parameters rather than contour parameters,

because the surface of interest is solidified onto loose powder rather than traced by a contour pass. Table 3.3 summarises the designs.

Table 3.3: Design of experiments by geometry family. All designs are orthogonal, with a largest absolute pairwise factor correlation of 0.000 in every case.

Zone	Geometry	Runs	Factors	Design
1	Upper tie (UT)	26	4	Face-centred CCD, 4 centre points
2	Square grid filter (SQ_F)	26	4	Face-centred CCD, identical run list to UT
3	Thin walls (TW)	21	4	2^4 factorial + centre block, 2 replicate pairs
4	Cylinder matrix (CY)	11	3	2^3 factorial, 3 centre points
5	Cross walls (C_TW)	11	3	2^3 factorial, 3 centre points
6	Cube benchmarks (CB)	11	3	2^3 factorial, 3 centre points
7	Angular struts, 45° (OH)	11	3	2^3 factorial, 3 centre points

Zones 1 to 3 vary contour power, scan speed, beam compensation and number of borders. Zones 4 to 6 vary contour power, scan speed and beam compensation, with the number of borders fixed. Zone 7 varies down-skin border power, down-skin border speed and beam compensation. Because the geometries do not share a common design, no single model is fitted across all of them; each geometry is modelled separately and the fitted effects are compared in Section 5.5.

- **Response Surface Designs: UT and SQ_F -**
  The UT and SQ_F geometries were assigned a face-centred central composite design. The axial distance was set to unity so that the axial runs lie on the faces of the factorial cube rather than beyond them, which restricts each continuous factor to three levels and keeps every run inside the qualified process window. The 26 runs decompose into 16 factorial runs, covering the 2^3 combinations of power, speed and beam compensation at both levels of number of borders; six axial runs, two for each continuous factor; and four centre runs.

  The design is orthogonal, with all pairwise factor correlations equal to zero. Power, scan speed and beam compensation are each balanced 9/8/9 across their three levels and the number of borders 13/13. Three of the centre runs, UT_8, UT_9 and UT_18, are genuine replicates at 150 W, 350 mm/s, 0.07 mm and two borders. These provide a pure-error estimate independent of the fitted model and make the lack-of-fit test available for every response. The design supports a full quadratic model in the three continuous factors.

  The SQ_F geometry was built on the identical run list, so that a perforated plate and a bored section experience exactly the same parameter conditions and any difference in response between them is attributable to geometry alone.
- **Orthogonal Design with Centre Replication: TW -**
  The thin-wall series was assigned an orthogonal design rather than a central composite design, because its purpose is to resolve how a given parameter effect varies across a graded feature-size series rather than to locate an optimum in the factor space. Runs TW_1 to TW_16 form a complete 2^4 factorial at the extreme levels of contour power, scan speed, beam compensation and number of borders. Runs TW_17 to TW_20 sit at the centre condition for power and

speed with beam compensation duplicated at both extremes, and TW_21 is the full centre point. All pairwise factor correlations are exactly zero.

Each TW coupon carries six walls at nominal thicknesses of 0.5, 0.7, 0.9, 1.1, 1.3 and 1.5 mm, so the 21 runs yield a size series at every parameter condition. This structure is what permits the separation of a constant boundary offset from a proportional scaling error in Section 4.3, since the same parameter condition is observed at six feature sizes simultaneously.

- **Screening Designs: C_TW, CB, CY and OH -**
  The remaining four geometries were assigned three-factor two-level full factorials with three centre-point replicates, giving eleven runs each. In every case all pairwise factor correlations are zero, and the three centre points supply two pure-error degrees of freedom and a lack-of-fit test. These designs resolve main effects and two-factor interactions but cannot estimate curvature, so a significant lack of fit is interpreted as evidence of curvature rather than modelled. The number of borders is fixed in all four, so the comparison with the four-factor geometries isolates the contribution of that factor.

  The overhang geometry was investigated by varying the down-skin border parameters. Only the down-skin border study was characterised; the hatch study was manufactured but not measured, and is not analysed in this work.

3.5.3 Response variables

Two families of response variables were measured.

- **Dimensional deviation**—the difference between the fabricated and nominal CAD dimension for wall thickness, hole and bore diameter, strut width and edge features.
- **Areal surface roughness**—arithmetic mean height (S_a), maximum height (S_z), ten-point height (S_{10z}), and skewness (S_{sk}), measured and studied on side-skin and bore surfaces using confocal microscopy and defined according to ISO 25178-2 [42].

Signed rather than absolute deviation: A methodological decision was taken during data consolidation that materially affects the conclusions and is therefore stated explicitly. The measurement workbooks as originally recorded reported *absolute* relative deviation $|\Delta\%|$ throughout. Absolute deviation cannot distinguish an oversized feature from an undersized one; consequently it cannot yield a compensation value, and it biases regression because the response is folded about zero. All analyses in this thesis therefore use the *signed* deviation in millimetres,

$$\Delta = d_{meas} - d_{nom}, \tag{3.1}$$

as the primary response, with negative values denoting an undersized feature. Signed and absolute relative deviations are retained as secondary columns so that the original rankings remain reproducible. The reason this matters is developed in Section 4.3: reporting in $|\Delta\%|$ makes the error appear to grow as features get smaller, when in millimetres it does not.

3.6 Build plate layout

The build plate layout was designed to organise the seven geometry families into spatially distinct zones, facilitating parameter assignment and reducing thermal interaction between geometries. The build plate was divided into seven zones, one for each geometry family; Figure 3.10 shows the zone arrangement.

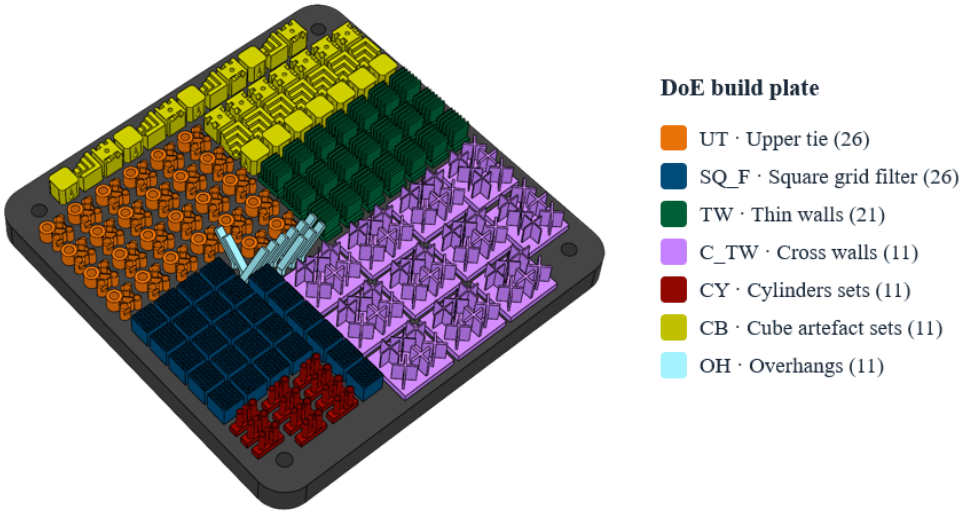


Figure 3.10: Build plate layout for Print 2, showing the seven DoE zones, part placement and the rear-to-front gas flow direction within the SLM 280 chamber.

A minimum spacing of 5 mm was maintained between individual parts, with 5 mm gaps between zone boundaries, to limit thermal interaction between neighbouring specimens. The layout additionally considered the inert gas flow direction within the SLM 280 chamber and the recoater movement (rear to front). Parts were arranged so that within each zone all samples occupied similar positions relative to the gas flow axis, reducing gas-flow-related confounding and allowing an individual zone to be terminated if any geometry family encountered problems during fabrication. Run identification codes were engraved on the samples using an engraving pen after stress-relief annealing, to maintain traceability throughout the characterisation and analysis pipeline.

3.7 Build preparation

Build preparation was performed using Materialise Magics software for part placement and orientation on the virtual build platform. For the DoE builds, a layer thickness of 60 µm was used throughout, corresponding to the productivity-oriented process condition selected as the basis for the border-parameter optimisation. All test coupon geometries were designed for support-free fabrication in accordance with the DfAM considerations described above; no support structures were used in the DoE build.

Process parameter assignment and slicing were performed through the SLM Build Processor integrated within Materialise Magics. The build processor uses a spreadsheet-based parameter template in which each column corresponds to a named part on the build plate and each row to a specific process parameter (border laser power, border scan speed, beam compensation, number of borders, hatch parameters, down-skin parameters, and so on). Translating the JMP-generated DoE run table into this template format and assigning parameters to each part individually is a tedious manual process; to streamline this, a simple automation script was developed to convert the DoE run tables into the Magics-compatible Excel format, which could then be imported directly as build profiles and auto-assigned to the corresponding parts. Hatch and down-skin parameters were held constant across all parts, as only border parameters were investigated in the DoE.

After parameter assignment, the build was sliced at the prescribed layer thickness (60 µm). The assigned parameters were cross-verified in the sliced file against the original DoE study data to confirm that each part carried the correct border parameter combination. This verification step is worth emphasising: because the parameter assignment is external to the CAD, a silent mis-assignment would be invisible in the built parts and would invalidate the entire dataset, so cross-verification was treated as a mandatory gate before release to build.

3.8 Manufacturing procedure

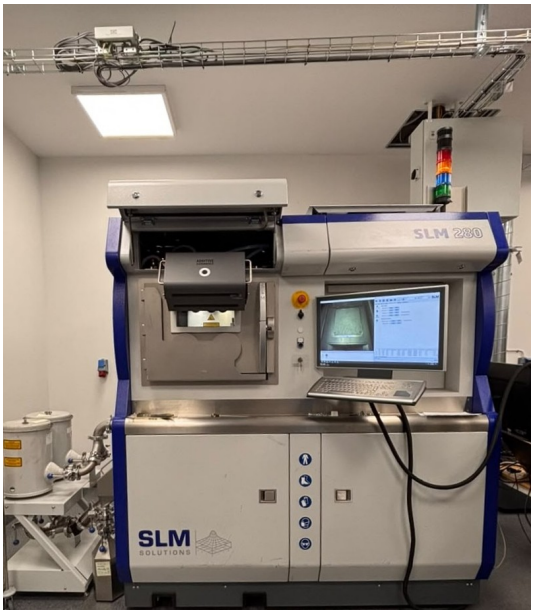


Figure 3.11: SLM 280 PBF-LB machine used for the experimental builds.

Three build jobs were executed during this thesis using an SLM 280 laser powder bed fusion system (Nikon SLM Solutions), shown in Figure 3.11. The machine has a nominal 280 × 280 mm build platform and was operated with two lasers during the builds.

- **Print 1 (April 2026).** The initial build attempted the full DoE across all geometry families. Releasable block supports had been specified to allow bandsaw removal of the specimens from the plate, but the high density of 316L gave these supports insufficient anchoring: parts warped, detached, and collided with the recoater, as seen in Figures 3.12 and 3.13, forcing an abort. Post-mortem inspection additionally identified that several parameter combinations had produced local overheating through excessive linear energy density. Two changes followed: parts were anchored directly to the build plate in subsequent builds, with wire EDM substituted for bandsaw removal; and the problematic high-energy parameter combinations were removed from the design, reducing the initially designed CCD from 28 to 26 runs. No usable specimens were recovered; the build served as a learning iteration.

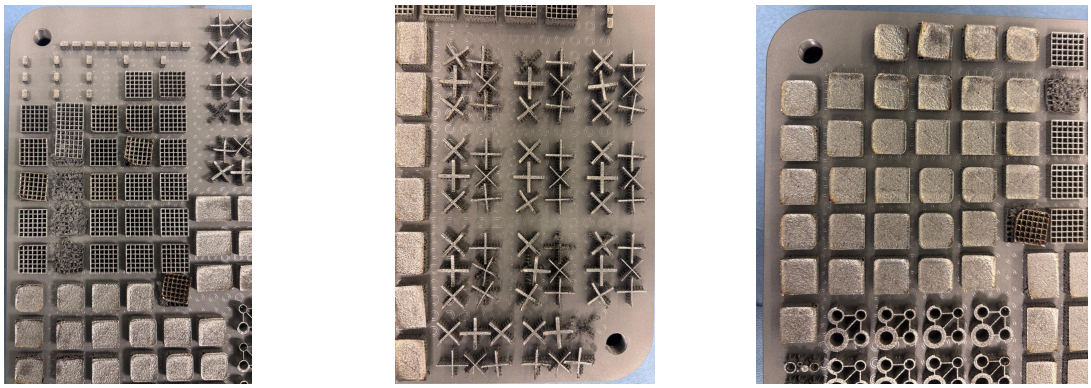


Figure 3.12: Close-up of failed geometries (Print 1).

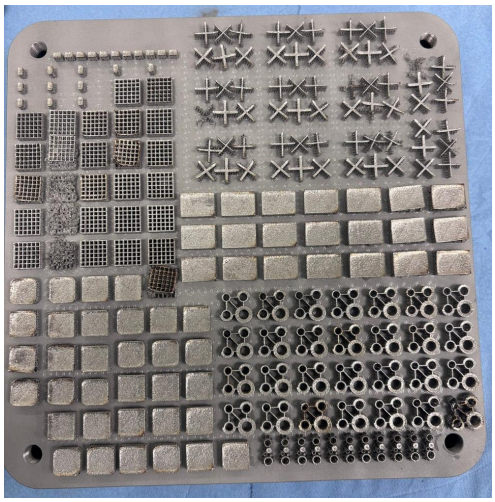


Figure 3.13: Build plate with failed parts (Print 1).

- **Print 2 (early May 2026).** The primary DoE build, and the source of all data reported in Chapter 4. All 117 DoE samples across the seven geometry families were manufactured successfully with direct plate anchoring, as seen in Figure 3.14. The build was executed under argon atmosphere with oxygen levels maintained below the machine's safety threshold. Visual inspection

confirmed that all geometries were structurally intact, and preliminary dimensional checks indicated that the printed features were consistent with CAD intent. Thermal monitoring was performed during this build using a newly installed Additive Assurance in-situ camera system; although outside the scope of this thesis, the thermal data were used during printing to monitor potential failure zones and regulate the process within safe operating limits.

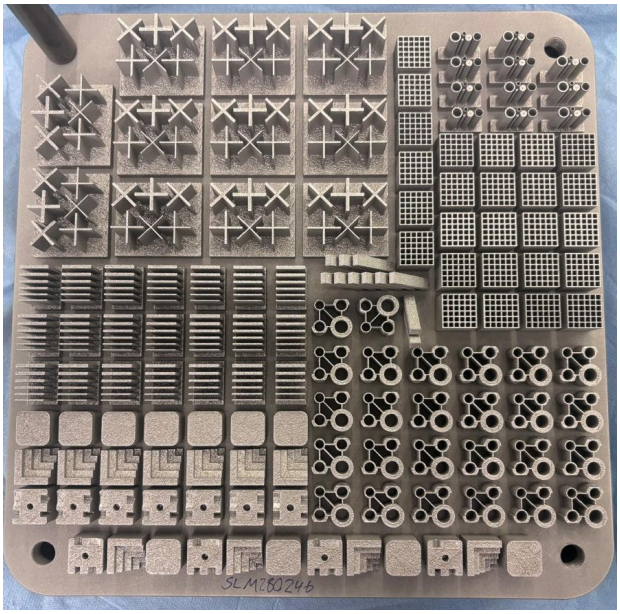


Figure 3.14: Successfully fabricated DoE coupons on the build plate in the as-printed condition (Print 2).

- **Print 3 (Mid-May 2026).** A supplementary build outside the primary thesis scope, producing five copies each of the upper tie plate, hexagonal porous plate, and square grid filter at full scale. Of these, two copies of each geometry were printed with custom M3 mounting pads and a 200 µm face offset to account for uniform material removal during Hirtisation, as shown in Figure 3.15. The remaining parts were allocated to other surface-finishing processes: one replicate for abrasive flow machining (AFM) with a 150 µm offset, and two replicates at the original thickness, one for plasma polishing and one as a reference piece, as part of the broader industrial project. The build also included additional thin-wall samples printed using the baseline parameters but with two different hatch distances (0.08 and 0.12 mm) and no layer rotation or active borders. These samples were included as preliminary exploratory tests to evaluate the influence of scan strategy on microstructural development. All Print 3 samples were manufactured successfully.

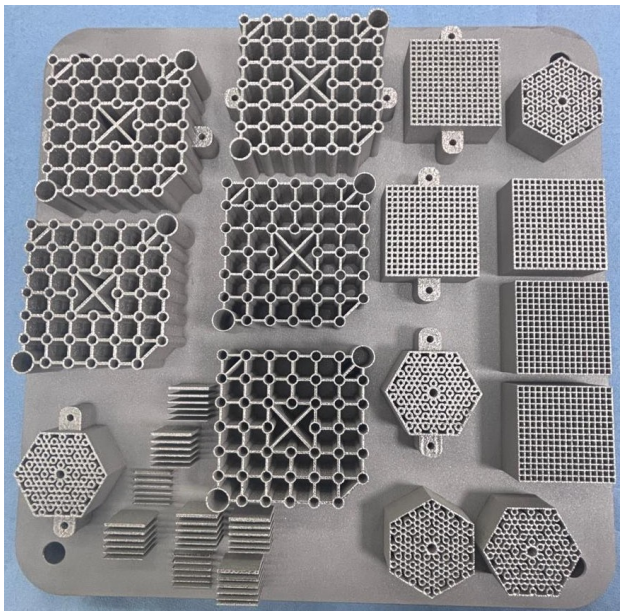


Figure 3.15: Full-scale geometries for the post-processing study on the build plate (Print 3).

3.9 Post-processing

Following manufacturing, samples from Print 2 were transported from RISE to Chalmers University of Technology for post-processing. Both wire EDM and heat treatment were performed at Chalmers: the change from releasable supports to direct plate anchoring made the initially planned bandsaw removal unviable, and no wire EDM facility was available at RISE, while the furnace at RISE could not accommodate the build plate. This made Chalmers the practical choice for both operations in the same visit.

Wire electrical discharge machining (EDM) was used to separate the printed samples from the build plate. Wire EDM was selected for its ability to produce precise cuts with minimal physical modification to the printed parts, which is important for preserving the as-printed dimensional state of the geometries. Stress-relief annealing was performed before the wire cut, at 450 °C for 6 hours in an argon atmosphere, followed by furnace cooling.

Stress relief prior to dimensional characterisation is necessary because residual stresses accumulated during the PBF-LB process can cause delayed distortion upon cutting, which would confound the dimensional measurements intended to reflect contour parameter effects [7]. During the subsequent metrology campaign, selected samples were additionally sectioned on a precision cutter to prepare cross-sections for confocal surface characterisation.

No additional surface finishing operations were performed on the DoE samples, as the objective of this study was to characterise the as-printed surface condition resulting from the border parameter variations.

3.10 Dimensional characterisation

Dimensional characterisation was performed to quantify deviations between fabricated geometries and their nominal CAD dimensions, and to correlate these deviations with border scanning parameter variations. Measurements were performed using a Leica M205 C stereomicroscope equipped with a Leica DFC450 digital camera (Figure 3.16). A variety of images were acquired for the different specimen geometries and feature types, with the relevant dimensions annotated directly on the images. Measurements were taken at multiple locations along the features to account for spatial variation and improve measurement repeatability. The microscope was operated at a zoom setting of 0.78 for the dimensional measurements. For example, Figure 3.16 shows how several positions along the wall height and across the wall length were measured for the TW geometry; similarly, for the cylinder and bore features, multiple diameters were measured per bore.

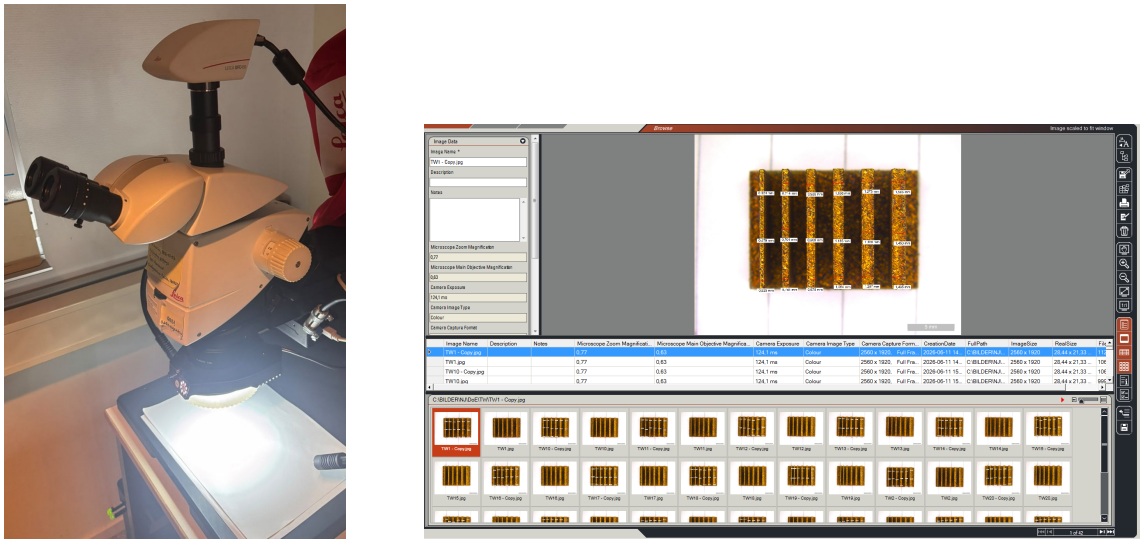


Figure 3.16: LOM set-up: (a) Leica M205 C during calibration; (b) screenshot of annotation performed in the Leica software.

In total, 1805 individual dimensional measurements were recorded across the characterised geometry families. Each measurement is stored as a row in a customised spreadsheet, carrying the run identifier, the DoE factor levels, the feature name, the feature group, the nominal dimension, the measured dimension and the derived signed and relative deviations, which allows any subset to be modelled without re-deriving the response.

The dimensional response variables measured for each geometry type are summarised in Table 3.4.

Table 3.4: Dimensional response variables by geometry family, and the feature group assigned for analysis.

Geometry	Dimensional response	Feature group
UT	Bore inner diameter	Internal
UT	Bore mid and outer diameter	External
UT	Wall / strut thickness	External
SQ_F	Pore opening size	Internal
SQ_F	Web wall thickness	External
TW	Wall thickness at 0.5–1.5 mm nominal	External
C_TW	Wall thickness at and away from nodes	External
CY	Bore inner diameter	Internal
CY	Pad outer diameter	External
CB	Edge radii, different types of holes, grooves, notches	Mixed

3.10.1 Feature grouping

Features were classified as *internal* (material-bounded openings: bores, pores, holes) or *external* (free-standing solid boundaries: walls, struts, pad outer diameters). This classification is not cosmetic. A given inward beam compensation moves the laser path towards the solid on both sides of an external feature, making it smaller, and away from the solid on both sides of an internal feature, making it larger. Pooling the two groups therefore averages two opposing responses and can make a strong effect appear to vanish, which is exactly what was initially observed on the square grid filter, where the pore and web responses cancelled in the pooled mean.

3.11 Surface characterisation

Surface roughness characterisation was conducted to evaluate side-skin surface morphology and quantify the influence of border scanning parameters on surface quality.

Surface topography was characterised using a Sensofar S neox optical 3D measurement system equipped with a Nikon EPI 20× objective (Figure 3.17). Measurements were performed using the confocal fusion technique to acquire three-dimensional surface topography. The measured topography was processed using MountainsMap Premium, where the surfaces were levelled and evaluated according to ISO 25178-2. The areal surface parameters S_a, S_z, S_{10z}, and S_{sk} were extracted to quantify the surface characteristics of the manufactured specimens. Areal (3D) parameters were used in preference to profile (2D) parameters throughout, following the recommendation of Townsend et al. [20] that areal parameters are substantially more representative of additively manufactured surfaces, whose features are three-dimensional and directionally non-uniform, than profile parameters extracted along a single line.

The following areal roughness parameters, defined in ISO 25178-2 [42], were evaluated:

- S_a (arithmetic mean height)—the average absolute deviation of the surface



Figure 3.17: Confocal microscopy set-up used in the experiments.

from the mean plane. This is the primary roughness indicator and the most widely reported parameter in the PBF-LB literature.

- S_z (maximum height)—the vertical distance between the highest peak and deepest valley within the evaluation area. This parameter captures worst-case surface features that may affect functional performance.
- S_{10z} (ten-point height)—the mean of the five highest peaks and five deepest valleys, a more robust alternative to S_z that is less sensitive to a single outlying particle.
- S_{sk} (skewness)—the asymmetry of the surface height distribution. Negative skewness indicates a surface dominated by valleys (pitted), while positive skewness indicates a surface dominated by peaks (bumpy). This parameter distinguishes a surface roughened by adhered particles from one roughened by pits and dross, which S_a alone cannot do.

Measurements were performed on side-skin surfaces, i.e. the vertical faces of printed geometries where border scanning parameters directly control surface formation, and additionally on the internal bore surfaces of the upper tie plate coupons; stitched areas of 4×2 fields were used for the upper tie plate coupons. For thin-wall geometries, measurements were taken on each of the six nominal wall thicknesses within a coupon. Stitched measurement areas (4×4 fields) were used where larger evaluation areas were required to achieve statistically representative results, consistent with the guidance that PBF-LB surface texture should be assessed over areas of at least a few millimetres square in order to capture the melt track periodicity as well as the

particle-scale texture [21].

Filtering and data processing were performed in the MountainsMap software according to standard areal surface metrology practice, with an appropriate L-filter nesting index selected to separate roughness from form and waviness components. The software was also used to generate a report for each measurement in a standardised template, as shown in Figure 3.18.

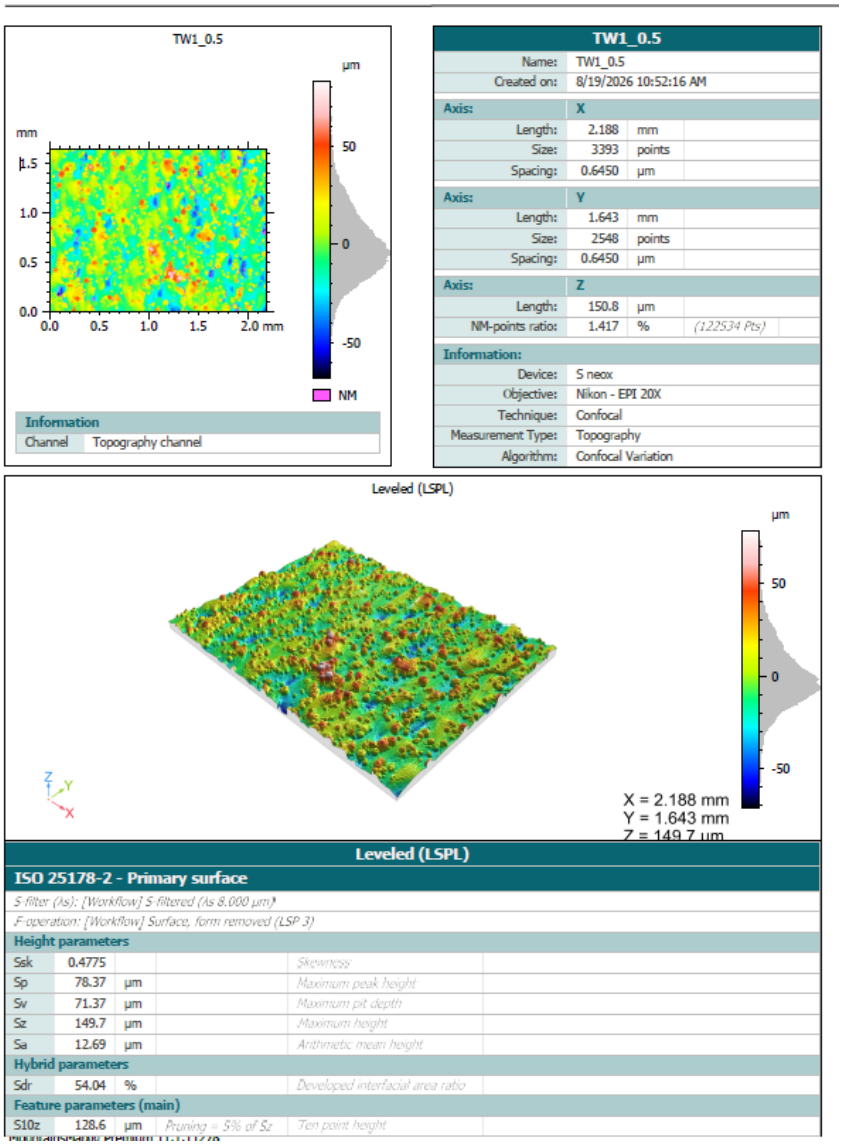


Figure 3.18: An example of report generation in MountainsMap.

3.11.1 Coverage limitation

Confocal measurement is slow relative to optical dimensional measurement, and within the project timeframe only 51 surfaces were acquired: both a wall and a bore surface on five upper tie plate runs, six walls on five thin-wall runs, and eleven

overhang struts. As shown in Section 4.9, this coverage is sufficient to support a paired comparison between surface types but not sufficient to fit any parameter-roughness model, because the measured runs do not span the entire DoE space. This is stated here rather than in the results because it is a limitation of the measurement plan, not of the data analysis.

3.12 Statistical analysis

Statistical analysis was conducted using JMP software (SAS Institute) to evaluate the effects of the border scanning parameters, establish parameter-response relationships, and identify process conditions associated with improved dimensional accuracy and surface quality. Although the DoE was designed in JMP, the subsequent statistical analysis was based on the responses that were practically characterised for each geometry family.

Each geometry family was characterised according to the planned measurement procedures described in the preceding sections. Dimensional measurements were conducted for six of the seven geometry families: Upper Tie Plate (UT), Square Grid Filter (SQ_F), Thin Wall (TW), Cross Thin Wall (C_TW), Cube Benchmark (CB), and Cylinder (CY). The Overhang (OH) geometry was characterised only through surface measurements, as its primary purpose was to investigate down-skin surface characteristics and no dimensional measurements were performed for this geometry.

For surface characterisation, five selected samples from the UT and TW geometry families were additionally examined using confocal microscopy to obtain surface measurements from representative side-skin features. These measurements were treated as supplementary surface responses and were analysed separately from the main dimensional response dataset. The OH geometry, in contrast, was characterised specifically for its down-skin surface response and its surface measurements were included in the statistical analysis.

Prior to statistical modelling, the measured data were extracted and subjected to descriptive and trend analysis in Excel (all measurement data are available in Appendix B). This preliminary analysis was used to verify the measured responses, identify trends with respect to the border parameters, and determine which datasets contained sufficient and relevant observations for subsequent JMP analysis. Only the datasets considered suitable for statistical modelling were transferred to JMP. Consequently, the statistical analysis did not include every measured response from every geometry family. This distinction was necessary because the dimensional and surface characterisation campaigns were performed on different subsets of geometries and features, and some surface measurements were limited to selected specimens due to the scope and time constraints of the experimental campaign.

- **Response Surface Methodology (RSM)** was applied to fit second-order polynomial models describing the relationship between border parameters and

measured responses. The general form of the response surface model is:

$$y = \beta_0 + \sum_{i=1}^{k} \beta_i x_i + \sum_{i=1}^{k} \beta_{ii} x_i^2 + \sum_{i<j} \beta_{ij} x_i x_j + \varepsilon \tag{3.2}$$

where y is the measured response, x_i are the coded factor levels, β_i are the linear coefficients, β_{ii} are the quadratic coefficients, β_{ij} are the interaction coefficients, and ε is the residual error. The significance of each model term was assessed at $\alpha = 0.05$; effect sizes are reported in millimetres alongside p-values throughout, because a statistically significant effect that is smaller than the measurement noise floor has no engineering meaning.

Model adequacy was evaluated using R^2, adjusted R^2, and the root mean square error (RMSE), together with the lack-of-fit test. The centre-point replicates in each design provide the pure-error estimate without which a lack-of-fit test cannot be performed; a non-significant lack of fit indicates that the residual scatter is consistent with pure experimental noise rather than with unmodelled structure.

- **Compensation value extraction.** For each feature class, the fitted model was solved for the beam compensation at which the predicted signed deviation is zero, evaluated at the centre settings of the remaining factors. This inverse use of the model is the practically actionable output of the study: it converts a regression coefficient into a machine setting.

- **Prediction Profiler** in JMP was used to visualise the fitted responses and locate the zero-deviation settings.

- **Cross-geometry comparison.** Because the geometries share the same factors but are not on a common design, each geometry was modelled separately and the fitted coefficients, principally the beam-compensation slope, were compared across geometries (Table B.1 and Figure 4.3).

4

Results

This chapter reports the experimental results obtained from Print 2. Section 4.1 covers qualitative manufacturing observations. Section 4.2 describes the consolidated dataset and its integrity. Sections 4.3 to 4.5 present the results against the factors. Sections 4.6 to 4.8 report where contour control reaches its limits. Section 4.9 presents the surface characterisation results and states explicitly what they can and cannot support. Section 4.10 summarises the verified findings, and Section 4.11 states the gaps that remain in the dataset.

Throughout this chapter, dimensional deviation is reported as the signed quantity $\Delta = d_{meas} - d_{nom}$ in millimetres, with negative values denoting an undersized feature, for the reasons set out in Section 3.5.3.

4.1 Manufacturing observations

Process behaviour was stable across the majority of the parameter combinations investigated. All benchmark geometries in Print 2 were fabricated without build interruption, recoater collision or part detachment, and visual inspection after powder removal confirmed that every coupon was structurally intact and separable from the plate.

Within that generally stable envelope, three qualitative observations were made that anticipate the quantitative results.

First, side-skin appearance varied visibly with contour scan speed. Coupons produced at the lowest scan speed of 200 mm/s, and hence the highest linear energy density, carried more prominent adhered particles on the side-skin than coupons produced at 500 mm/s, although the underlying boundary appeared better consolidated. The quantitative measurements in Section 4.9.2 confirm this reading: the high-energy coupons are the smoothest by mean height while being the most strongly peak-dominated by skewness.

Second, the smallest features in the cylinder matrix reached a genuine process limit. In run CY_7, at 170 W, 200 mm/s and 0.10 mm beam compensation, the smallest nominal bore fused completely and measured 0.000 mm. This run combined the highest contour energy input in this geometry family with the largest compensation,

which on its own would enlarge an internal feature. The result is not a measurement failure but a physically meaningful limit, and it is discussed in Section 4.8.

Third, no evidence of gross thermal distortion or warping was observed on any geometry family, including the thin walls. The dimensional deviations reported in this chapter are therefore attributable to melt pool placement and width rather than to part-scale distortion.

4.2 Consolidated dataset and data integrity

Measurement data from Print 2 were consolidated from nine source workbooks into a single dataset comprising 1805 individual dimensional measurements and 51 areal surface topography measurements. The distribution across geometry families is given in Table 4.1.

Table 4.1: Consolidated dataset: runs, factors and measurement counts by geometry family.

Geometry	Runs	Factors	Dimensional	Confocal
UT (upper tie plate)	26	4	390	10
SQ_F (square filter)	26	4	312	—
TW (thin walls)	21	4	378	30
C_TW (cross walls)	11	3	264	—
CB (cube benchmark)	11	3	352	—
CY (cylinder matrix)	11	3	109	—
OH (angled overhangs)	11	3	—	11
Total			**1805**	**51**

4.2.1 Design verification

Before any model was fitted, the realised design for the upper tie plate and square grid filter was verified against its intent. All pairwise correlations between the four factor columns were zero to four decimal places, confirming full orthogonality; level occupancy was 9/8/9 across the low, centre and high levels of laser power, scan speed and beam compensation, and 13/13 across the two border-count levels. Runs UT_8, UT_9 and UT_18 were confirmed as genuine replicates at the design centre (150 W / 350 mm/s / 0.07 mm / 2 borders). The pure-error standard deviation computed from those three replicates is

$$s_{pe} \approx 0.021 \text{ mm} \tag{4.1}$$

on wall features. This value is used throughout the chapter as the noise floor: an effect smaller than approximately 0.021 mm cannot be distinguished from run-to-run variation regardless of its p-value, and is reported as not practically significant even where it is statistically detectable.

4.3 The dimensional error is a constant offset, not a scaling error

The graded thin-wall series, spanning nominal thicknesses of 0.5, 0.7, 0.9, 1.1, 1.3 and 1.5 mm within every coupon, permits a direct test of the character of the dimensional error. If the error were proportional to feature size (a scaling error, as would arise from uniform shrinkage), then signed deviation would grow with nominal thickness. If the error is instead a fixed offset arising from the placement of the contour track relative to the CAD boundary, signed deviation would be independent of nominal thickness.

Regressing signed deviation against nominal size within each thin-wall run gives a slope of

$$\frac{\partial \Delta}{\partial d_{nom}} \approx -0.006 \text{ mm/mm}, \tag{4.2}$$

which is statistically indistinguishable from zero. The mean signed deviation by nominal thickness is given in Table 4.2.

Table 4.2: Mean signed deviation and mean absolute relative deviation by nominal wall thickness, thin-wall family. The deviation in millimetres is essentially constant; the percentage deviation is not.

Nominal (mm)	0.5	0.7	0.9	1.1	1.3	1.5
Mean signed Δ (mm)	-0.054	-0.055	-0.053	-0.052	-0.049	-0.067
Mean $\lvert\Delta\%\rvert$	14.6	10.7	7.4	6.3	5.3	4.9

Across a threefold range of nominal thickness, the signed deviation varies between -0.049 and -0.067 mm, a spread of 0.018 mm that is smaller than the 0.021 mm noise floor of Equation 4.1. The physical statement supported by the data is therefore:

> *Every wall from 0.5 to 1.5 mm nominal thickness is undersized by the same offset of approximately 0.055 mm, independent of feature size.*

The second row of Table 4.2 shows why this matters. Expressed as a percentage, the same constant offset produces a deviation that appears to worsen monotonically from 4.9% at 1.5 mm to 14.6% at 0.5 mm, a threefold difference. That apparent trend is arithmetic, not physical: it is the constant 0.055 mm divided by a shrinking denominator. The commonly reported observation that thin walls have poorer dimensional accuracy than thick walls may, within the investigated process window and thickness range, be largely due to the use of relative rather than absolute deviation.

This has an important practical implication for compensation. The results do not support a single universal compensation value for all geometries, since the fitted relationships showed different intercepts for different feature classes. Instead, compensation can be defined at the feature-class level, with each class assigned a value

based on its measured response. Where a single global compensation value is required, a value of approximately 0.05–0.06 mm provides a practical compromise for the investigated geometries, although some residual deviation should be expected for the feature classes at the extremes of the observed range.

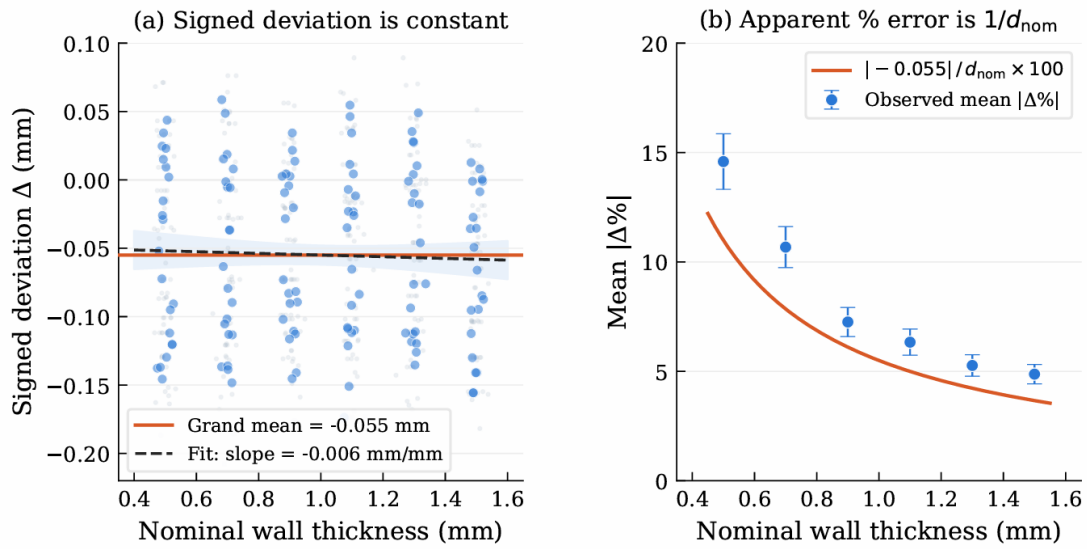


Figure 4.1: Thin-wall measurements shown in two ways. (a) Signed deviation remains nearly constant across wall thickness. (b) The same deviation appears larger as a percentage for thinner walls. The orange curve shows the expected percentage error for a constant absolute deviation.

4.4 Beam compensation is the controlling factor

4.4.1 Pooled response across geometry families

Mean signed deviation by beam compensation level is given in Table 4.3 for the three geometry families with sufficient runs to support the comparison.

Table 4.3: Mean signed deviation (mm) by beam compensation level, pooled across all other factors, for the thin-wall, cross-wall and upper tie plate families.

Beam compensation (mm)	TW	C_TW	UT
0.04	+0.003	+0.023	−0.070
0.07	−0.064	−0.054	−0.092
0.10	−0.112	−0.098	−0.133
Slope (mm per mm)	−1.9	−2.0	−1.05
Zero crossing (mm)	≈ 0.041	≈ 0.049	(see below)

The thin-wall and cross-wall families both respond with a slope close to −2 mm per mm of applied compensation. This is precisely the geometric expectation: an inward offset δ applied to both sides of a wall removes 2δ from its thickness. The

agreement between the measured slope and the geometric prediction is the strongest single piece of evidence in this study that beam compensation is doing what it is intended to do, and that the dimensional response is dominated by contour track placement rather than by any thermal mechanism.

The zero-deviation crossings sit at approximately 0.041 mm for thin walls and 0.049 mm for cross walls, just above the lowest level tested. Both are reachable settings.

The upper tie plate slope of -1.05 is anomalous against this picture, being close to half the expected magnitude. The resolution is given in the next subsection.

4.4.2 Feature class splits the response in two

The upper tie plate coupon contains both internal features (bores) and external features (struts and walls) within a single part. When signed deviation is pooled across all its features, the internal and external responses, which have opposite signs, partially cancel, producing the misleadingly shallow pooled slope of -1.05.

Fitting separately by feature group resolves this completely. Table 4.4 gives the beam compensation slope and model quality for each of the three feature classes.

Table 4.4: Beam compensation slope by feature class, upper tie plate family. Slopes are signed Δ in mm per mm of applied compensation.

Feature class	**Slope**	$\mathbf{R^2}$	**RMSE (mm)**	**Lack-of-fit** p
Bore ID (internal)	$+1.823$	0.892	0.0182	0.329
Bore OD/MD (external)	-2.093	0.914	0.0191	0.680
Wall (external)	-2.085	0.778	0.0306	0.674

Three features of this table deserve emphasis.

- **The signs are opposite and the magnitudes are similar.** Internal surfaces open up as compensation increases; external surfaces close down. Both magnitudes are close to 2, the geometric expectation for a dimension gaining or losing the offset on both sides. This is the central finding of the dimensional analysis.
- **The wall and external-bore slopes agree to two decimal places** (-2.085 and -2.093). Two independently measured feature types, on different parts of the same coupon, returning the same coefficient to within 0.4% is a strong internal consistency check, and it confirms that the mid and outer bore diameters behave as external surfaces.
- **The models are adequate.** All three lack-of-fit tests are comfortably non-significant ($p = 0.33$ to 0.68), meaning the residual scatter is consistent with pure experimental error rather than with unmodelled structure. The RMSE values of 0.018 to 0.031 mm bracket the 0.021 mm pure-error estimate, as they should for a well-specified model. Without the three centre-point replicates none of these statements could be made.

When all features of the square grid filter are analysed together, the beam-compensation response appears almost zero. However, separating the features reveals two strong responses in opposite directions. Internal pores increase in size with increasing beam compensation, while external walls decrease in size. These opposing responses cancel when the features are pooled, creating the misleadingly weak overall response depicted in Figure 4.2.

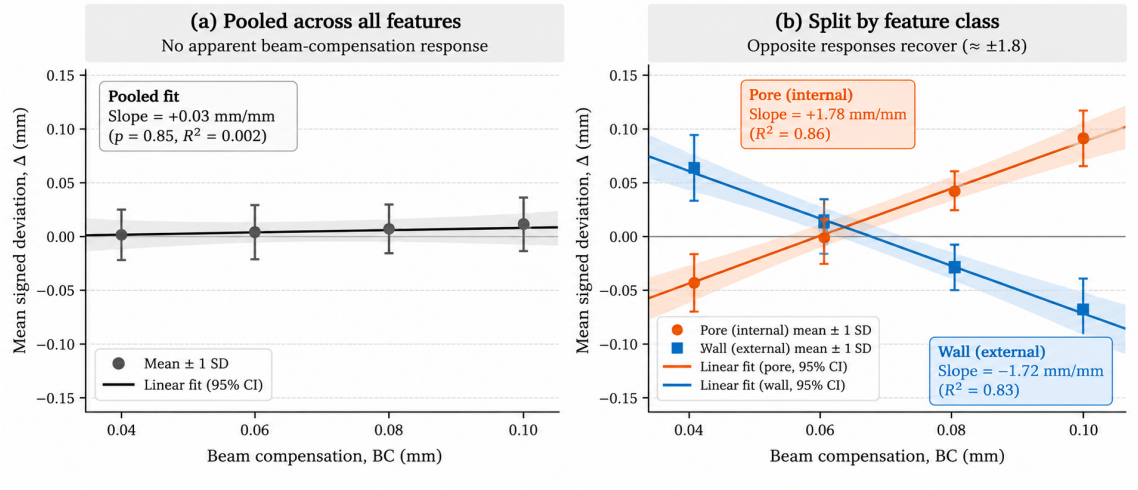


Figure 4.2: Square grid filter showing cancellation between feature classes. (a) The pooled response is nearly flat. (b) Separating pores and walls reveals strong but opposite responses.

4.4.3 Compensation values and their reachability

Solving each fitted model for the compensation at which predicted deviation is zero, evaluated at the centre settings of the remaining factors, gives the values in Table 4.5.

Table 4.5: Beam compensation required for zero signed deviation, by feature class and number of borders, evaluated at 150 W and 350 mm/s. The tested range was 0.04–0.10 mm.

Feature class	**1 border** (mm)	**2 borders** (mm)	**Reachable?**
Wall (external)	0.077	0.081	Yes, mid-range
Bore ID (internal)	0.110	0.107	At the edge of the range
Bore OD/MD (external)	no zero crossing		Not achievable in the tested range, $\Delta \approx -0.196$ mm

The fitted models indicate that the beam compensation required for zero dimensional deviation is feature-dependent. External walls reached zero predicted deviation within the tested range, at approximately 0.077–0.081 mm for one and two borders, respectively. For bore ID, the predicted zero crossing occurred slightly above the tested range, at approximately 0.107–0.110 mm. In contrast, the fitted

quadratic model for bore OD/MD remained negative across the entire tested range, with its least negative value of $\Delta \approx -0.196$ mm occurring at a compensation of approximately 0.048 mm, as seen in Table 4.5. Thus, zero deviation cannot be achieved for this feature class through beam compensation alone. A linear fit would suggest a zero crossing at a small negative compensation; however, this is an extrapolation and is not considered physically meaningful for the observed quadratic response.

> *No single global beam-compensation value nulls all three feature classes. Walls reach zero deviation at approximately 0.079 mm and bore inner diameters at approximately 0.108 mm, whereas the external bore diameters cannot be brought to zero at any tested setting.*

Using the wall optimum of 0.079 mm as a single global compensation would therefore leave the other feature classes uncorrected. At this setting, the predicted bore ID deviation is approximately $1.823(0.079 - 0.108) \approx -0.053$ mm, while the bore OD/MD deviation remains below -0.196 mm. Both deviations exceed the 0.021 mm noise floor, with the OD/MD deviation being approximately an order of magnitude larger. Compensation should therefore be assigned by feature class where possible. If the machine software permits only one global value, the prioritised feature class and the resulting deviations in the other classes should be explicitly considered.

- **Validity envelope.** These values apply to this machine, this material, the layer thickness and build condition of Print 2, and the tested ranges of 130–170 W, 200–500 mm/s and 0.04–0.10 mm compensation. The bore-ID value of 0.108 mm lies just outside the tested range and is a short extrapolation. For the external bore diameters, no compensation within the tested range reaches zero deviation, and a negative compensation is not a meaningful setting on this platform. Where external bore tolerances are tight, the correction must be made in CAD rather than in the parameter set. Confirmation coupons at 0.11–0.13 mm would close the bore-ID case.

- **Consistency across geometries.** The wall compensation values differ between families: approximately 0.041 mm for the isolated thin walls, 0.049 mm for cross walls and 0.079 mm for the upper tie plate walls. All three are external-surface values with the same sign and the same order of magnitude, but they are not identical. This indicates a residual geometry dependence superimposed on the dominant compensation effect, discussed in Section 5.4.

4.4.4 The unified relation: $\Delta = a \pm 2 \times \mathrm{BC}$

Across all nine dimensional responses measured in this study (walls, bores, outer diameters, pore widths, and cavity widths observed in the different coupon geometries), beam compensation acts with a slope whose magnitude is close to 2 and whose sign is set by the feature class:

$$\Delta_{\mathrm{ext}} = a - 2 \times \mathrm{BC} \tag{4.3}$$

$$\Delta_{\mathrm{int}} = a + 2 \times \mathrm{BC} \tag{4.4}$$

where a is a build-condition-specific intercept (dependent on power, speed, and thermal environment) and BC is the beam compensation value in millimetres. The factor of 2 is geometric, not fitted: a contour offset applied to both sides of a wall or both sides of a bore changes the measured dimension by twice the offset.

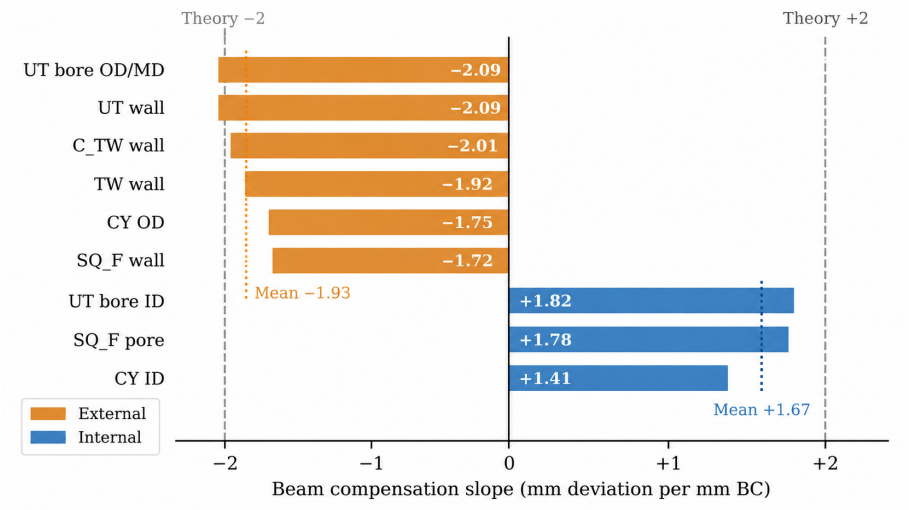


Figure 4.3: Beam compensation slopes (signed Δ per mm of BC) for all nine dimensional responses. External features (walls, outer diameters) cluster around a mean slope of -1.93; internal features (bores, pores) cluster around $+1.67$. The dashed lines indicate the theoretical expectation of ± 2.

Figure 4.3 plots the fitted BC slope for each dimensional response. The external-feature slopes have a mean of -1.93 and the internal-feature slopes a mean of $+1.67$. Both values are close to the geometric expectation of ± 2; the internal mean is slightly lower, which may reflect the additional thermal confinement that enclosed features experience. The sign split is consistent across every geometry tested: walls and outer diameters always shrink with increasing BC, while bores, pores, and cavities always grow.

4.4.5 Zero-crossing beam compensation by feature class

Setting $\Delta = 0$ in Equations 4.3 and 4.4 and solving for BC gives the compensation value at which each feature class reaches zero mean deviation. These values are listed in Table 4.6 and vary from 0.026 mm (CY outer diameter) to 0.108 mm (UT bore inner diameter). The external bore diameters of the upper tie plate are not listed, because their fitted response has no zero crossing within or near the tested range (Section 4.4.3).

Table 4.6: Beam compensation value at zero mean deviation for each feature class, computed from the per-geometry linear fits. Values are for the centre-point conditions (150 W, 350 mm/s) where applicable.

Feature class	Type	BC at $\Delta = 0$ (mm)
CY outer diameter	External	0.026
TW wall	External	0.041
SQ_F pore	Internal	0.045
C_TW wall	External	0.049
SQ_F wall	External	0.068
CY inner diameter	Internal	0.073
UT wall	External	0.079
UT bore ID	Internal	0.108

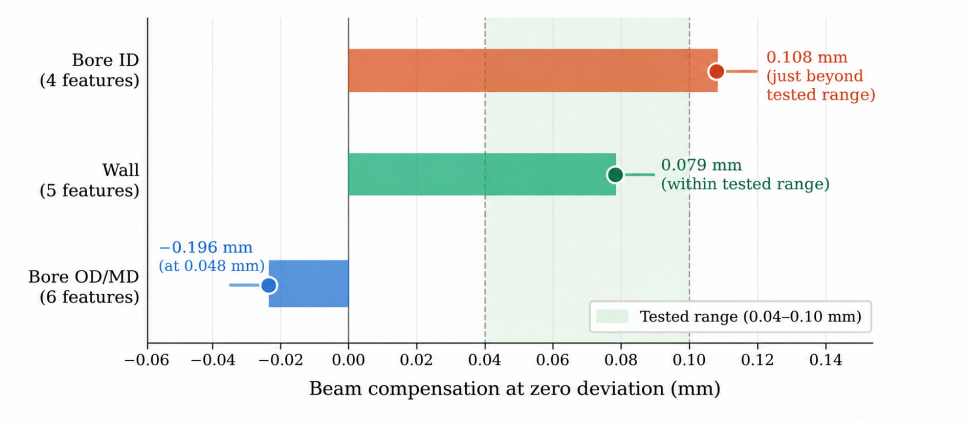


Figure 4.4: Zero-crossing beam compensation values by feature class, ordered from smallest to largest.

The spread of zero-crossing values shown in Figure 4.4 demonstrates that no single global beam compensation setting can simultaneously null the deviation on all feature classes. This is the central practical constraint: when a part containing several feature classes is run with a single global BC value, the choice of which feature class to prioritise determines the residual error on every other class. This trade-off is quantified in Chapter 5.

4.5 Scan speed, laser power and number of borders

4.5.1 Contour scan speed

Contour scan speed produced a genuine but small effect, and like beam compensation it also acts in opposite directions on internal and external features:

- Walls: -1.1×10^{-4} mm per mm/s ($p = 0.034$)
- Bore inner diameters: $+1.5 \times 10^{-4}$ mm per mm/s ($p < 0.001$)

Over the full tested range of 200 to 500 mm/s, these coefficients correspond to a change of -0.033 mm on walls and $+0.045$ mm on bore diameters. Both exceed the 0.021 mm noise floor, so the effect is active, but both are substantially smaller than the effect of beam compensation, which spans $-2.085 \times 0.06 = -0.125$ mm across its tested range. Beam compensation is therefore roughly four times more influential than scan speed on external features.

The direction is physically coherent. Increasing scan speed reduces linear energy density and hence melt pool width; a narrower contour track deposits less material outside the intended path, so external features shrink further and internal openings enlarge. The sign reversal between internal and external features mirrors that seen for compensation, and for the same geometric reason.

4.5.2 Contour laser power

Contour laser power was *not* statistically significant for any dimensional response, with p-values ranging from 0.35 to 0.80 across feature classes.

This is a negative result worth stating clearly, because it is contrary to the expectation that would follow from treating melt pool width as a simple function of power. Within the tested range of 130–170 W, a span of ±13% about the baseline, any effect of power on the final dimension is smaller than the experimental noise. The most likely explanation is that the tested power range was too narrow relative to the range tested on speed (±43%): expressed as linear energy density, the power axis spans a factor of 1.31 while the speed axis spans a factor of 2.5. It is therefore more accurate to say that power was under-ranged in this design than that power does not matter; a wider power range would be required to test the latter claim.

4.5.3 Number of borders

The difference in mean signed deviation between one and two border passes was approximately 0.009 mm, well inside the 0.021 mm noise floor, and was not statistically significant.

This is a useful practical result: within this parameter window, adding a second contour pass does not measurably change the dimension of the feature. Its influence on the compensation values in Table 4.5 is correspondingly small.

4.5.4 Curvature

Two quadratic terms reached significance:

- Beam compensation squared, on wall thickness ($p \approx 0.046$)
- Scan speed squared, on external bore diameters ($p \approx 0.007$)

Both terms are small relative to the main compensation effect. Their presence supports the use of a three-level design, since a two-level factorial cannot detect curvature. For walls and bore inner diameters, the curvature does not materially change the compensation values in Table 4.5, and the beam-compensation response can be treated as approximately linear over the tested range. The external bore diameters are the exception. Their quadratic response is concave and remains negative everywhere in the tested range, which is why no zero crossing is reported for them (Section 4.4.3).

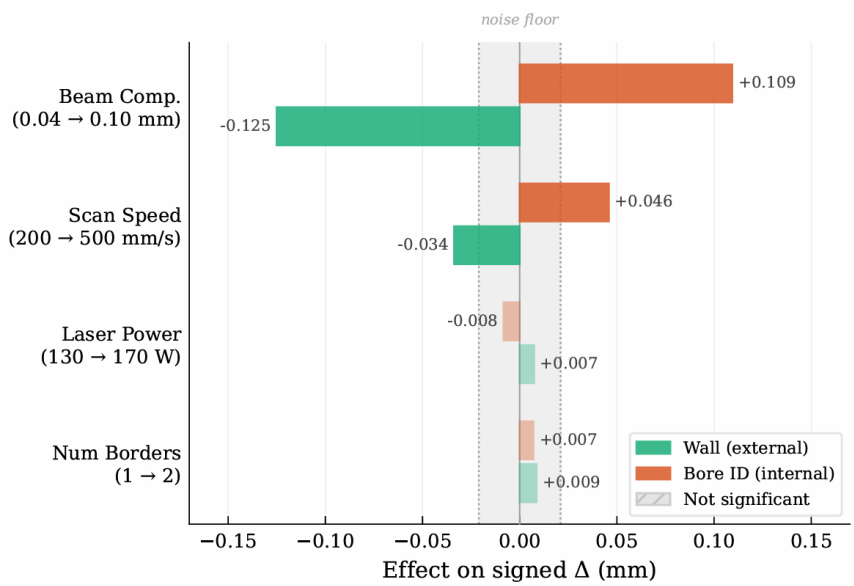


Figure 4.5: Factor effect sizes against the noise floor.

Figure 4.5 shows the change in signed deviation produced by moving each factor across its full tested range, for external wall and internal bore responses. Solid bars are significant at $\alpha = 0.05$; hatched bars are not. Dotted lines mark the ± 0.021 mm pure-error noise floor from the centre-point replicates. Beam compensation dominates; scan speed is real but about four times weaker and acts in opposite directions on the two classes; laser power and number of borders fall inside the noise.

4.6 Where contour control ends: the cube benchmark

The cube benchmark differs from every other geometry in this study in that its features, especially the internal ones, are embedded in 3–5 mm of surrounding solid within a 15 mm cube, rather than formed by thin, contour-defined sections. All four feature classes were fitted against the three contour factors. No model reached significance for the step faces, holes or fillets; the notches showed a single beam-compensation term, discussed below. The measured deviations are summarised in Table 4.7.

The step faces gave the lowest relative deviation of any feature measured in this

study, 1.4% on average, and no factor survived model reduction. At a section thickness of 3 mm the contour pass accounts for less than 5% of the cross-sectional area, so the dimension is governed by the hatch exposure rather than by the border.

Table 4.7: Cube benchmark: measured deviation by feature class and outcome of the fitted contour model.

Feature class	Mean Δ (mm)	SD (mm)	Mean $\lvert\Delta\rvert$ (%)	Model outcome
Step faces (3 mm)	-0.018	0.026	1.4	$p = 0.28$, n.s.
Holes (Ø0.5–4)	-0.162	0.060	> 5	$p = 0.33$, n.s.
Notches	–	–	1.9	$\delta\ p = 0.026$
Fillets (Ø2, Ø6)	–	–	5.9	$p > 0.10$, n.s.

The holes behaved as a fixed undersize of -0.162 mm with a standard deviation of 0.060 mm, independent both of hole diameter over the Ø0.5–4 mm range and of every parameter setting. Seven of the eight holes were undersized by 0.15–0.24 mm; the Ø3 bore was the exception, close to nominal (+0.017 mm). It is retained in the pooled value, as no parameter dependence was found for it either. This is the most informative result in the geometry, because it stands in direct contrast to the upper tie plate. A bore of comparable diameter passing through a 0.5 mm web gave a beam-compensation response of +1.823 mm per mm at $R^2 = 0.892$ (Table B.1); the same feature type surrounded by 3–5 mm of solid material gave no detectable response at all. The feature is identical and the machine is identical; what differs is the quantity of surrounding material, and therefore whether the contour or the hatch defines the final surface.

The external fillets showed a mean absolute deviation of 0.220 mm, 5.9%, with no significant term. Curved external features at these radii are formed largely by the hatch and are not controllable through contour settings. Unlike the contour-defined walls, the fillet error scales with size (≈0.08 mm at Ø2, ≈0.36 mm at Ø6, both ≈6%), consistent with a hatch-defined rather than contour-defined surface.

The notches gave a mean absolute deviation of 0.029 mm, 1.9%, consistent with the other external features of this geometry. Beam compensation reaches $p = 0.026$ with a fitted slope of -0.80 mm per mm. This slope is less than half the geometric expectation of -2 observed on every contour-defined external feature elsewhere in the study, and the discrepancy is not explained by the present data. The notch model is therefore reported but not used in formulating the compensation guidelines of Section 5.8.

Taken together, the cube benchmark shows that feature class predicts achievable accuracy more strongly than any parameter setting within it. The step faces remain below 1.5% in ten of the eleven runs (2.4% in CB_S_4), 2.4% in CB_S_4), the holes never average below 5% in any run, and no contour setting moves those features into the accuracy band occupied by a step. A single tolerance figure quoted for a component of this kind would therefore be wrong for most of its features.

4.7 Wall-to-wall uniformity is not controllable by contour parameters

The preceding sections concern the mean dimension of a feature. A separate and equally important question for precision manufacturing is the spread between nominally identical features produced in the same run: whether the five walls of a single upper tie plate coupon come out the same as each other.

This was tested by modelling the wall range within a run (the difference between the largest and smallest of the five wall measurements) against the four DoE factors. The result is unambiguous:

$$R^2 = 0.097, \qquad \text{no term significant at } \alpha = 0.05. \tag{4.5}$$

Less than 10% of the variation in wall-to-wall uniformity is explained by the contour parameters, and none of the individual factors is statistically significant. The contour parameters can shift the dimensions of the walls in a similar direction, as demonstrated in Sections 4.3 and 4.4, but they do not appear to control the variation between individual walls.

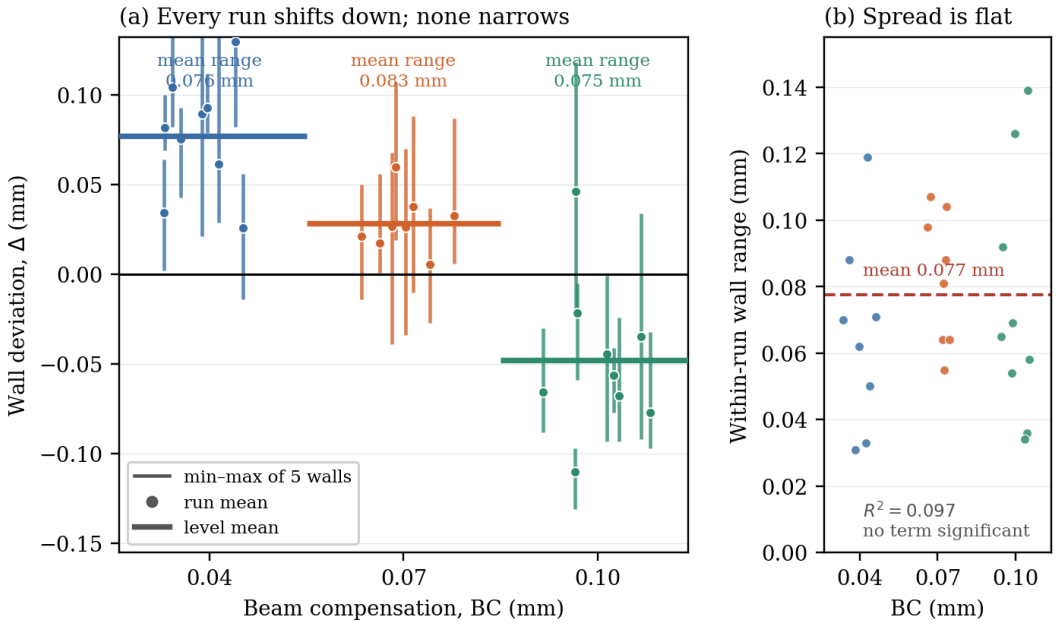


Figure 4.6: Wall-to-wall uniformity in the upper tie plate. (a) Each line spans the five wall deviations of one run; the lines shift down with compensation but keep the same length. (b) Within-run range against compensation.

Figure 4.6 shows this directly. Each vertical line spans the smallest to largest wall deviation of one run, plotted at the compensation applied to it. As compensation increases, the lines move down the axis, but their lengths remain similar.

The mean within-run range was 0.077 mm, corresponding to a standard deviation of

approximately 0.033 mm across the five walls. This exceeds the 0.021 mm pure-error estimate from the centre-point replicates, indicating that the variation between walls is greater than the repeatability of the process and cannot be attributed solely to measurement noise.

This is an important negative result because it shows a limitation of contour parameter optimisation. The remaining variation is likely influenced by factors that were not investigated in this study, such as local powder-bed conditions, recoater interaction, thermal effects, position on the build plate and gas flow, or measurement variation. These factors were not systematically varied or recorded and therefore cannot be separated using the present data.

The practical implication is that contour compensation can shift the wall dimensions towards the nominal value, but it does not necessarily reduce the variation between walls. Therefore, achieving a tighter manufacturing tolerance requires not only accurate compensation but also control of the additional factors contributing to wall-to-wall variation.

4.8 Process limit: bore closure

Run CY_7, at 170 W, 200 mm/s and 0.10 mm beam compensation, produced a completely closed bore in the smallest cylinder feature: the measured inner diameter was 0.000 mm against a 0.5 mm nominal.

This run combined the highest contour energy input in the cylinder design (E_L = 0.85 J/mm) with the largest beam compensation. The two settings do not act in the same direction. For an internal feature, inward compensation moves the scan path away from the opening on both sides, so a compensation of 0.10 mm would, on its own, enlarge the bore by approximately $2 \times 0.10 = 0.20$ mm relative to the lowest-compensation condition. The closure therefore occurred despite the maximum compensation, not because of it. The more plausible cause is the high energy input. A wider melt pool and greater heat conduction into the enclosed powder promote partial sintering and particle adhesion inside a 0.5 mm opening. With a sufficient build-up of such particles, the remaining gap can bridge completely.

This observation is consistent with Maleki et al. [25], who reported that small holes are susceptible to closure through powder adhesion and incomplete powder removal. It provides an empirical process limit for the investigated machine, material and parameter range. A 0.5 mm bore did not remain open at the highest contour energy input tested, even with maximum compensation applied. The result comes from a single, unreplicated run and should be read as a warning boundary rather than a quantified threshold.

Since the bore was physically closed rather than simply measured as zero, this condition was excluded from the regression analysis. Including it as a zero value would have introduced an extreme observation that could disproportionately influence the fitted model. However, the result was retained as an important practical observation and design guideline.

4.9 Surface characterisation results

4.9.1 Scope of the confocal dataset

Fifty-one areal surface measurements were acquired across three geometry families. The selection criterion differed between them, and this determines what each can support.

For the thin-wall and upper tie plate families, the five coupons with the best dimensional performance in each geometry were measured, so that the surface condition associated with dimensionally acceptable parts could be established. Because these coupons were chosen on a response rather than by design, the resulting subsets are not orthogonal in the process factors, and the two are confounded in different factor pairs. In the five TW coupons, contour power and scan speed are perfectly confounded ($r = -1.000$): the three distinct conditions present, 130 W/500 mm/s, 150 W/350 mm/s and 170 W/200 mm/s, lie on a single diagonal through the factor space. In the five UT coupons, scan speed is uncorrelated with power ($r = 0.000$), but power and beam compensation are perfectly confounded ($r = -1.000$), the three power levels occurring only alongside compensations of 0.10, 0.07 and 0.04 mm respectively. Pooling the subsets removes neither.

Table 4.8: Overview of confocal surface measurements acquired across three geometry families.

Family	Surface type	Samples	Maps	Analysis supported
TW	Vertical wall	5	30	Descriptive, energy-density trend
UT	Vertical wall	5	5	Paired comparison (wall vs bore)
UT	Internal bore	5	5	Paired comparison (wall vs bore)
OH	Down-skin (45°)	11	11	Response surface model
		Total	**51**	

No parameter-roughness model is therefore fitted to the TW or UT data. Those results are reported as descriptive trends and controlled pairwise contrasts, in Sections 4.9.2 and 4.9.3. The overhang family is the exception: all eleven specimens of a complete factorial design were measured, and response surface models are fitted in Section 4.9.4.

4.9.2 Vertical wall roughness and energy density dependence

The five TW coupons provide 30 individual surface measurements, summarised in Table 4.9. Ordered by linear energy density $E_L = P/v$, the height parameters are monotonic. The two coupons at the lowest energy density tested, TW_1 and TW_11 at 0.26 J/mm, have mean S_a of 13.9 and 13.4 µm; the coupon at the highest, TW_15 at 0.85 J/mm, reaches 7.4 µm, with TW_20 and TW_21 at 0.43 J/mm

falling between at 8.4 and 8.3 µm. Across that range, S_a falls by a factor of 1.8 and S_z from 221 to 103 µm, while S_{sk} rose from +0.04–0.14 to +0.88 across the three energy-density levels. Within the tested window a higher contour energy input produces a smoother vertical side-skin.

Table 4.9: Per-sample averages of confocal surface parameters on the TW vertical wall faces (each value is the mean of six individual wall measurements on that sample).

Sample	S_a	S_z	S_{10z}	E_L	S_{sk}
TW_1	13.9	195.8	164.8	0.26	+0.14
TW_11	13.4	221.0	180.6	0.26	+0.04
TW_15	7.4	102.8	77.8	0.85	+0.88
TW_20	8.4	112.0	90.7	0.43	+0.83
TW_21	8.3	111.9	92.5	0.43	+0.84
Mean	**10.3**	**148.7**	**121.3**	**0.446**	+0.55
SD	3.1	55.4	47.6	0.241	0.42

At 0.26 J/mm, the surfaces had deep valleys and approximately symmetric height distributions, with S_{sk} close to zero (+0.04 to +0.14). At 0.85 J/mm, the valleys were shallower while peak features remained, giving a clearly positive S_{sk} of +0.88, as listed in Table 4.9. This is consistent with a shift from a texture shaped by incompletely consolidated contour tracks, where valleys and peaks contribute similarly, to a smoother track surface on which adhered, partially melted particles dominate the residual texture. It matches the melt-track- and particle-dominated surface regimes described by Fox et al. [22].

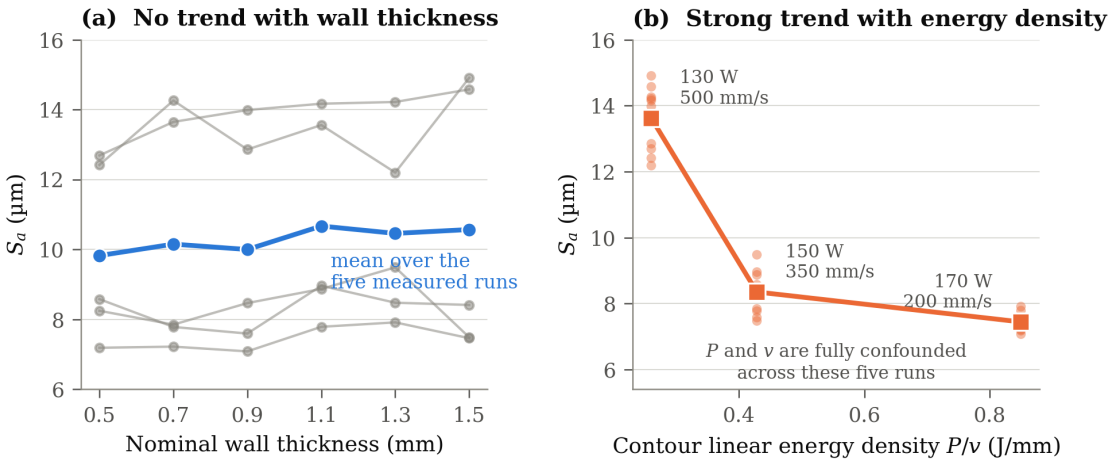


Figure 4.7: Surface roughness (S_a) of the five TW samples grouped by contour linear energy density.

The practical consequence is that S_a and S_{sk} must be read together. The smoothest surfaces measured here are also the most strongly peak-dominated, so optimising for mean height alone does not minimise the functionally relevant protrusions.

A further comparison shows that beam compensation had no measurable effect on side-skin roughness at fixed energy input. TW_20 and TW_21 share contour power, scan speed and border count and differ only in beam compensation, 0.04 against 0.07 mm; their mean S_a values are 8.40 and 8.30 µm, a difference of 0.10 µm. Taken with the energy-density ordering above, this indicates that within the tested window the dimensional and surface responses are controlled by different factors: beam compensation sets the dimension without penalising the finish, and contour energy input sets the finish.

4.9.3 Internal versus external surface roughness

The UT geometry provides a paired comparison that the TW geometry cannot: each coupon contributes one external wall surface and one internal bore surface measured under identical conditions. Because both surfaces on a coupon experienced the same parameters, the parameter effects cancel within each pair, and the comparison between surface types is valid regardless of which parameters were used.

The paired comparison ($n = 5$ coupons) is given in Table 4.10.

Table 4.10: Paired comparison of bore (internal) and wall (external) surfaces measured on the same five upper tie plate coupons. p-values from paired t-tests, $n = 5$.

Parameter	Bore ID	Wall	Difference	p
S_a (µm)	10.47	8.57	+1.90	0.030
S_z (µm)	146.1	106.8	+39.4	0.005
S_{10z} (µm)	107.9	88.9	+19.0	0.015
S_{dr} (%)	34.3	27.6	+6.7	0.008

Internal bore surfaces are rougher than external wall surfaces on every metric, in every coupon, with all four differences significant at $\alpha = 0.05$. The consistency of the direction across all five pairs is as informative as the p-values: with $n = 5$ this is the strongest possible unanimity.

The effect is proportionally larger on the extreme-height parameters than on the mean-height parameter. Bore S_a exceeds wall S_a by 22%, whereas bore S_z exceeds wall S_z by 37%. A difference concentrated in the extremes rather than the mean indicates that the bore surfaces carry a population of tall isolated features, most plausibly partially melted particles adhering to the downward-facing and inward-facing portions of the bore, where they are neither re-melted by a subsequent pass nor swept away by the recoater, rather than a uniformly coarser texture. The elevated S_{dr}, which quantifies the additional interfacial area created by the texture, points the same way.

This result pairs directly with the dimensional finding of Section 4.4.2. Internal and external surfaces differ both in size response to compensation, with opposite signs, and in surface finish, with internal surfaces consistently worse. The internal/external

distinction is therefore not a modelling convenience introduced for the regression; it is a real physical division that appears independently in two unrelated measurement modalities.

The UT wall mean of 8.57 µm sits close to the TW coupons at 0.43–0.85 J/mm (8.05 µm), which is expected since four of the five UT coupons lie in that energy-density range. The absolute values are consistent with published side-skin roughness for PBF-LB: Zhang and Yuan [11] report vertical-surface S_a below 15 µm for 316L, and Patel et al. [13] report 11–26 µm under core-parameter variation and below 10 µm with tuned border parameters, although in Ti-6Al-4V.

One contrast within the UT set isolates a single factor. UT_18 and UT_21 were produced at identical contour power, scan speed and beam compensation (150 W, 350 mm/s, 0.07 mm) and differ only in the number of contour passes. The coupon built with two borders is smoother on every parameter: S_a falls from 9.63 to 7.47 µm, S_z from 148.2 to 92.6 µm and S_{10z} from 108.6 to 82.1 µm, while skewness rises from +0.65 to +1.37. The reduction is largest in the peak-to-valley measures and the surface becomes more strongly peak-dominated, the signature expected if the second contour pass re-melts the first, consolidating the boundary and removing the deep inter-track valleys while leaving adhered particles as the residual texture. This is the re-melting mechanism reported by Yasa et al. [17] operating within a layer rather than as a separate scan. The comparison rests on a single pair without replication and is reported as an observation consistent with an established mechanism rather than as a quantified effect. It is nonetheless the largest single difference in the UT surface dataset, and it stands against the dimensional finding of Section 4.5.3 that border count has no resolvable effect on size.

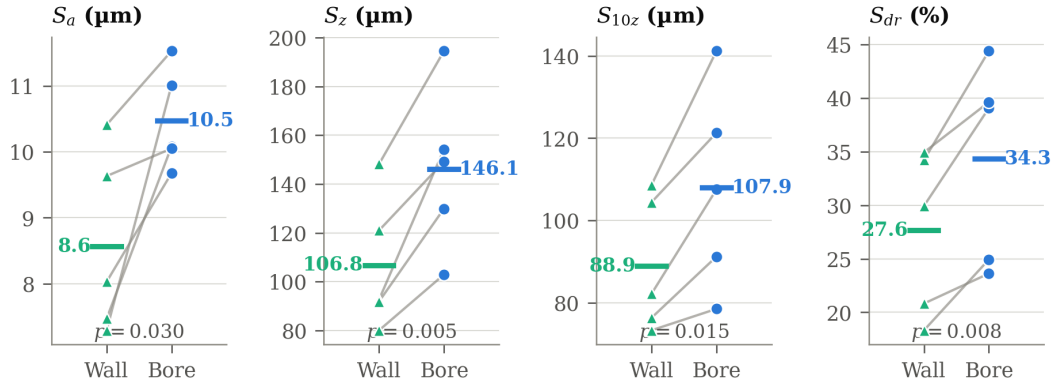


Figure 4.8: Each line connects the external wall and internal bore surface of one upper tie plate coupon, measured under identical process parameters so that parameter effects cancel within the pair. Heavy bars are group means. All five coupons slope the same way for every parameter; p-values are from paired t-tests, $n = 5$.

4.9.4 Overhang surfaces

Down-facing surfaces are substantially rougher than any vertical surface measured in this work. Mean S_a on the 45° struts was 29 µm against 8.6 µm on the upper tie plate walls, and peak-to-valley heights of 220–290 µm against roughly 110 µm. Down-skin quality is therefore governed by a different problem from side-skin quality, and the down-skin parameters were varied independently for that reason.

Within the tested ranges, the down-skin parameters shift peak-to-valley height but do not control mean height. S_{10z} and S_z both fit a two-term model in beam compensation and scan speed ($R^2 = 0.63$), with both coefficients negative: raising compensation from 0.04 to 0.10 mm reduces S_z by 22 µm and raising speed from 800 to 1200 mm/s by a further 16 µm, each around twice the centre-point repeatability. S_a fits nothing: no factor approaches significance, yet it varies with a standard deviation of 2.7 µm against a repeatability of 0.79 µm. The variation is real but unexplained by these factors.

Table 4.11: Confocal surface measurements on the eleven overhang down-skin specimens, with the down-skin border settings of each. All values in µm except S_{sk} (dimensionless). Specimens marked † are the centre-point replicates.

Specimen	P (W)	v (mm/s)	δ (mm)	$\mathbf{S_a}$	$\mathbf{S_{10z}}$	$\mathbf{S_z}$	$\mathbf{S_{sk}}$
OH_1	80	1200	0.10	30.4	230.2	254.2	+0.31
OH_2	120	800	0.10	27.0	225.0	256.3	+0.14
OH_3†	100	1000	0.07	27.8	245.3	264.8	+0.29
OH_4	80	1200	0.04	26.2	223.3	250.2	+0.12
OH_5†	100	1000	0.07	28.8	230.5	246.2	−0.14
OH_6	120	800	0.04	33.7	258.8	289.6	−0.16
OH_7	80	800	0.04	33.0	263.9	288.9	−0.07
OH_8	120	1200	0.10	27.6	220.8	247.1	+0.07
OH_9	80	800	0.10	26.1	235.2	248.0	+0.07
OH_10	120	1200	0.04	31.1	248.6	266.4	+0.06
OH_11†	100	1000	0.07	27.3	243.6	267.5	+0.14
Mean				**29.0**	**238.7**	**261.7**	+0.08
SD				2.7	14.5	15.6	0.15
Min				26.1	220.8	246.2	−0.16
Max				33.7	263.9	289.6	+0.31

Both significant effects act in the direction of reduced energy into the powder beneath the down-facing surface: a faster scan deposits less, and a larger compensation moves the border away from the unsupported edge. This is the opposite sense to the contour result of Section 4.9.2, where higher energy density gave smoother vertical walls, and it is consistent with the positive S_{sk} on eight of eleven specimens, which indicates surfaces dominated by adhered particles rather than pits.

The practical consequence is that parameter selection alone is not sufficient for down-facing surfaces, as shown in Table 4.11. Moving from the worst to the best

combination tested, OH_6 to OH_8, improves S_z from 290 to 247 µm, a reduction of about 15%, but leaves the surface roughly two to three times rougher than a vertical wall. Where down-skin finish is functionally important, orientation, support strategy or post-processing must carry the requirement; the down-skin parameters can only reduce the severity.

4.10 Summary of verified results

1. **The dimensional error is a constant offset of approximately** -0.055 **mm**, independent of nominal feature size over the 0.5–1.5 mm range. The slope of deviation against nominal size is -0.006 mm/mm (SD 0.020), indistinguishable from zero. Compensation is therefore a single number, not a size-dependent function.
2. **Reported percentage deviations are misleading.** The apparent threefold degradation from 4.9% to 14.6% as walls thin from 1.5 to 0.5 mm is arithmetic, not physical.
3. **Beam compensation is the dominant controllable factor**, with a slope near the geometric expectation of ± 2 mm per mm on both external (-2.085 walls, -2.093 external bores) and internal ($+1.823$ bore inner diameters) surfaces.
4. **Internal and external features respond to compensation in opposite directions.** No single global value nulls both. Required settings span 0.026 to 0.108 mm.
5. **Contour scan speed is significant but secondary**, at -1.1×10^{-4} mm per mm/s on walls and $+1.5 \times 10^{-4}$ on bores; approximately one quarter the influence of compensation across the tested ranges.
6. **Contour laser power was not significant** ($p = 0.35$–0.80) over the tested 130–170 W range, most plausibly because that range was too narrow.
7. **Number of borders was not significant**, with a mean difference of 0.009 mm against a 0.021 mm noise floor.
8. **Wall-to-wall uniformity is not controllable** by the four contour factors ($R^2 = 0.097$, no significant terms).
9. **Internal surfaces are rougher than external surfaces** on every areal parameter measured, in every coupon (S_a +1.90 µm, $p = 0.030$; S_z +39.4 µm, $p = 0.005$).

4.11 Gaps in the current dataset

The following items are outstanding. They are listed here rather than deferred to the future work chapter because each one bounds a claim made above, and a reader should know which conclusions are provisional.

1. **Measurement and process variation are not fully separated.** Dimensional annotations on LOM images are placed manually by the researcher, introducing a human-dependent component to each reading. A preliminary repeatability check was performed by taking multiple measurements from the same image, confirming that the annotation procedure itself is repeatable. However, small variations were observed between repeated measurements; these should not be disregarded entirely, as they could account for part of the minor unexplained deviation trends.
2. **Confocal coverage is insufficient for modelling.** Measuring side-skin surfaces on 12–15 of the existing 26 upper tie plate coupons, selected to span the factor space, would convert the roughness data from a paired comparison into a modellable response and would allow the surface-quality half of the research question to be answered.
3. **The overhang confocal data lack a dimensional counterpart.** All eleven overhang samples have known down-skin border parameters (power 80–120 W, speed 800–1200 mm/s, beam compensation 0.04–0.10 mm) and surface models were fitted for S_{10z} and S_z, but no dimensional measurements were taken on these specimens. The overhang results therefore contribute to the surface-quality analysis only.
4. **The hexagonal porous plate geometry was not part of the Print 2 DoE build.** It was included only in Print 3, which was dedicated to post-processing evaluation, and therefore carries neither dimensional nor surface data within the DoE framework, although its constituent features are covered by representative test coupons.
5. **Compensation values at the range edges require confirmation coupons.** The bore-ID optimum of ≈ 0.108 mm sits at the boundary of the tested range, and the external bore diameters have no zero crossing within it (minimum residual deviation ≈ -0.2 mm); neither should be adopted as a machine setting without verification builds.

5

Discussion

This chapter interprets the results of Chapter 4 in relation to the research questions and the existing literature. Section 5.1 discusses the trend of the dimensional error and why it matters for how AM dimensional data are reported. Section 5.2 examines the influence of feature class on compensation response, and Section 5.3 defines the feature range over which contour optimisation is effective. Section 5.4 examines the residual geometry dependence. Section 5.5 discusses the parameter hierarchy and the negative results. Section 5.6 discusses what contour optimisation cannot achieve. Section 5.7 discusses the surface quality results. Section 5.8 summarises the findings as process design guidelines and their industrial implications, and Section 5.9 presents the study limitations.

5.1 Central observation: approximately constant offset

The finding that the dimensional error is a constant offset rather than a scaling error has a significance beyond this particular process window, because it bears on a reporting convention that is widespread in the additive manufacturing literature.

Dimensional accuracy in AM is very commonly reported as a percentage of nominal. Doing so is entirely reasonable when the error mechanism is proportional; uniform thermal shrinkage, for instance, genuinely does scale with dimension. But when the error mechanism is a fixed offset, as observed in the current study, a percentage-based report generates an apparent trend that has no physical content. Table 4.2 shows a threefold worsening from 4.9% to 14.6% across the thickness series, and a reader encountering only that row would reasonably conclude that thin walls suffer from some additional mechanism that thick walls escape. The signed millimetre data show that they do not: every wall is displaced by the same amount, and the percentage trend is a constant absolute deviation divided by d_{nom}, and nothing more.

This offers a partial reinterpretation of a well-established observation in the literature. It is frequently reported that dimensional accuracy degrades as features become thinner [26, 25], and López-García et al. [28] report relative errors of 13–16%

for 316L walls below 750 µm against 2–15% for wider walls, a pattern quantitatively similar to Table 4.2. The present results do not contradict those findings; the relative errors are real and they do matter to a designer working to a proportional tolerance. What the results suggest is that at least a part of the effect commonly attributed to thin-wall thermal behaviour may be the result of a size-independent offset. Distinguishing the two requires signed data in absolute units, which much of the published work does not report.

The limitation on this claim must be stated equally clearly. The thin-wall series here spans 0.5 to 1.5 mm. Below 0.5 mm, where the wall approaches the melt pool width itself and where Leicht et al. [34] report genuine changes in grain morphology and crystallographic texture, and where Wróbel et al. [35] report melt pool asymmetry arising from powder denudation, there is every reason to expect additional size-dependent mechanisms to appear. The constant-offset result is a statement about walls in the 0.5–1.5 mm range and is not meant to be a general law.

The engineering consequence is nevertheless substantial and favourable. A constant offset is correctable by a single machine setting. A scaling error would require compensation to be a function of local feature size, which for a lattice or filter plate containing many different feature sizes would demand either per-feature parameter assignment or acceptance of a size-dependent residual error.

5.2 Response depends on feature class more than feature size

The central result of this thesis is that internal and external surfaces respond to beam compensation with slopes of similar magnitude and opposite sign: $+1.823$ for bore inner diameters against -2.093 and -2.085 for external bore surfaces and walls.

5.2.1 Why a slope of 2 makes sense

That both magnitudes approach 2 provides strong support for the measurement and the geometric model. Beam compensation is defined as an inward offset of the laser path from the nominal CAD boundary. For an external feature such as a wall, the offset is applied on both faces, reducing the fabricated thickness by 2δ. For an internal feature such as a bore, the same inward offset moves the scan paths away from the solid on both sides, increasing the fabricated opening by 2δ. The expected slopes are therefore -2 and $+2$, respectively, consistent with the unified relation discussed in Section 4.4.4. The measured slopes of -2.09 and $+1.82$ are close to these ideal values.

This agreement indicates that the dimensional response in this process window is primarily governed by geometric track placement rather than thermal effects. The similar slope magnitudes for walls and internal bores, despite their different thermal environments, suggest that melt pool width remains sufficiently stable for laser path placement to be the dominant factor determining the final dimensions. The small

deviations from the ideal ±2 response indicate that other effects, such as residual melt pool behaviour or measurement uncertainty, may contribute but do not dominate the observed response. Further geometry-dependent effects are discussed in Section 5.4.

5.2.2 The practical conflict

The practical consequence is uncomfortable. The compensation values required to null the different feature classes span 0.026 to 0.108 mm, while the build processor applies one value per part. A part such as the upper tie plate, which by its nature contains bores and struts in the same body, cannot be dimensionally correct in both simultaneously with a single setting.

This is a conflict that the existing literature on beam compensation does not appear to address directly, and the reason is instructive. Beam compensation is commonly treated as a fixed machine constant rather than as an experimental factor. Contour effects on surface and dimensional quality are widely reported [10, 11, 14], but the offset itself is rarely varied within a response-surface framework. Habeeb and Chou [15] do treat contour offset as a variable, but on inclined surfaces rather than on paired internal and external features within one part. Studying compensation on a coupon that contains only external features, as most benchmark studies do, would find a single clean optimum and would never surface the conflict. It becomes visible only when both feature classes are measured on the same part under the same parameters, which is what the upper tie plate coupon happens to enable.

Three resolutions are available to a practitioner, and the study permits each to be quantified rather than merely listed:

1. **Prioritise one class and accept the residual on the others.** Choosing the wall optimum of 0.079 mm leaves bore inner diameters undersized by approximately 0.053 mm, and external bore diameters undersized by more than 0.196 mm. Whether that is acceptable is an application question, but it is now a quantified one.

2. **Split the part.** Where the build processor permits per-body parameter assignment, features of different class can be separated into different bodies carrying different compensation values. This is the technically correct answer and is achievable on the SLM 280, which already supports per-part assignment, the same capability that made this DoE possible in a single build.

3. **Compensate in CAD rather than in the machine.** Applying the difference as a geometric offset to the model boundary before slicing achieves per-feature compensation without requiring the machine to support it. The disadvantage is that the correction is then baked into the model and must be reversed if parameters change.

5.2.3 Evidence from an independent measurement approach

The distinction between internal and external features is not solely a result of the regression analysis. The confocal measurements presented in Section 4.9 show that the internal bore surfaces were rougher than the external wall surfaces for all measured surface parameters and across the investigated coupons. The difference was also more pronounced for the extreme-height parameter S_z (+37%) than for the mean roughness parameter S_a (+22%).

This distinction is further supported by the fact that two independent measurement methods show the same difference between internal and external features. Dimensional measurements obtained using optical microscopy and surface topography measurements obtained using confocal microscopy both distinguish the two feature types. This provides stronger evidence that the observed difference is related to the physical characteristics of the surfaces rather than a result of how the features were grouped in the analysis.

A possible explanation is related to the different powder-bed conditions surrounding internal and external surfaces. For an internal bore, the region immediately outside the melt track consists of enclosed powder that may be heated but not fully consolidated. This powder is neither removed by the recoater nor necessarily re-melted by a neighbouring hatch track. Partially melted particles can therefore remain attached to the surface. This can increase surface roughness, particularly through isolated high peaks, which is consistent with the larger difference observed in S_z, and may also result in a small amount of additional material extending beyond the intended surface.

On an external surface, the equivalent region is open powder bed that is recoated each layer. This mechanism is consistent with the accounts of partially melted particle attachment given by Strano et al. [18] and Patel et al. [13]; it is also consistent with the findings of Fox et al. [22], in which the transition between particle-dominated and melt-track-dominated surfaces is detectable in the surface texture parameters themselves.

The mechanism is offered as an interpretation consistent with the data, not as a demonstrated result. No cross-sectional metallography or CT of the bore surfaces was performed in this work; a microstructural study is included in the later scope of the project.

5.3 Feature range where contour optimisation can be relevant

The results of Sections 4.4 and 4.6 together define the range over which contour compensation is effective. Where a feature is thin enough that the contour forms a substantial fraction of its cross-section, the relation $\Delta = a \pm 2\delta$ holds and the dimension is directly controllable. Where the feature is embedded in bulk material, the contour becomes a thin skin on a cross-section formed predominantly by hatch

exposure, and the border parameters no longer reach the surface that determines the dimension.

The clearest evidence for this limit is the comparison of two bores of similar diameter. Through a 0.5 mm web in the upper tie plate, the bore responded to beam compensation at +1.823 mm per mm with $R^2 = 0.892$. Surrounded by 3–5 mm of solid material in the cube benchmark, the equivalent bore showed no response to any factor and instead a constant undersize of −0.162 mm. The feature geometry and the machine were the same in both cases; only the surrounding material volume differed. This indicates that the transition is governed by the ratio of contour area to total cross-sectional area rather than by the nominal size of the feature itself.

This has a direct consequence for how the guidelines of Section 5.8 should be applied. Contour compensation is the correct instrument for walls, webs, thin sections and bores through thin material. For bulk features, the appropriate correction is a dimensional allowance applied in CAD: the holes of the cube benchmark, for example, require approximately +0.16 mm added to the nominal diameter, or alternatively a study and optimisation of the hatch parameters, where the contour plays a lesser role. Attempting to tune border parameters for such features uses up build time without moving the dimension.

The boundary between the two regimes has not been located quantitatively in this work. The thin-wall series extends only to 1.5 mm, while the cube benchmark features sit in 3–5 mm of surrounding solid, so the transition lies somewhere between approximately 1.5 and 3 mm. A dedicated series spanning this range would be required to establish where and how sharply it occurs.

5.4 Residual geometric dependence

Although feature class explains the largest difference in the response, the required compensation also differs between similar features in different geometry families. The compensation needed to null an external wall is approximately 0.041 mm for isolated thin walls, 0.049 mm for cross walls and 0.079 mm for the walls of the upper tie plate.

All three are external-surface values with the same sign and the same order of magnitude, so the dominant physics is common. However, the compensation required for the upper tie plate walls is almost twice that of the isolated thin walls. This difference is larger than the observed measurement noise of approximately 0.021 mm, indicating that the geometry itself may influence the required compensation.

Several candidate mechanisms are consistent with the observation, and the present data do not discriminate between them:

- **Thermal environment.** The upper tie plate walls sit within a lattice, surrounded by other solid material, whereas the thin-wall coupons present isolated walls surrounded by powder. The surrounding solid provides a conduction path that the powder does not, and the resulting difference in local thermal history would plausibly alter melt pool width and hence effective track placement.

- **Contour-hatch interaction.** The upper tie plate walls are thicker relative to the contour track and therefore contain a hatch region; the thinnest walls of the TW family are essentially entirely contour. Zhang and Yuan [10] show that the transition zone between contour and hatch is itself governed by the contour offset and the relative energy densities, so a wall containing hatch is not simply a thicker version of one that does not.
- **Measurement location.** The measured wall features differ in their position relative to junctions and free ends between the families, and no systematic study of measurement position was performed.

The cross walls provide an intermediate case between the isolated thin walls and the upper tie plate walls. Their compensation value (0.049 mm) lies between the thin-wall value (0.041 mm) and the upper tie plate value (0.079 mm). Since the cross walls contain border intersections while the thin walls do not, this trend suggests that the local geometric environment may influence the required compensation. However, the limited number of geometry classes means that this observation remains suggestive rather than conclusive. A design rule derived from a single coupon type should therefore not be transferred to a different geometry without verification, which is precisely the caution that Gradl et al. [26] draw from their geometric feature reproducibility study, and that motivated the multi-geometry design adopted here.

5.5 Parameter hierarchy exhibited in the results

Ordered by influence on dimensional accuracy across the tested ranges, the four factors fall into a clear hierarchy: beam compensation (0.125 mm across its range on walls) dominates, contour scan speed (0.033 mm) is significant but roughly four times weaker, and contour laser power and number of borders are not significant at all.

5.5.1 Scan speed

The scan speed effect is coherent with the compensation effect and reinforces the geometric interpretation. Raising scan speed lowers linear energy density and narrows the melt pool; a narrower contour track places less material outside the intended path, so external features shrink further and internal openings enlarge. The observed signs, negative on walls and positive on bores, match this exactly, and mirror the sign reversal seen for compensation.

The relationship between speed and melt pool geometry is well established for 316L. Zhang et al. [33] report that at constant power the melt pool width-to-depth ratio shifts from keyhole-like to conduction mode as speed increases, and that at constant linear energy density the pool dimensions still shrink with increasing speed while instability grows. The present result is consistent with operating in the conduction-dominated part of that space, where the response is monotonic and moderate rather than abrupt.

Practically, the speed effect is a second-order trim rather than a primary control.

Given that it acts in opposite directions on internal and external features, it also cannot be used to reconcile the compensation conflict of Section 5.2: moving speed to improve bores makes walls worse, and vice versa.

5.5.2 Laser power

Contour laser power was not statistically significant for any of the dimensional responses ($p = 0.35$–0.80). This may appear surprising because laser power directly affects the melt pool and is widely reported as an important PBF-LB process parameter.

However, the result should be interpreted in relation to the experimental design. The investigated power range was relatively narrow, from 130 to 170 W, corresponding to a variation of approximately ±13% about the baseline. In comparison, the scan speed ranged from 200 to 500 mm/s, a span of ±43%. In terms of linear energy density, the power axis covers a factor of 1.31 and the speed axis a factor of 2.5.

The difference is even larger when expressed as linear energy density at the design centre. At 350 mm/s, the power range spans 0.37–0.49 J/mm, a change of about 0.11 J/mm. At 150 W, the speed range spans 0.30–0.75 J/mm, a change of about 0.45 J/mm. If the dimensional response is broadly a function of P/v, the power range would therefore be expected to produce roughly a quarter of the speed effect. That is about 0.008 mm on walls and 0.011 mm on bores, both well inside the 0.021 mm noise floor.

Therefore, the non-significant result should not be interpreted as evidence that contour laser power has no effect on dimensional accuracy. Rather, it indicates that no statistically detectable effect was observed within the power range investigated. A wider power range, comparable to the scan-speed range in terms of energy-density variation, would be required to assess the influence of contour laser power more conclusively.

5.5.3 Number of borders

The number of border passes produced a mean difference of 0.009 mm, well inside the noise floor. Its effect on the derived compensation values is 0.003–0.004 mm, an order of magnitude below the values themselves.

This is a useful practical result, and it acquires a second dimension from the surface data. The single controlled contrast available in the confocal set, UT_18 against UT_21 at identical power, speed and compensation, shows the coupon built with two borders to be substantially smoother: S_z falls from 148.2 to 92.6 µm and S_a from 9.63 to 7.47 µm (Section 4.9.3). The two observations are consistent with one another rather than in conflict. A second contour pass that retraces ground already melted, rather than extending the contour-defined zone outward, would be expected to leave the dimension unchanged while re-melting the boundary and consolidating the side-skin, which is the re-melting mechanism described by Yasa et al. [17]. Border count therefore appears to be dimensionally neutral but surface-active within this

window, which makes it a third lever alongside compensation and energy density rather than a factor that can simply be set for build time. The surface evidence rests on a single unreplicated pair and is treated accordingly in Section 5.9.

5.5.4 Curvature

The significant quadratic terms (beam compensation squared and scan speed squared for the external bore diameters, and scan speed squared for the square grid pores) indicate some curvature in the response. However, these effects are relatively small and do not materially change the estimated compensation values.

The presence of these quadratic terms also supports the use of the three-level experimental design with centre-point replicates. A two-level factorial design would not have been able to identify curvature, whereas the three-level design allowed the response to be tested for non-linearity. The responses were largely linear over the investigated ranges, and the analysis confirms that strong curvature was generally absent. This supports the use of the fitted models for interpolation within the investigated parameter ranges and increases confidence in the reported compensation values.

5.6 Limitation of contour optimisation

The wall uniformity result ($R^2 = 0.097$, with no significant terms) indicates that contour parameter optimisation has limited ability to reduce the variation in wall thickness. This is an important consideration for industrial application, since contour parameters primarily affect the average dimensional position rather than the spread of the measured values.

Contour parameters primarily shift the mean wall thickness rather than reduce its variation. With appropriate compensation, the measured wall thickness can be centred around the nominal value, but the spread of the measurements remains largely unchanged. Since a manufacturing tolerance defines an acceptable range of variation around the nominal dimension, contour optimisation can bring a process within specification only when its existing variation is already smaller than the tolerance band. If the inherent variation is larger than the allowable tolerance, reducing it might require addressing other sources of process variability.

The present experimental design cannot determine the source of this remaining variation because these factors were not systematically varied. Possible contributors include powder-bed condition, local recoating uniformity, position on the build plate and its relation to gas flow, layer-to-layer variation in deposited powder-layer thickness, and measurement variation. Measurement variation is particularly important because it cannot be separated from process variation in the current data.

It should also be noted that a negative result of this kind is only reportable because the design included genuine replicates. Without a pure-error estimate there would be no basis for asserting that 0.009 mm is inside the noise and 0.033 mm is outside it,

and a study lacking replicates would be unable to distinguish 'no effect' from 'effect not resolved'. This is a general argument for including replicate runs in PBF-LB DoE work, where they are often sacrificed to build-plate area.

5.7 Surface quality

The surface characterisation results warrant separate discussion for the overhang geometry, where a full model was fitted, and for the thin-wall and upper tie plate geometries, where only selective measurements were performed.

5.7.1 Overhang down-skin surfaces

The overhang geometry was the only family for which all 11 runs were measured by confocal microscopy, because dimensional deviation is not the primary quality metric for down-skin surfaces; surface roughness is the direct functional concern. The resulting models reveal a clear split: beam compensation significantly influenced the peak-to-valley metrics (S_{10z}, S_z) but had no detectable effect on arithmetic mean roughness (S_a). This distinction is physically plausible: beam compensation shifts the melt pool boundary relative to the overhang edge, which controls dross adhesion and the severity of isolated peak features, while the mean roughness of the down-skin texture is governed more by the layer-wise staircase geometry than by the contour offset. The practical implication is that beam compensation can be used to reduce extreme peak heights on overhangs without expecting a corresponding improvement in S_a.

5.7.2 Thin-wall and upper tie plate surfaces

For the TW and UT geometries, confocal measurements were limited to five representative samples per family, selected on the basis of their geometric deviation results. Dimensional accuracy was treated as the primary screening criterion because it carries greater practical weight for the application; surface characterisation was then targeted at the samples where parameter effects on geometry were most pronounced. This selective approach means the TW and UT surface data cannot support independent parameter-roughness models, and the influence of border parameters on surface quality for these geometries is addressed through paired comparison rather than regression.

The paired internal-external comparison is nonetheless a valid result precisely because pairing eliminates the parameter confounding: both surfaces on a coupon experienced identical border settings, so parameter effects cancel within each pair. The consistent finding, discussed in Section 4.9, was that internal surfaces were rougher on every metric, in every coupon.

5.7.3 Context within the literature

The absolute roughness values sit within the published range for PBF-LB side-skins. Zhang and Yuan [11] report vertical-surface S_a below 15 µm for 316L at low energy density, and Vu et al. [24] report up-skin $R_a \approx 10$ µm on 316L walls. Patel et al. [13] report 11–26 µm under core-parameter variation and below 10 µm with tuned border parameters, although for Ti-6Al-4V. The TW and UT wall values of 7–14 µm are consistent with these ranges, which gives confidence in the measurement protocol.

The energy-density trend observed here runs opposite to what might be expected from the dross literature, and the discrepancy is informative rather than contradictory. Zhang and Yuan [11] and Glaubitz et al. [14] both report side-skin finish degrading once contour energy density becomes excessive, through melt pool instability and dross formation. In the present data, side-skin roughness falls with increasing linear energy density across the whole tested window, from $S_a = 13.6$ µm at 0.26 J/mm to 7.4 µm at 0.85 J/mm. The skewness data of Section 4.9.2 explain why: the low-energy surfaces have near-symmetric height distributions, consistent with incompletely consolidated contour tracks, while the high-energy surfaces are smooth and peak-dominated, their residual texture consisting of adhered particles. The tested window therefore spans the transition from track-dominated to particle-dominated surfaces and lies entirely below the dross threshold those authors identify. Habeeb and Chou [15] obtained their best up-facing surface at 0.26 J/mm, the bottom of the present range, which places this window at or above their optimum throughout.

The practical reading is that the dross constraint is a ceiling not yet reached, rather than an active limit, and that a wider energy-density range would be required to locate it on this platform. An additional subset of 12–15 coupons from the DoE set would both convert the descriptive trend into a fitted model and establish where the trend reverses.

5.8 Process design guidelines

The results from Chapter 4 can be condensed into actionable compensation guidelines for PBF-LB production of 316L components on the SLM 280 platform. The two primary levers identified in this study, beam compensation for dimensional accuracy and contour energy input for surface finish, are treated separately below. The number of borders appears as a possible third, surface-related lever.

5.8.1 Compensation for external features

External features (walls, webs, and outer diameters) respond to beam compensation with a negative slope: increasing BC makes external dimensions smaller. Table 5.1 lists the recommended BC setting for each external feature class, the expected residual deviation at that setting, and the sensitivity to the secondary factors (power and scan speed).

For external features, the recommended BC values range from 0.026 mm (CY outer

diameter) to 0.079 mm (UT wall). The variation across geometry families reflects differences in the intercept a, which is sensitive to the local thermal environment of the feature. Geometries with greater thermal confinement (e.g., UT, where the wall is enclosed between two bores) require higher compensation than open geometries (e.g., CY, where the outer diameter is fully exposed), as seen in Table 5.1.

Table 5.1: Compensation guidelines for external features.

Feature	Set BC to	Expected residual	Design note
Free-standing wall, 0.5–1.5 mm (TW)	0.04 mm	$\approx 0 \pm 0.012$ mm	One value covers the whole 0.5–1.5 mm range; wall thickness does not enter the relation.
Intersecting wall (C_TW)	0.05 mm	$\approx 0 \pm 0.022$ mm	No additional oversizing was measured at the crossing nodes, so no local relief is needed at the junction.
Cylinder outer diameter (CY)	0.04 mm	-0.025 ± 0.009 mm	Zero crossing (0.026 mm) lies below the tested range, so 0.04 mm is the lowest validated setting. A setting of 0.03 mm would reduce the mean offset to about −0.007 mm but is untested. Shallower slope (−1.75) than a flat wall.
Square-grid web, 0.5 mm (SQ_F)	0.07 mm	$\approx 0 \pm 0.032$ mm	Conflicts with the pore optimum (0.045 mm) on the same part.
Tie-plate wall between bores (UT)	0.08 mm	$\approx 0 \pm 0.031$ mm	Roughly double the free-standing value; the surrounding lattice raises the required compensation.

The practical implication is that a single beam compensation value will not serve all external features equally. At a global setting of 0.06 mm the residual deviations are −0.06 mm on the cylinder outer diameter, −0.038 mm on isolated thin walls, −0.022 mm on cross walls, +0.014 mm on square grid webs and +0.040 mm on upper tie plate walls, so a single value holds the external wall-type features within approximately ±0.06 mm of nominal. The upper tie plate outer and mid bore diameters are the exception: their zero-crossing is negative and unreachable, and at 0.06 mm they remain undersized by approximately 0.2 mm. Those features cannot be brought to nominal by compensation at all and require a CAD-side allowance. Where per-body parameter assignment is available, the feature-specific values of Table 4.6 should be used instead.

5.8.2 Compensation for internal features

Internal features (bores, pores and cavities) respond with a positive slope: increasing beam compensation makes internal dimensions larger. Their zero-crossings, 0.045 mm for square grid pores, 0.073 mm for cylinder inner diameters and 0.108 mm for upper tie plate bore inner diameters, are, with the exception of the square grid

pores, higher than the external values of the same geometry, consistent with the greater thermal confinement of enclosed features.

One caution applies. The upper tie plate bore inner diameter zero-crossing at 0.108 mm sits just outside the tested range of 0.04–0.10 mm and is therefore a short extrapolation; confirmation coupons at 0.11–0.13 mm would be required before adopting it as a machine setting. The corresponding values for each feature type are presented in Table 5.2.

Table 5.2: Compensation guidelines for internal features. Internal features respond with the opposite sign to external features and generally require a higher setting. Columns as in Table 5.1.

Feature	Set BC to	Expected residual	Design note
Lattice pore, 2.0 mm	0.045 mm	±0.012 mm	Opposite sign to its own wall; both cannot be nulled on one part.
Bore ID > 0.5 mm	0.07 mm	±0.040 mm	Slope +1.41, the most attenuated and the noisiest response in the study.
Bore adjoined by thin web	0.10 mm	±0.018 mm	True optimum 0.108 mm sits just outside the tested range.
Bore ID ≤ 0.5 mm		*see note*	Manufacturable across most of the window, but closed completely in the single run at the highest energy input (170 W / 200 mm/s), even at maximum compensation (Section 4.8). Avoid the highest energy settings for bores of this size, or treat 1 mm as the lower bound where the parameter set is not controlled.

5.8.3 Surface finish guidelines

Surface roughness is mainly influenced by different parameters than dimensional accuracy. For the TW and UT confocal measurements, the arithmetic mean roughness, S_a, showed a negative correlation with linear energy density ($E_L = P/v$):

$$S_a \approx 13.2 - 7.8\, E_L \quad (\mu\text{m}) \tag{5.1}$$

with $r = -0.71$, $p = 0.021$ and $n = 10$. This relationship describes the measured samples but is not a DoE model. Since power and compensation were changed together in the UT samples, their individual effects cannot be separated. However, the controlled TW comparison showed that beam compensation had no clear effect on S_a when the energy input was kept constant. Expected roughness values for each surface type are provided in Table 5.3.

Table 5.3: Expected areal roughness by surface type, with the parameters that control it. Ranges are the measured span across the confocal dataset (Section 4.9). Energy-density guidance derives from a descriptive correlation across confounded subsets and indicates direction rather than predicting a value; see Section 5.8.3.

Surface	Expected S_a	Controlled by	Design note
Vertical wall, external	7–14 µm	Contour energy density; number of borders	Smoothest at the highest energy density tested, 0.85 J/mm (170 W / 200 mm/s), giving S_a = 7.4 µm. At 0.43 J/mm (150 W / 350 mm/s) $S_a \approx$ 8.3 µm. At the lowest tested, 0.26 J/mm, S_a rises to 13.6 µm, a factor of 1.8. A second border pass improved finish further in the one controlled comparison available.
Bore wall, internal	9.7–11.5 µm	Not resolved	Approximately 1.9 µm rougher than an external wall on the same coupon (p = 0.030), and 37% higher on S_z. Parameter dependence was not measured on these surfaces. Check post-process access at the design stage.
Down-skin overhang	26–34 µm	Geometry sets S_a; beam compensation sets peak height	Roughly three times the vertical-wall value, and no down-skin border parameter shifted S_a detectably. Raising beam compensation from 0.04 to 0.10 mm did reduce S_z by 22 µm and S_{10z} by 21 µm. Where mean roughness matters, reorient, support or post-process.

On this basis, roughness and dimensional accuracy can be addressed largely separately:

- **Dimensional accuracy** is set by choosing the beam compensation for each feature class using the $\Delta = a \pm 2 \times \mathrm{BC}$ relation.
- **Surface finish** is improved by increasing the linear energy density, through higher power and/or lower scan speed. At 170 W / 200 mm/s, note the bore-closure limit for 0.5 mm openings (Section 4.8).

The separation is not complete. Scan speed also shifts dimensions, by up to about 0.03 mm on walls and 0.045 mm on bores across the tested range. A change of speed made for finish should therefore be followed by a small compensation trim. With that caution, a practitioner can set compensation for dimensional targets and then adjust power and speed for surface quality. The number of borders may offer a further finish lever with no measurable dimensional cost.

5.8.4 Recommended starting range for parameters

1. **Beam compensation.** Set per feature class using Table 4.6. Where only one global value is available, 0.05–0.06 mm holds external wall-type features within

approximately ±0.06 mm; features whose zero-crossing is negative require a CAD allowance instead.

2. **Power and speed.** Higher linear energy density gives the smoother vertical wall within the tested window. At 170 W / 200 mm/s the measured S_a was 7.4 µm against 13.6 µm at 130 W / 500 mm/s. Where build rate matters more than finish, 150 W / 350 mm/s gives $S_a \approx 8.3$ µm at a substantially higher scan rate.
3. **Number of borders.** One border is sufficient for dimensional accuracy; the second changes the dimension by 0.009 mm against a 0.021 mm noise floor. Where side-skin finish matters, the single controlled contrast available here indicates that a second pass improves it materially (Section 5.5), and the trade is scan time against finish rather than against accuracy.
4. **Down-skin surfaces.** Expect $S_a \approx$ 26–34 µm, roughly three times the vertical-wall values, and note that S_a did not respond to any down-skin border parameter tested. The peak-to-valley metrics did: raising beam compensation from 0.04 to 0.10 mm reduced S_z by 22 µm and S_{10z} by 21 µm, both above the centre-point noise. Down-skin compensation is therefore worth setting where isolated tall features matter functionally, but mean roughness at this level requires post-processing.

These recommendations are valid within the tested envelope: SLM 280, 316L, 60 µm layer thickness, contour power 130–170 W, scan speed 200–500 mm/s and beam compensation 0.04–0.10 mm.

5.8.5 Implications for nuclear industry components

The demonstrations described in Section 2.6 make the relevant feature scale explicit. The Westinghouse spacer grid carries walls of approximately 250 µm, below the 0.5 mm lower bound of the present thin-wall series, so the constant-offset finding of Section 5.1 would need re-verification at that scale before transfer. Three implications follow.

Compensation is worth getting right, and it is cheap to get right. The uncompensated offset of approximately 0.055 mm is, on a 0.5 mm wall, an 11% error, which can be corrected by a single machine setting. No hardware change, additional process step or post-machining is required. For a component class whose economic case rests partly on eliminating post-processing, a software-side correction of this size is attractive.

Parts containing both feature classes force a decision that should be made explicitly. A filter plate or tie plate is exactly such a part: its pores and its webs are both functional and respond to compensation with opposite sign. Leaving a single global value in place does not avoid the decision, it makes it silently, correcting one class and leaving the other with a quantified error. The three resolutions set out in Section 5.2 should be chosen between deliberately. This appears to be a general property of perforated and lattice geometries rather than anything specific to these coupons.

Tolerance capability is set by uniformity, not by compensation accuracy. Because contour parameters do not control wall-to-wall spread, the achievable tolerance band on a multi-feature part is governed by the scatter documented in Section 4.7. Specification exercises should be based on that spread, and tightening it requires variables outside the contour parameter set.

The surface result carries a specific relevance here. Internal surfaces are both rougher and harder to reach for post-processing, and in a fuel assembly component the internal channel and pore surfaces influence flow behaviour, deposition and corrosion. The bore surfaces were rougher than external walls on every metric measured, with S_a 22% and S_z 37% higher, and the developed interfacial area ratio S_{dr} 6.7 percentage points higher, indicating correspondingly more surface available for those processes. The internal surfaces are therefore simultaneously the most functionally significant and the least tractable, which argues for addressing them at the design and parameter stage rather than relying on downstream finishing.

5.9 Limitations of the current study

Several limitations should be considered when interpreting these results.

- **Surface characterisation was selective rather than exhaustive.** Of the 117 coupons in the Print 2 DoE, 21 were measured by confocal microscopy: all eleven overhang specimens, and the five best dimensional performers from each of the thin-wall and upper tie plate families. Selecting the thin-wall and upper tie plate coupons on a dimensional response established the surface condition associated with dimensionally acceptable parts, but it also means those subsets are not orthogonal in the process factors, and the resulting confounding is described in Section 4.9. The consequence is that surface quality for those two geometries is addressed through descriptive trends and controlled pairwise contrasts rather than through a fitted model, and the surface-quality component of the second research question remains only partially answered. Measuring all 117 coupons would have been prohibitively time-consuming within the scope of a single thesis.
- **Contour-hatch interaction was not investigated.** Because the hatch parameters were held constant across all runs, the DoE captures only the effect of border parameters at that single hatch condition. Contour-hatch interaction (how border parameter optima shift when the infill strategy changes) is therefore outside the scope of this study. The compensation values reported in Chapter 4 are valid for the hatch and layer condition used, and should be re-verified before transfer to a different build profile.
- **The parameter ranges were asymmetric in energy-density terms.** The power range was substantially narrower than the speed range, which is the most likely reason for the power null result and limits what can be concluded about power.
- **Mechanical and metallurgical characterisation was outside scope.** No tensile, fatigue or fracture testing, no metallography, no porosity measure-

ment and no residual stress analysis were performed; these are planned for later stages of the industrial project, for which the present results serve as a foundation. Statements in this thesis are confined to dimensional and surface behaviour, and no claim is made about the mechanical consequences of the parameter sets studied.

- **A single material, machine and build.** All results derive from 316L on one SLM 280 system in a single build. Transfer to other alloys, machines or layer thicknesses requires verification. Glaubitz et al. [14] specifically caution that contour–roughness relationships established on one alloy and platform did not transfer to another, and the same caution should be applied to the compensation values reported here.

Despite these limitations, the study provides quantified, internally consistent and statistically adequate values for the tested envelope, together with a clear statement of what contour parameter optimisation can achieve.

6

Conclusion

This thesis investigated the influence of border (contour) scanning parameters (contour laser power, contour scan speed, beam compensation and number of border passes) on dimensional accuracy and side-skin surface quality in laser powder bed fusion of 316L stainless steel. Seven benchmark geometry families derived from nuclear fuel assembly features were manufactured on an SLM 280 system using per-part parameter assignment, allowing every design-of-experiments run to be produced within a single build. In total, 1805 dimensional measurements and 51 areal surface measurements were acquired and analysed through descriptive trend analysis in spreadsheets and response surface modelling in JMP.

6.1 RQ1: Which border scanning parameters most strongly influence dimensional accuracy and surface quality on precision-critical PBF-LB geometries?

Beam compensation is the dominant controllable factor by a substantial margin, producing a change of 0.125 mm in wall thickness across the tested range of 0.04–0.10 mm. Contour scan speed is significant but roughly four times weaker, at -1.1×10^{-4} mm per mm/s on external features and $+1.5 \times 10^{-4}$ on internal features, corresponding to 0.033 mm and 0.045 mm respectively across the tested range. Contour laser power was not statistically significant for any dimensional response ($p = 0.35$–0.80), and number of border passes produced a mean difference of 0.009 mm, inside the 0.021 mm experimental noise floor.

The power null result should be read as a limitation of the design rather than as a physical conclusion, for the reasons set out in Section 5.5. Number of borders was likewise dimensionally inactive, but is not therefore inconsequential: the single controlled surface contrast available showed a second contour pass reducing S_z by 38% at identical power, speed and compensation. It appears to be dimensionally neutral and surface-active, which makes it a third lever rather than a free choice.

For surface quality the question is only partially answered. The confocal subsets for

the thin-wall and upper tie plate geometries were selected on dimensional performance rather than designed, and are confounded in power and speed and in power and compensation respectively, so no parameter–roughness model is fitted to them. What they do support is a descriptive relation: mean height falls with contour energy density across the tested window, from $S_a = 13.6\,\mu m$ at $0.26\,J/mm$ to $7.4\,\mu m$ at $0.85\,J/mm$, placing the whole window in the particle-dominated regime rather than the dross-dominated one. The overhang geometry is the exception, having a complete factorial with every specimen measured: beam compensation was significant for S_{10z} ($R^2 = 0.628$, $p = 0.018$) and S_z ($R^2 = 0.626$, $p = 0.018$), while no term reached significance for S_a, whose full model gave $R^2 = 0.35$ at $p = 0.36$. Vertical-wall roughness remains unmodelled.

6.2 RQ2: How do these parameters affect geometric and surface quality for different features?

The dominant distinction in both dimensional and surface responses was feature class rather than feature size. Internally and externally bounded features showed opposite dimensional responses to beam compensation, with slopes of $+1.823$ mm/mm for bore diameters and approximately -2.09 mm/mm for external features. The magnitudes are close to the expected ± 2 mm/mm response, reflecting the opposite effects of contour displacement on internal and external boundaries. In contrast, wall thicknesses from 0.5 to 1.5 mm showed an approximately constant signed deviation of -0.055 mm. This indicates that the apparent reduction in relative accuracy at smaller wall thicknesses is primarily a consequence of a constant offset rather than evidence of a size-dependent dimensional mechanism.

Surface behaviour also differed strongly by feature class. Internal bore surfaces were consistently rougher than external walls, while the dominant parameters differed with surface orientation. On vertical surfaces, increasing contour energy density reduced S_a from 13.6 to 7.4 µm, whereas beam compensation had little measurable effect. On down-skin surfaces, the parameter influence was reversed: beam compensation reduced peak-related parameters such as S_{10z} and S_z, while no border parameter produced a clear change in S_a. Down-skin surfaces nevertheless remained substantially rougher than vertical surfaces, indicating that orientation and support conditions impose a stronger limitation than border optimisation within the tested range.

A residual geometry dependence remained in the dimensional response, with the compensation required to centre external features varying from 0.026 to 0.079 mm across geometries. This variation suggests an influence of local thermal conditions and contour–hatch interaction, although the present data cannot distinguish between these mechanisms. Border count was dimensionally inactive but showed a potential influence on surface quality, indicating that border parameters cannot be selected solely on dimensional or build-time considerations.

Overall, the results show that contour optimisation can effectively control dimensional offset, but its influence on surface quality is strongly dependent on feature class and orientation. The observed surface trends provide useful process insight, but additional controlled confocal measurements are required to establish predictive roughness models and to separate the individual effects of power, speed, and energy density.

6.3 RQ3: Can response surface modelling identify contour process windows that satisfy dimensional accuracy requirements, and what surface-quality constraints apply within those windows?

Response surface models were fitted and validated, with R^2 values of 0.785–0.901 and no significant lack of fit ($p = 0.27$–0.88). The models were then used to determine the beam compensation required to achieve zero dimensional deviation for each feature class.

No single compensation value satisfies all feature classes. On the upper tie plate, walls require approximately 0.079 mm and bore inner diameters approximately 0.108 mm, while the external bore diameters remain undersized at every tested setting, by at least 0.196 mm. Using the wall optimum leaves bore inner diameters undersized by about 0.053 mm. Parts containing different feature classes therefore require feature-specific compensation, through per-body parameter assignment or CAD-side offsetting. The external bore diameters can only be corrected in CAD.

A further limitation is that contour parameters do not reduce dimensional variation. The model for wall-to-wall range gave a low R^2 of 0.097, with no significant parameter effects. This indicates that achievable tolerance is mainly limited by process variation rather than compensation accuracy, and cannot be improved through contour optimisation alone.
Within these windows, the available surface data suggest that compensation can be set for dimension without a measurable penalty in vertical-wall finish, based on a single controlled pair (Section 4.9.2). Finish is instead governed mainly by contour energy input, and possibly by the number of borders. The highest energy settings give the smoothest walls but coincide with the bore-closure limit for 0.5 mm openings (Section 4.8).

6.4 Principal contributions

- Demonstration, on a graded 0.5–1.5 mm wall series, that the dimensional error in this process window is a constant offset rather than a scaling error, and that percentage-based reporting of AM dimensional accuracy can generate an apparent size dependence with no physical content.

- Quantification of the opposite compensation response of internal and external features, with slopes matching the geometric expectation, established on a coupon carrying both classes under identical parameters.
- Identification and quantification of the resulting conflict: no single global compensation value can null both classes, with the cost of each choice stated in millimetres.
- Confirmation of the internal/external division by an independent measurement modality, with internal surfaces being rougher than external surfaces on every areal parameter in every coupon measured.

6.5 Validity envelope

All quantitative results reported in this thesis apply to 316L stainless steel processed on an SLM 280 system under argon, at 60 µm layer thickness and the hatch condition used in Print 2, and within tested ranges of 130–170 W contour laser power, 200–500 mm/s contour scan speed, 0.04–0.10 mm beam compensation and one or two border passes. The bore-ID compensation value of 0.108 mm lies just beyond that range, and the external bore diameters have no zero crossing within it. The first requires confirmation coupons, and the second a validated CAD allowance, before adoption.

7

Future Work

The work reported here identifies several clearly defined directions for further study. These are prioritised according to their expected contribution and ease of execution, taking into account the work already completed. The first three can be completed using existing specimens and would serve as a continuation of the project, with this study as a foundation.

7.1 Extending the current analysis

These items require no new build. The Print 2 coupons still exist, and each closes a gap identified in Section 5.9.

Break the confounding in the existing confocal subsets. The five thin-wall coupons measured lie on a single power-speed diagonal and the five upper tie plate coupons on a single power-compensation diagonal, which is why Equation 5.1 cannot isolate energy density. Two further thin-wall coupons, one at 130 W / 200 mm/s and one at 170 W / 500 mm/s, would break that diagonal and separate energy density from power and speed individually. These are the two most informative measurements available on existing specimens.

Extend confocal coverage to make roughness modellable. Measuring 12–15 of the existing 26 upper tie plate coupons, chosen to span the factor space, would convert the surface data from a paired comparison into a modellable response and allow the surface-quality component of the second research question to be answered. Extending the same treatment to the thin-wall coupons would test whether the contour-roughness relationship is geometry dependent in the way the dimensional response is.

Establish a confocal repeatability estimate. No repeat measurements were made on the vertical-wall surfaces, so measurement scatter cannot currently be separated from process scatter. Coupons UT_18 and UT_21 differ only in border count and differ in S_a by 2.16 µm, which is most of the range across the five coupons; whether that is a border-count effect or measurement noise cannot be resolved without repeats. Re-measuring one surface three times and measuring the two thin-wall replicate pairs would settle it and would also test the border-count observation of

Section 5.5.

7.2 Confirmation builds

Verify the compensation values at the range edges. The bore-ID optimum of 0.108 mm lies just beyond the tested range. A short confirmation build at 0.11, 0.12 and 0.13 mm would close this case. The external bore diameters cannot be corrected through compensation within the tested range. Their correction should instead be validated as a CAD-side allowance of approximately the best-case residual (about 0.2 mm on diameter), checked on a confirmation coupon.

Validate the recommended settings on the full component. The compensation values derived here were established on unit-cell coupons. A build of full-scale upper tie plate or filter plate geometry using per-body compensation (external features at approximately 0.080 mm, internal features at approximately 0.110 mm) would test whether the coupon-derived rules transfer to the complete component, which is the necessary step before any industrial adoption.

7.3 Extending the parameter space

Re-test laser power over an energy-density-matched range. The power null result most likely reflects a range that was too narrow relative to the speed range. Repeating the design with a power range spanning a comparable factor in linear energy density, for example 100–250 W, would establish whether power genuinely has no effect on contour placement or whether it was simply under-ranged here.

Investigate contour–hatch interaction. Hatch parameters were deliberately held constant to isolate border effects. Zhang and Yuan [10] show that the transition zone between contour and hatch is governed by the contour offset and the relative energy densities of the two exposures, and the residual geometry dependence observed in Section 5.4 may be partly a contour–hatch effect. A follow-on design varying contour–hatch overlap alongside beam compensation would address this directly.

7.4 Addressing process uniformity

The finding that wall-to-wall uniformity is not controllable by contour parameters identifies the next bottleneck but does not diagnose it. A dedicated study would vary the factors that were held constant or unrecorded here: position on the build plate relative to the rear-to-front gas flow, recoater condition and blade wear, powder reuse cycle, and layer-to-layer variation in delivered layer thickness. Because these are build-level rather than part-level variables, such a study requires a purpose-designed plate layout with replicate coupons distributed systematically across it, rather than the geometry-grouped zoning used here.

This work would establish the achievable tolerance band for the process, which is what an industrial specification actually requires and which contour optimisation alone cannot provide.

7.5 Beyond dimensional and surface characterisation

The following extend the scope of the investigation and are planned to be conducted in the later stages of the project.

- **Metallurgical characterisation of the contour-defined zone.** Cross-sectional metallography of the border region under different contour parameters would test whether the compensation settings recommended on dimensional grounds also produce acceptable density and microstructure at the part surface, where fatigue cracks initiate.
- **Verification of the adhered-particle mechanism.** The interpretation offered in Section 5.2 for why internal surfaces are rougher, namely adhered partially melted powder that is neither recoated nor re-melted, is consistent with the data but not demonstrated. Cross-sectional imaging or X-ray computed tomography of bore surfaces would test it directly.
- **Residual stress and distortion.** Not investigated here. Relevant particularly to thin-wall components and to the question of whether the constant offset changes after stress relief.
- **Mechanical property evaluation.** Whether contour parameter selection, which governs the surface condition, measurably affects fatigue performance is an open and industrially important question.
- **In-situ monitoring and adaptive control.** Melt pool monitoring on contour tracks would allow the contour condition to be verified during the build rather than inferred from post-build measurement, and in principle would permit compensation to be adapted per feature in real time.
- **Data-driven modelling.** With a sufficiently large dataset spanning geometries, machine learning approaches could extend the response surface models to predict deviation for arbitrary feature geometry. This should follow rather than precede a properly resolved physical understanding, and the present dataset is not yet large enough to support it.

Bibliography

[1] ALLEA (2023). *The European Code of Conduct for Research Integrity: Revised Edition 2023*. Berlin. DOI: 10.26356/ECOC.

[2] DebRoy, T., Wei, H. L., Zuback, J. S., Mukherjee, T., Elmer, J. W., Milewski, J. O., Beese, A. M., Wilson-Heid, A., De, A., & Zhang, W. (2018). Additive manufacturing of metallic components – Process, structure and properties. *Progress in Materials Science*, 92, 112–224. DOI: 10.1016/j.pmatsci.2017.10.001.

[3] Herzog, D., Seyda, V., Wycisk, E., & Emmelmann, C. (2016). Additive manufacturing of metals. *Acta Materialia*, 117, 371–392. DOI: 10.1016/j.actamat.2016.07.019.

[4] King, W. E., Anderson, A. T., Ferencz, R. M., Hodge, N. E., Kamath, C., Khairallah, S. A., & Rubenchik, A. M. (2015). Laser powder bed fusion additive manufacturing of metals; physics, computational, and materials challenges. *Applied Physics Reviews*, 2(4), 041304. DOI: 10.1063/1.4937809.

[5] Khairallah, S. A., Anderson, A. T., Rubenchik, A., & King, W. E. (2016). Laser powder-bed fusion additive manufacturing: Physics of complex melt flow and formation mechanisms of pores, spatter, and denudation zones. *Acta Materialia*, 108, 36–45. DOI: 10.1016/j.actamat.2016.02.014.

[6] Li, R., Liu, J., Shi, Y., Wang, L., & Jiang, W. (2012). Balling behavior of stainless steel and nickel powder during selective laser melting process. *International Journal of Advanced Manufacturing Technology*, 59(9–12), 1025–1035. DOI: 10.1007/s00170-011-3566-1.

[7] Mercelis, P., & Kruth, J. P. (2006). Residual stresses in selective laser sintering and selective laser melting. *Rapid Prototyping Journal*, 12(5), 254–265. DOI: 10.1108/13552540610707013.

[8] Gibson, I., Rosen, D., Stucker, B., & Khorasani, M. (2021). *Additive Manufacturing Technologies* (3rd ed.). Springer.

[9] Brandt, M. (Ed.) (2017). *Laser Additive Manufacturing: Materials, Design, Technologies, and Applications*. Woodhead Publishing. DOI: 10.1016/C2014-0-03891-9.

[10] Zhang, T., & Yuan, L. (2024). Interaction of contour and hatch parameters on vertical surface roughness in laser powder bed fusion. *Journal of Materials Research and Technology*, 32, 3390–3401. DOI: 10.1016/j.jmrt.2024.08.170.

[11] Zhang, T., & Yuan, L. (2022). Understanding surface roughness on vertical surfaces of 316L stainless steel in laser powder bed fusion additive manufacturing. *Powder Technology*, 411, 117957. DOI: 10.1016/j.powtec.2022.117957.

[12] Zhang, T., & Yuan, L. (2025). Dimensional accuracy and surface roughness of thin-wall geometries in laser powder bed fusion of 316L stainless

steel. *Engineering Science in Additive Manufacturing*, 1(3), 025340022. DOI: 10.36922/ESAM025340022.

[13] Patel, S., Rogalsky, A., & Vlasea, M. (2020). Towards understanding side-skin surface characteristics in laser powder bed fusion. *Journal of Materials Research*, 35(15), 2055–2064. DOI: 10.1557/jmr.2020.125.

[14] Glaubitz, E. B., Fox, J. C., Kafka, O. L., & Gockel, J. (2025). Contour parameters, melt pool behavior, and surface roughness relationships across laser powder bed fusion platforms and metallic alloys. *International Journal of Advanced Manufacturing Technology*, 136(10), 4419–4437. DOI: 10.1007/s00170-025-15066-0.

[15] Habeeb, N. V. V., & Chou, K. (2025). Surface roughness and image analyses of contour scanning offset effects on sloping topography in laser powder bed fusion. *International Journal of Advanced Manufacturing Technology*, 138(7), 3575–3591. DOI: 10.1007/s00170-025-15745-y.

[16] Habeeb, N. V. V., & Chou, K. (2026). Effect of inclined angles and contouring parameters on upskin surface characteristics of parts made by laser powder-bed fusion. *Coatings*, 16(1), 119. DOI: 10.3390/coatings16010119.

[17] Yasa, E., Deckers, J., & Kruth, J. P. (2011). The investigation of the influence of laser re-melting on density, surface quality and microstructure of selective laser melting parts. *Rapid Prototyping Journal*, 17(5), 312–327. DOI: 10.1108/13552541111156450.

[18] Strano, G., Hao, L., Everson, R. M., & Evans, K. E. (2013). Surface roughness analysis, modelling and prediction in selective laser melting. *Journal of Materials Processing Technology*, 213(4), 589–597. DOI: 10.1016/j.jmatprotec.2012.11.011.

[19] Boschetto, A., Bottini, L., & Veniali, F. (2017). Roughness modeling of AlSi10Mg parts fabricated by selective laser melting. *Journal of Materials Processing Technology*, 241, 154–163. DOI: 10.1016/j.jmatprotec.2016.11.013.

[20] Townsend, A., Senin, N., Blunt, L., Leach, R. K., & Taylor, J. S. (2016). Surface texture metrology for metal additive manufacturing: a review. *Precision Engineering*, 46, 34–47. DOI: 10.1016/j.precisioneng.2016.06.001.

[21] Thompson, A., Newton, L., & Leach, R. (2023). New standard for metal powder bed fusion surface texture measurement and characterisation. *Metrology*, 3(2), 237–245. DOI: 10.3390/metrology3020013.

[22] Fox, J., Moylan, S. P., & Lane, B. (2016). Effect of process parameters on the surface roughness of overhanging structures in laser powder bed fusion additive manufacturing. *Procedia CIRP*, 45, 131–134. DOI: 10.1016/j.procir.2016.02.347.

[23] Leach, R. K. (2011). *Optical Measurement of Surface Topography*. Springer.

[24] Vu, H. M., Meiniger, S., Ringel, B., Hoche, H., Oechsner, M., Weigold, M., & Seidel, C. (2024). Investigation on surface characteristics of wall structures out of stainless steel 316L manufactured by laser powder bed fusion. *Progress in Additive Manufacturing*, 9(6), 2041–2060. DOI: 10.1007/s40964-023-00559-9.

[25] Maleki, E., Salehnasab, B., Paul, M., Shao, S., & Shamsaei, N. (2025). Dimensional accuracy of fabricated geometries through powder bed fusion: An overview and a new benchmark artifact proposal. *Materials & Design*, 257, 114361. DOI: 10.1016/j.matdes.2025.114361.

[26] Gradl, P., Tinker, D. C., Ivester, J., Skinner, S. W., Teasley, T., & Bili, J. L. (2021). Geometric feature reproducibility for laser powder bed fusion (L-PBF) additive manufacturing with Inconel 718. *Additive Manufacturing*, 47, 102305. DOI: 10.1016/j.addma.2021.102305.

[27] Wu, Z., Narra, S. P., & Rollett, A. (2020). Exploring the fabrication limits of thin-wall structures in a laser powder bed fusion process. *International Journal of Advanced Manufacturing Technology*, 110(1–2), 191–207. DOI: 10.1007/s00170-020-05827-4.

[28] López-García, C., García-López, E., Siller, H. R., Sandoval-Robles, J. A., & Rodriguez, C. A. (2022). A dimensional assessment of small features and lattice structures manufactured by laser powder bed fusion. *Progress in Additive Manufacturing*, 7(4), 751–763. DOI: 10.1007/s40964-022-00263-0.

[29] Gaikwad, A., Imani, F., Rao, P., Yang, H., & Reutzel, E. (2019). Design rules and in-situ quality monitoring of thin-wall features made using laser powder bed fusion. In *Proceedings of the ASME 2019 14th International Manufacturing Science and Engineering Conference (MSEC)*, Vol. 1, V001T01A039. DOI: 10.1115/MSEC2019-3035.

[30] Sun, Z., Tan, X., Tor, S. B., & Yeong, W. Y. (2016). Selective laser melting of stainless steel 316L with low porosity and high build rates. *Materials & Design*, 104, 197–204. DOI: 10.1016/j.matdes.2016.05.035.

[31] Cherry, J. A., Davies, H. M., Mehmood, S., Lavery, N. P., Brown, S. G. R., & Sienz, J. (2015). Investigation into the effect of process parameters on microstructural and physical properties of 316L stainless steel parts by selective laser melting. *International Journal of Advanced Manufacturing Technology*, 76(5–8), 869–879. DOI: 10.1007/s00170-014-6297-2.

[32] Ahmed, N., Barsoum, I., Haidemenopoulos, G., & Abu Al-Rub, R. K. (2022). Process parameter selection and optimization of laser powder bed fusion for 316L stainless steel: A review. *Journal of Manufacturing Processes*, 75, 415–434. DOI: 10.1016/j.jmapro.2021.12.064.

[33] Zhang, Z., Zhang, T., Sun, C., Karna, S., & Yuan, L. (2024). Understanding melt pool behavior of 316L stainless steel in laser powder bed fusion additive manufacturing. *Micromachines*, 15(2), 170. DOI: 10.3390/mi15020170.

[34] Leicht, A., Klement, U., & Hryha, E. (2018). Effect of build geometry on the microstructural development of 316L parts produced by additive manufacturing. *Materials Characterization*, 143, 137–143. DOI: 10.1016/j.matchar.2018.04.040.

[35] Wróbel, R., Del Guidice, L., Scheel, P., Abando, N., Maeder, X., Vassiliou, M., Hosseini, E., Spolenak, R., & Leinenbach, C. (2024). Influence of wall thickness on microstructure and mechanical properties of thin-walled 316L stainless steel produced by laser powder bed fusion. *Materials & Design*, 238, 112652. DOI: 10.1016/j.matdes.2024.112652.

[36] Tang, M., Pistorius, P. C., & Beuth, J. L. (2017). Prediction of lack-of-fusion porosity for powder bed fusion. *Additive Manufacturing*, 14, 39–48. DOI: 10.1016/j.addma.2016.12.001.

[37] Thomas, D. (2009). *The development of design rules for selective laser melting.* PhD thesis, University of Wales Institute, Cardiff (now Cardiff Metropolitan University).

[38] Montgomery, D. C. (2017). *Design and Analysis of Experiments* (9th ed.). John Wiley & Sons.

[39] Box, G. E. P., & Wilson, K. B. (1951). On the experimental attainment of optimum conditions. *Journal of the Royal Statistical Society, Series B*, 13(1), 1–45.

[40] Read, N., Wang, W., Essa, K., & Attallah, M. M. (2015). Selective laser melting of AlSi10Mg alloy: Process optimisation and mechanical properties development. *Materials & Design*, 65, 417–424. DOI: 10.1016/j.matdes.2014.09.044.

[41] Gajera, H. M., Dave, K. G., & Jani, V. P. (2019). Experimental investigation and analysis of dimensional accuracy of laser-based powder bed fusion made specimen by application of response surface methodology. *Progress in Additive Manufacturing*, 4(4), 371–382. DOI: 10.1007/s40964-019-00076-8.

[42] ISO (2021). *ISO 25178-2:2021 Geometrical product specifications (GPS) – Surface texture: Areal – Part 2: Terms, definitions and surface texture parameters* (2nd ed.). International Organization for Standardization, Geneva.

[43] ISO (2019). *ISO 25178-600:2019 Geometrical product specifications (GPS) – Surface texture: Areal – Part 600: Metrological characteristics for areal topography measuring methods.* International Organization for Standardization, Geneva.

[44] ISO/ASTM (2021). *ISO/ASTM 52900:2021 Additive manufacturing – General principles – Fundamentals and vocabulary.* International Organization for Standardization, Geneva.

[45] ISO/ASTM (2023). *ISO/ASTM 52902:2023 Additive manufacturing – Test artefacts – Geometric capability assessment of additive manufacturing systems.* International Organization for Standardization, Geneva.

[46] ISO/ASTM (2019). *ISO/ASTM 52911-1:2019 Additive manufacturing – Design – Part 1: Laser-based powder bed fusion of metals.* International Organization for Standardization, Geneva.

[47] World Nuclear News (2022). 3D-printed fuel component installed at Swedish reactor. *World Nuclear News*, 21 September 2022. Available at: `https://www.world-nuclear-news.org/Articles/3D-printed-fuel-component-installed-at-Swedish-rea`

[48] Framatome (2022). *Framatome installs first 3D-printed stainless steel fuel component at Forsmark Nuclear Power Plant.* Press release, September 2022.

[49] Additive Manufacturing Media (2025). 3D printed spacer grids for nuclear power: The Cool Parts Show #79. 9 January 2025. Available at: `https://www.additivemanufacturing.media/articles/3d-printed-spacer-grids-for-nuclear-power-the-cool-parts-show-79`

A

Baseline characterisation data

A.1 Baseline characterisation

A.1.1 Geometries characterised

Among the studied baseline prints, four families of test geometries provided the most meaningful insights into different aspects of PBF-LB geometric quality relevant to the requirements of the target application:

Thin walls. Six vertical walls with nominal thicknesses of 0.5, 0.7, 0.9, 1.1, 1.3 and 1.5 mm, identical to those used in the subsequent DoE. These are the most direct probe of border parameter effects, as the entire wall cross-section at the thinnest nominal is defined by the contour scan.

Grooves. Three groove types cut into a solid block: a narrow rectangular groove (0.5 mm width), a wider rectangular groove (1 mm width), and a trapezoidal groove with inclined walls (2 mm top width tapering to 0.5 mm). These features test internal dimensional accuracy and corner fidelity.

Square lattices. Lattice structures with two unit-cell sizes: a large cell with 2 mm edge length and a small cell with 1 mm edge length. Four features were characterised per cell: outer edge length, unit-cell angle (squareness), strut thickness, and pore edge length.

Angled overhangs. Struts oriented at 45° and 70° from the horizontal, used to evaluate down-skin and up-skin surface quality as a function of overhang angle. Measurements were taken at three locations per strut to assess spatial variation.

A.1.2 Dimensional accuracy findings

Thin walls. Both workflows produced walls that were consistently undersized relative to the CAD nominal. The precision workflow used a beam compensation of 0.08 mm and the productivity workflow 0.07 mm. Most wall thicknesses showed high dimensional fidelity, but the thinnest walls (0.5 mm) exhibited the largest relative error. The precision workflow showed higher absolute deviation at the smallest thickness, consistent with its larger beam compensation removing more material

from the contour path.

Grooves. Internal groove widths were consistently larger than the CAD nominal in both workflows, the opposite direction to the thin-wall (external feature) deviation. The narrow 0.5 mm rectangular groove showed the largest dimensional error, confirming that small features are more sensitive to melt pool effects. The precision parameter set produced greater width deviation than the productivity set for most groove features. The trapezoidal groove exhibited mixed behaviour: the 2 mm top width was undersized in the productivity workflow but oversized in the precision workflow, while the internal corner radii increased from the CAD value of 0.5 mm to approximately 0.73–0.76 mm in both workflows due to melt pool spreading. Length dimensions along the scan direction were significantly more stable than width dimensions controlled by the contour scan, confirming that border-controlled features are the primary source of geometric deviation.

Lattices. Strut thickness was the dominant source of deviation, with relative errors of 30–40% for the thinnest struts. Pore sizes showed moderate but inconsistent deviation, particularly in the small-cell lattice. Outer dimensions and unit-cell angles were stable and reliable in both workflows. The precision workflow showed lower overall deviation and better geometric fidelity than the productivity workflow. Small lattices exhibited higher deviation than large lattices due to increased sensitivity to melt pool size effects.

A.1.3 Surface quality findings

Confocal microscopy measurements were performed on the thin-wall side-skin surfaces and on the overhang up-skin and down-skin surfaces. Table A.1 presents the thin-wall surface roughness data.

Table A.1: Baseline thin-wall surface roughness (mean values from stitched confocal measurements).

Thickness (mm)	Workflow	S_a (µm)	S_z (µm)	S_{10z} (µm)	S_{sk}
0.5	Precision	13.19	133.30	117.40	1.01
0.7	Precision	11.01	119.10	105.34	1.12
0.9	Precision	9.39	107.95	97.05	1.00
1.1	Precision	10.93	116.65	99.35	0.77
1.3	Precision	10.08	113.65	104.00	1.09
1.5	Precision	9.40	114.55	101.60	0.85
0.5	Productivity	9.90	146.25	124.75	0.27
0.7	Productivity	11.11	165.80	143.75	0.46
0.9	Productivity	10.05	138.60	98.91	0.54
1.1	Productivity	10.26	137.50	113.21	0.74
1.3	Productivity	11.05	159.30	116.25	0.32
1.5	Productivity	10.99	143.00	127.00	0.30

The arithmetic mean roughness (S_a) was comparable between the two workflows, ranging from 9.39 to 13.19 µm for precision and 9.90 to 11.11 µm for productivity.

However, the extreme roughness metrics (S_z and S_{10z}) were consistently higher for the productivity workflow. At 0.7 mm wall thickness, the productivity S_{10z} reached 143.75 µm compared to 105.34 µm for precision, a difference of 36%. This indicates that while the average surface texture is similar, the productivity workflow produces more pronounced extreme surface features, such as partially melted powder particles, balling defects and unstable melt pool edges, which increase peak-to-valley height.

Surface skewness (S_{sk}) revealed a systematic difference between workflows. The precision workflow produced consistently positive skewness values (0.77–1.12), indicating peak-dominated surfaces characteristic of partially melted powder adhesion. The productivity workflow showed lower positive skewness (0.27–0.74), suggesting more randomised surface morphology with smoother transitions between peaks and valleys.

Overhang surface roughness. At a 45° overhang angle, the down-skin S_a was 3–5 times higher than the up-skin S_a in both parameter sets, reflecting the critical thermal regime where partial self-support and unstable melt pool behaviour promote powder adhesion and dross formation. At 70°, the down-skin roughness improved substantially: S_a dropped from approximately 35–48 µm at 45° to 10–21 µm at 70°, because the steeper angle provides better heat conduction into solid material. The productivity parameters were especially problematic for low-angle overhangs, producing higher absolute roughness than the precision parameters at 45°. Location-to-location variation was observed, most visibly in the down-skin S_z and S_{10z} at 45°, likely caused by gas flow heterogeneity, local thermal history, and recoater powder interactions; however, these location effects were secondary to the dominant influence of overhang angle and parameter set.

B

DoE measurement data and fitted models

This appendix reproduces the as-measured data underlying Chapter 4 together with a summary of every response-surface model fitted. Deviations are not tabulated, as they follow directly from the measured and nominal values given here. Factor columns are the contour (border) exposure settings applied to the run: P_c laser power (W), v_c scan speed (mm/s), δ beam compensation (mm) and n_b number of border passes. All dimensions are in millimetres.

B.1 Fitted model summary

Table B.1 lists every dimensional response-surface model fitted in JMP. Models were reduced stepwise by removing the term with the highest p-value above 0.10, preserving model hierarchy; terms were judged significant at $\alpha = 0.05$. Lack-of-fit probabilities are computed against the pure error from the centre-point replicates of the respective design. The cube benchmark responses are included for completeness: no term reached significance for any of them (Section B.2.1).

Table B.1: Summary of fitted dimensional models.

Response	Geometry	Class	Terms retained	BC slope	R^2	R^2_{adj}	RMSE	n	LoF p
Bore inner diameter	UT	Internal	δ, v_c	1.823	0.892	0.883	0.0182	26	0.3286
Bore MD/OD	UT	External	δ, v_c, v_c^2, δ^2	−2.093	0.914	0.898	0.0191	26	0.6795
Wall thickness	UT	External	δ, v_c	−2.085	0.778	0.758	0.0306	26	0.6735
Wall thickness	TW	External	δ, v_c	−1.920	0.967	0.963	0.0117	21	0.9027
Wall thickness	C_TW	External	δ	−2.007	0.875	0.861	0.0215	11	0.2738
Wall thickness	SQ_F	External	δ, v_c, $v_c{\times}\delta$	−1.720	0.720	0.682	0.0303	26	0.3508
Pore width	SQ_F	Internal	δ, v_c, v_c^2	1.780	0.944	0.936	0.0121	26	0.6024
Outer diameter	CY	External	δ, v_c	−1.750	0.976	0.970	0.0092	11	0.8698
Inner diameter	CY	Internal	δ	1.408	0.495	0.439	0.0402	11	0.0531
Step faces	CB	External	none significant	–	–	–	–	11	–
Holes	CB	Internal	none significant	–	–	–	–	11	–
Fillets	CB	External	none significant	–	–	–	–	11	–

BC slope is the fitted coefficient on beam compensation, in mm of signed deviation per mm of applied compensation. RMSE and BC slope are in mm.

B.2 Measurement data from the DoE print

B.2.1 Cube benchmark: absence of contour response

All four feature classes were fitted against the three contour factors. No model reached significance for the step faces, holes or fillets; the notches showed a single beam-compensation term, discussed below. The step faces gave a mean signed deviation of $-0.018\,\text{mm}$ (SD $0.026\,\text{mm}$, model $p = 0.28$) and the lowest relative deviation of any feature in the study at 1.4%. The holes showed a fixed undersize of $-0.162\,\text{mm}$ (SD $0.060\,\text{mm}$, model $p = 0.33$), independent of both hole diameter and every parameter setting. The external fillets gave a mean absolute deviation of $0.220\,\text{mm}$ (5.9%) with no significant term. The notches gave a mean absolute deviation of $0.029\,\text{mm}$ (1.9%); beam compensation reached $p = 0.026$ with a slope of -0.80, well below the geometric expectation of -2, and this model is therefore reported but not relied upon.
The interpretation is given in Chapter 5: these features are embedded within a bulk volume, where the contour forms a negligible fraction of each cross-section and the hatch exposure governs the resulting dimension.

B.2.2 Upper tie plate (UT)

Table B.2: Upper tie plate: factor settings and measured bore diameters (mm).

Run	P_c	v_c	δ	n_b	A_ID	A_MD	A_OD	B_ID	B_OD	C_ID	C_OD	D_ID	D_MD	D_OD
UT_1	170	200	0.10	2	4.664	5.671	7.223	5.970	9.654	4.004	4.845	4.653	5.645	7.192
UT_2	150	350	0.10	2	4.665	5.776	7.219	5.929	9.592	3.967	4.798	4.629	5.718	7.072
UT_3	150	350	0.04	2	4.545	5.838	7.250	5.913	9.778	3.927	4.846	4.551	5.738	7.327
UT_4	170	500	0.04	1	4.550	5.964	7.347	5.913	9.803	3.877	4.885	4.562	5.815	7.166
UT_5	170	500	0.10	1	4.719	5.702	7.311	5.995	9.697	3.981	4.773	4.741	5.734	7.178
UT_6	130	500	0.04	1	4.599	5.847	7.330	5.914	9.784	3.932	4.811	4.570	5.787	7.300
UT_7	170	500	0.04	2	4.623	5.810	7.317	5.883	9.832	3.931	4.926	4.584	5.874	7.289
UT_8	150	350	0.07	2	4.672	5.803	7.344	5.945	9.763	3.986	4.764	4.602	5.768	7.218
UT_9	150	350	0.07	2	4.642	5.785	7.268	5.905	9.678	3.931	4.827	4.529	5.741	7.185
UT_10	130	200	0.10	1	4.655	5.786	7.252	5.973	9.669	3.948	4.750	4.635	5.848	7.194
UT_11	130	500	0.10	1	4.720	5.757	7.127	5.992	9.640	4.009	4.741	4.731	5.680	7.153
UT_12	170	200	0.04	1	4.552	5.913	7.404	5.828	9.830	3.778	4.905	4.525	5.815	7.417
UT_13	130	200	0.04	2	4.553	5.853	7.394	5.874	9.714	3.845	4.861	4.582	5.839	7.371
UT_14	150	200	0.07	1	4.664	5.856	7.416	5.865	9.787	3.947	4.865	4.562	5.791	7.321
UT_15	130	200	0.04	1	4.585	5.993	7.352	5.795	9.783	3.866	4.909	4.544	5.894	7.257
UT_16	170	200	0.10	1	4.706	5.740	7.192	5.904	9.738	3.989	4.773	4.699	5.721	7.175
UT_17	130	500	0.04	2	4.601	5.851	7.368	5.921	9.753	3.970	4.968	4.566	5.859	7.356
UT_18	150	350	0.07	2	4.655	5.754	7.292	5.917	9.740	3.955	4.848	4.647	5.823	7.131
UT_19	130	200	0.10	2	4.650	5.720	7.201	6.004	9.686	4.028	4.721	4.569	5.895	7.236
UT_20	130	350	0.07	1	4.685	5.802	7.258	5.944	9.708	3.990	4.861	4.646	5.850	7.307
UT_21	150	350	0.07	1	4.605	5.885	7.372	5.945	9.701	3.915	4.804	4.639	5.717	7.204
UT_22	170	200	0.04	2	4.631	5.905	7.427	5.826	9.780	3.842	4.842	4.545	5.843	7.410
UT_23	170	350	0.07	1	4.604	5.817	7.363	5.886	9.766	3.952	4.849	4.621	5.765	7.240
UT_24	130	500	0.10	2	4.726	5.787	7.268	6.018	9.678	4.005	4.759	4.677	5.636	7.170
UT_25	170	500	0.10	2	4.722	5.756	7.268	6.030	9.674	4.051	4.770	4.683	5.734	7.053
UT_26	150	500	0.07	1	4.662	5.861	7.377	5.910	9.798	3.926	4.793	4.620	5.845	7.333
Nominal	–	–	–	–	4.70	6.00	7.50	6.00	10.00	4.00	5.00	4.70	6.00	7.50

Table B.3: Upper tie plate: factor settings and measured wall thicknesses (mm).

Run	P_c	v_c	δ	n_b	AB	AC	BD	CD	BC
UT_1	170	200	0.10	2	0.435	0.459	0.445	0.423	0.457
UT_2	150	350	0.10	2	0.423	0.438	0.407	0.417	0.476
UT_3	150	350	0.04	2	0.525	0.556	0.525	0.564	0.502
UT_4	170	500	0.04	1	0.580	0.580	0.543	0.593	0.582
UT_5	170	500	0.10	1	0.403	0.400	0.369	0.394	0.384
UT_6	130	500	0.04	1	0.531	0.521	0.486	0.556	0.535
UT_7	170	500	0.04	2	0.648	0.556	0.529	0.529	0.546
UT_8	150	350	0.07	2	0.517	0.522	0.530	0.486	0.550
UT_9	150	350	0.07	2	0.550	0.527	0.528	0.568	0.461
UT_10	130	200	0.10	1	0.412	0.470	0.414	0.441	0.435
UT_11	130	500	0.10	1	0.419	0.407	0.403	0.418	0.468
UT_12	170	200	0.04	1	0.569	0.600	0.570	0.600	0.570
UT_13	130	200	0.04	2	0.678	0.542	0.521	0.591	0.614
UT_14	150	200	0.07	1	0.550	0.466	0.502	0.543	0.570
UT_15	130	200	0.04	1	0.583	0.580	0.612	0.579	0.609
UT_16	170	200	0.10	1	0.618	0.538	0.479	0.510	0.587
UT_17	130	500	0.04	2	0.582	0.601	0.599	0.587	0.653
UT_18	150	350	0.07	2	0.584	0.527	0.562	0.519	0.607
UT_19	130	200	0.10	2	0.441	0.495	0.482	0.480	0.495
UT_20	130	350	0.07	1	0.588	0.516	0.580	0.490	0.514
UT_21	150	350	0.07	1	0.537	0.497	0.511	0.473	0.510
UT_22	170	200	0.04	2	0.582	0.613	0.664	0.620	0.670
UT_23	170	350	0.07	1	0.587	0.534	0.506	0.513	0.524
UT_24	130	500	0.10	2	0.534	0.434	0.464	0.408	0.487
UT_25	170	500	0.10	2	0.480	0.440	0.452	0.407	0.499
UT_26	150	500	0.07	1	0.516	0.501	0.556	0.505	0.510
Nominal	–	–	–	–	0.50	0.50	0.50	0.50	0.50

B.2.3 Square grid filter (SQ_F)

Table B.4: Square grid filter: factor settings and measured pore and wall dimensions (mm).

Run	P_c	v_c	δ	Pore X1	Pore X2	Pore X3	Pore Y1	Pore Y2	Pore Y3	Wall X1	Wall X2	Wall X3	Wall Y1	Wall Y2	Wall Y3
SQ_F 1	170	200	0.10	2.047	2.032	2.053	2.041	2.112	2.023	0.490	0.500	0.432	0.452	0.480	0.472
SQ_F 2	150	350	0.10	2.105	2.093	2.114	2.093	2.119	2.093	0.456	0.445	0.411	0.410	0.439	0.417
SQ_F 3	150	350	0.04	2.007	1.992	2.000	1.937	2.017	1.987	0.627	0.598	0.627	0.571	0.635	0.508
SQ_F 4	170	500	0.04	1.967	1.967	2.029	1.966	1.966	1.967	0.534	0.553	0.549	0.540	0.541	0.513
SQ_F 5	170	500	0.10	2.113	2.075	2.083	2.150	2.119	2.111	0.462	0.545	0.461	0.417	0.417	0.414
SQ_F 6	130	500	0.04	1.914	1.991	1.992	1.993	1.976	1.987	0.566	0.524	0.629	0.592	0.573	0.560
SQ_F 7	170	500	0.04	1.980	2.017	2.047	1.964	2.004	1.964	0.517	0.499	0.518	0.504	0.504	0.525
SQ_F 8	150	350	0.07	2.068	2.034	2.051	2.051	2.023	1.994	0.439	0.484	0.456	0.472	0.440	0.461
SQ_F 9	150	350	0.07	2.055	2.108	2.053	2.023	2.051	1.995	0.457	0.456	0.412	0.399	0.412	0.417
SQ_F 10	130	200	0.10	2.108	2.098	2.080	2.055	2.052	2.052	0.420	0.419	0.439	0.478	0.439	0.481
SQ_F 11	130	500	0.10	2.034	2.096	2.097	2.067	2.126	2.093	0.532	0.508	0.471	0.439	0.465	0.465
SQ_F 12	170	200	0.04	1.971	1.929	1.992	1.991	1.991	1.991	0.625	0.584	0.593	0.616	0.530	0.649
SQ_F 13	130	200	0.04	1.940	1.977	1.959	1.976	1.929	1.884	0.547	0.538	0.538	0.513	0.547	0.530
SQ_F 14	150	200	0.07	1.938	1.995	2.051	2.014	1.967	2.049	0.485	0.483	0.496	0.530	0.545	0.492
SQ_F 15	130	200	0.04	1.938	2.004	1.966	2.023	1.985	1.938	0.598	0.570	0.598	0.546	0.523	0.584
SQ_F 16	170	200	0.10	2.083	2.032	2.127	2.063	2.064	2.095	0.456	0.422	0.457	0.425	0.465	0.465
SQ_F 17	130	500	0.04	1.990	1.886	1.996	2.034	1.994	1.968	0.531	0.490	0.471	0.491	0.482	0.515
SQ_F 18	150	350	0.07	2.013	2.034	2.034	2.039	2.080	2.051	0.459	0.417	0.417	0.491	0.463	0.464
SQ_F 19	130	200	0.10	2.051	2.108	2.051	2.127	2.103	2.069	0.444	0.427	0.414	0.417	0.388	0.365
SQ_F 20	130	350	0.07	2.051	2.042	2.034	2.083	2.007	2.060	0.527	0.502	0.527	0.517	0.541	0.477
SQ_F 21	150	350	0.07	2.080	2.080	2.080	2.023	2.023	2.023	0.513	0.513	0.486	0.449	0.587	0.465
SQ_F 22	170	200	0.04	1.938	2.016	1.929	1.987	2.023	1.970	0.608	0.545	0.549	0.525	0.617	0.556
SQ_F 23	170	350	0.07	1.996	2.053	2.034	2.013	2.064	2.053	0.496	0.474	0.509	0.528	0.556	0.500
SQ_F 24	130	500	0.10	2.150	2.128	2.109	2.000	2.100	2.080	0.530	0.499	0.496	0.452	0.398	0.434
SQ_F 25	170	500	0.10	2.053	2.009	2.103	2.154	2.100	2.009	0.432	0.509	0.448	0.451	0.437	0.427
SQ_F 26	150	500	0.07	2.075	2.076	2.034	2.069	2.028	2.028	0.540	0.463	0.473	0.461	0.502	0.445

B.2.4 Thin walls (TW)

Table B.5: Thin walls: factor settings and measured thicknesses (mm), walls A–C (nominal 0.5, 0.7, 0.9 mm).

Run	P_c	v_c	δ	n_b	Wall A1	Wall A2	Wall A3	Wall B1	Wall B2	Wall B3	Wall C1	Wall C2	Wall C3
TW 1	130	500	0.04	1	0.524	0.479	0.525	0.714	0.701	0.741	0.926	0.906	0.876
TW 2	170	500	0.04	2	0.463	0.533	0.510	0.694	0.671	0.625	0.856	0.903	0.856
TW 3	170	200	0.04	1	0.517	0.543	0.571	0.751	0.749	0.776	0.956	0.930	0.879
TW 4	170	500	0.10	1	0.348	0.370	0.371	0.579	0.579	0.602	0.764	0.787	0.811
TW 5	130	500	0.10	1	0.414	0.388	0.337	0.543	0.647	0.571	0.827	0.801	0.801
TW 6	170	200	0.10	2	0.388	0.388	0.388	0.594	0.569	0.621	0.827	0.801	0.827
TW 7	130	200	0.04	2	0.517	0.543	0.543	0.698	0.692	0.734	0.883	0.908	0.881
TW 8	170	200	0.10	1	0.413	0.439	0.492	0.594	0.647	0.621	0.827	0.827	0.827
TW 9	130	200	0.10	1	0.388	0.414	0.413	0.568	0.492	0.595	0.775	0.775	0.801
TW 10	130	200	0.10	2	0.417	0.417	0.394	0.650	0.625	0.556	0.834	0.810	0.788
TW 11	130	500	0.10	2	0.371	0.347	0.345	0.579	0.579	0.532	0.741	0.767	0.769
TW 12	130	200	0.04	1	0.532	0.533	0.509	0.741	0.741	0.764	0.880	0.880	0.927
TW 13	130	500	0.04	2	0.486	0.464	0.463	0.694	0.672	0.718	0.880	0.903	0.856
TW 14	170	500	0.10	2	0.363	0.336	0.388	0.517	0.595	0.580	0.751	0.724	0.789
TW 15	170	200	0.04	2	0.492	0.517	0.536	0.750	0.672	0.674	0.956	0.879	0.906
TW 16	170	500	0.04	1	0.492	0.465	0.465	0.672	0.672	0.646	0.879	0.904	0.930
TW 17	150	350	0.04	1	0.509	0.568	0.492	0.698	0.776	0.672	0.918	0.954	0.931
TW 18	150	350	0.10	1	0.399	0.370	0.342	0.570	0.627	0.598	0.800	0.770	0.798
TW 19	150	350	0.10	1	0.399	0.427	0.313	0.541	0.514	0.629	0.769	0.827	0.741
TW 20	150	350	0.04	1	0.571	0.484	0.399	0.627	0.743	0.713	0.913	0.883	0.912
TW 21	150	350	0.07	1	0.427	0.399	0.457	0.684	0.599	0.627	0.855	0.798	0.798
Nominal	–	–	–	–	0.5	0.5	0.5	0.7	0.7	0.7	0.9	0.9	0.9

Table B.6: Thin walls: factor settings and measured thicknesses (mm), walls D–F (nominal 1.1, 1.3, 1.5 mm).

Run	P_c	v_c	δ	n_b	Wall D1	Wall D2	Wall D3	Wall E1	Wall E2	Wall E3	Wall F1	Wall F2	Wall F3
TW 1	130	500	0.04	1	1.086	1.163	1.064	1.273	1.300	1.297	1.505	1.453	1.435
TW 2	170	500	0.04	2	1.088	1.089	1.088	1.296	1.301	1.300	1.470	1.478	1.470
TW 3	170	200	0.04	1	1.137	1.189	1.138	1.292	1.344	1.348	1.551	1.499	1.447
TW 4	170	500	0.10	1	0.972	0.949	0.926	1.135	1.230	1.157	1.343	1.391	1.343
TW 5	130	500	0.10	1	0.931	1.008	1.086	1.215	1.189	1.163	1.345	1.370	1.318
TW 6	170	200	0.10	2	0.982	0.982	1.009	1.189	1.294	1.189	1.370	1.447	1.397
TW 7	130	200	0.04	2	1.140	1.111	1.083	1.254	1.424	1.369	1.512	1.481	1.481
TW 8	170	200	0.10	1	1.034	0.959	0.983	1.241	1.241	1.189	1.421	1.396	1.421
TW 9	130	200	0.10	1	0.956	1.034	1.059	1.215	1.215	1.189	1.396	1.370	1.397
TW 10	130	200	0.10	2	1.042	1.020	1.042	1.188	1.132	1.225	1.453	1.453	1.396
TW 11	130	500	0.10	2	0.926	0.926	0.927	1.181	1.175	1.138	1.344	1.344	1.345
TW 12	130	200	0.04	1	1.134	1.158	1.111	1.297	1.389	1.296	1.528	1.505	1.505
TW 13	130	500	0.04	2	1.042	1.065	1.088	1.320	1.296	1.296	1.458	1.459	1.435
TW 14	170	500	0.10	2	0.982	0.982	1.006	1.163	1.215	1.163	1.370	1.370	1.370
TW 15	170	200	0.04	2	1.059	1.086	1.085	1.241	1.345	1.345	1.499	1.525	1.473
TW 16	170	500	0.04	1	1.060	1.060	1.111	1.266	1.292	1.292	1.525	1.525	1.474
TW 17	150	350	0.04	1	1.164	1.138	1.137	1.370	1.318	1.318	1.448	1.499	1.447
TW 18	150	350	0.10	1	0.998	0.969	0.969	1.197	1.140	1.225	1.396	1.397	1.453
TW 19	150	350	0.10	1	0.998	0.969	0.998	1.198	1.198	1.168	1.368	1.339	1.370
TW 20	150	350	0.04	1	1.083	1.113	1.083	1.339	1.254	1.254	1.510	1.481	1.510
TW 21	150	350	0.07	1	1.083	1.055	1.084	1.282	1.225	1.255	1.424	1.396	1.396
Nominal	–	–	–	–	1.1	1.1	1.1	1.3	1.3	1.3	1.5	1.5	1.5

B.2.5 Cross walls (C_TW)

Table B.7: Cross walls: factor settings and measured thicknesses (mm), nominal 0.5, 0.7, 0.9 mm. Four measurements per wall.

Run	P_c	v_c	δ	0.5/M1	0.5/M2	0.5/M3	0.5/M4	0.7/M1	0.7/M2	0.7/M3	0.7/M4	0.9/M1	0.9/M2	0.9/M3	0.9/M4
C_TW_S1	170	200	0.04	0.582	0.578	0.605	0.578	0.784	0.752	0.752	0.752	0.906	0.939	0.986	0.970
C_TW_S2	150	350	0.07	0.478	0.460	0.430	0.489	0.671	0.671	0.650	0.671	0.860	0.881	0.840	0.861
C_TW_S3	150	350	0.07	0.439	0.470	0.488	0.470	0.673	0.641	0.663	0.769	0.833	0.834	0.851	0.869
C_TW_S4	130	500	0.10	0.392	0.378	0.394	0.370	0.644	0.644	0.591	0.634	0.794	0.786	0.768	0.786
C_TW_S5	170	500	0.04	0.479	0.487	0.537	0.494	0.715	0.729	0.671	0.709	0.844	0.996	0.883	0.881
C_TW_S6	170	500	0.10	0.449	0.451	0.431	0.468	0.583	0.637	0.582	0.609	0.771	0.768	0.741	0.794
C_TW_S7	170	200	0.10	0.449	0.461	0.393	0.407	0.654	0.621	0.619	0.621	0.812	0.834	0.833	0.791
C_TW_S8	130	200	0.04	0.487	0.552	0.569	0.485	0.662	0.662	0.689	0.711	0.899	0.963	0.922	0.899
C_TW_S9	150	350	0.07	0.403	0.454	0.465	0.407	0.562	0.595	0.585	0.637	0.998	0.898	0.856	0.834
C_TW_S10	130	500	0.04	0.566	0.562	0.551	0.522	0.667	0.761	0.711	0.763	1.006	1.017	0.906	0.903
C_TW_S11	130	200	0.10	0.411	0.469	0.408	0.453	0.622	0.687	0.621	0.662	0.847	0.847	0.821	0.814

Table B.8: Cross walls: factor settings and measured thicknesses (mm), nominal 1.1, 1.3, 1.5 mm. Four measurements per wall.

Run	P_c	v_c	δ	1.1/M1	1.1/M2	1.1/M3	1.1/M4	1.3/M1	1.3/M2	1.3/M3	1.3/M4	1.5/M1	1.5/M2	1.5/M3	1.5/M4
C_TW_S1	170	200	0.04	1.116	1.170	1.151	1.245	1.310	1.310	1.360	1.335	1.482	1.540	1.543	1.538
C_TW_S2	150	350	0.07	1.037	1.058	1.023	1.054	1.316	1.284	1.224	1.243	1.370	1.421	1.447	1.423
C_TW_S3	150	350	0.07	1.085	1.053	1.103	1.048	1.226	1.244	1.220	1.274	1.398	1.408	1.407	1.445
C_TW_S4	130	500	0.10	0.971	1.026	1.005	1.020	1.182	1.154	1.105	1.070	1.308	1.373	1.438	1.509
C_TW_S5	170	500	0.04	1.066	1.086	1.050	1.108	1.300	1.315	1.270	1.331	1.496	1.476	1.453	1.474
C_TW_S6	170	500	0.10	0.963	0.949	0.962	0.936	1.179	1.179	1.180	1.179	1.376	1.406	1.299	1.349
C_TW_S7	170	200	0.10	0.971	0.996	1.040	0.996	1.160	1.329	1.160	1.240	1.369	1.410	1.369	1.282
C_TW_S8	130	200	0.04	1.110	1.156	1.113	1.086	1.277	1.364	1.376	1.294	1.471	1.457	1.534	1.471
C_TW_S9	150	350	0.07	1.020	1.003	1.054	0.996	1.233	1.216	1.200	1.211	1.419	1.420	1.442	1.404
C_TW_S10	130	500	0.04	1.096	1.120	1.055	1.137	1.347	1.272	1.294	1.366	1.551	1.608	1.491	1.551
C_TW_S11	130	200	0.10	0.926	1.101	1.043	0.972	1.220	1.241	1.179	1.220	1.404	1.404	1.404	1.435

B.2.6 Cube benchmark (CB)

Table B.9: Cube benchmark: factor settings and measured dimensions (mm), steps and holes.

Run	P_c	v_c	δ	Step1 Side A	Step2 Side A	Step3 Side A	Step4 Side A	Step1 Side B	Step2 Side B	Step3 Side B	Step4 Side B	Hole Ø2	Hole Ø3	Hole Ø4
CB_S_1	170	200	0.10	3.077	2.992	3.078	2.992	3.012	3.005	3.020	3.052	1.678	2.801	3.646
CB_S_2	150	350	0.07	3.039	2.910	2.909	3.039	2.906	2.992	2.994	3.034	1.936	2.811	3.790
CB_S_3	150	350	0.07	3.027	3.051	3.015	2.988	2.941	2.982	2.925	3.012	1.859	2.849	3.765
CB_S_4	130	500	0.04	2.900	2.861	2.971	2.932	2.857	2.990	2.963	2.963	1.897	2.831	3.886
CB_S_5	170	500	0.10	3.050	2.955	2.932	3.003	2.925	2.983	2.953	2.983	1.727	2.732	3.609
CB_S_6	170	500	0.04	2.987	3.004	2.912	2.997	2.809	3.026	3.002	2.947	1.901	2.938	3.892
CB_S_7	170	200	0.04	2.990	2.970	3.011	3.090	2.836	2.982	2.947	2.953	1.844	2.864	3.748
CB_S_8	130	200	0.04	2.992	3.035	2.970	3.050	2.963	3.017	2.937	2.957	1.699	2.537	3.665
CB_S_9	150	350	0.07	3.013	3.034	3.056	2.949	2.953	2.925	2.959	3.017	1.851	2.872	3.875
CB_S_10	130	500	0.10	3.016	3.016	3.085	2.963	2.990	2.998	3.042	2.990	1.874	2.736	3.721
CB_S_11	130	200	0.10	2.991	3.013	2.992	3.007	2.884	2.928	3.025	2.938	1.914	2.851	3.740

Table B.10: Cube benchmark: factor settings and measured dimensions (mm), notches and slot lengths.

Run	P_c	v_c	δ	NI Width	NI Depth	NII Width	NII Depth	NIII Width	NIII Depth	NIV Width	NIV Depth	NII Length	NI Length	NIII Length	NIV Length
CB_S_1	170	200	0.10	2.684	0.982	0.699	3.030	0.458	5.667	0.528	3.023	3.850	5.631	2.440	3.812
CB_S_2	150	350	0.07	2.901	0.983	0.552	2.947	0.556	5.565	0.625	2.988	3.979	5.659	2.506	3.928
CB_S_3	150	350	0.07	2.824	1.012	0.648	3.038	0.690	5.643	0.705	3.036	3.917	5.727	2.513	3.949
CB_S_4	130	500	0.04	2.872	0.953	0.752	2.912	0.650	5.621	0.801	2.937	3.962	5.975	2.536	4.017
CB_S_5	170	500	0.10	2.755	0.918	0.587	2.962	0.556	5.633	0.653	3.023	3.861	5.744	2.454	3.866
CB_S_6	170	500	0.04	2.769	1.031	0.701	2.938	0.599	5.575	0.872	2.953	3.982	5.833	2.593	4.005

continued

Table B.10 – continued

Run	P_c	v_c	δ	NI Width	NI Depth	NII Width	NII Depth	NIII Width	NIII Depth	NIV Width	NIV Depth	NII Length	NI Length	NIII Length	NIV Length
CB_S_7	170	200	0.04	2.844	0.957	0.641	2.921	0.559	5.551	0.630	3.004	4.028	5.764	2.559	3.902
CB_S_8	130	200	0.04	2.683	1.076	0.592	3.024	0.509	5.579	0.542	2.970	3.866	5.850	2.429	3.871
CB_S_9	150	350	0.07	2.639	1.083	0.649	2.991	0.599	5.678	0.687	2.977	3.986	5.903	2.547	3.936
CB_S_10	130	500	0.10	2.900	0.965	0.590	2.992	0.590	5.642	0.530	2.930	3.912	5.682	2.479	3.875
CB_S_11	130	200	0.10	2.747	1.045	0.478	3.106	0.530	5.674	0.669	2.989	3.984	5.892	2.555	3.966

Table B.11: Cube benchmark: factor settings and measured dimensions (mm), bores and fillets.

Run	P_c	v_c	δ	Bore Ø3	Fillet Ø2 (a)	Fillet Ø2 (b)	Hole Ø0.5	Hole Ø1	Hole Ø2	Hole Ø4	Fillet Ø6 (a)	Fillet Ø6 (b)
CB_S_1	170	200	0.10	2.910	2.095	1.962	0.308	0.742	1.702	3.828	5.699	5.834
CB_S_2	150	350	0.07	3.046	1.895	1.951	0.353	0.768	1.944	3.882	5.540	5.778
CB_S_3	150	350	0.07	3.061	1.830	1.873	0.360	0.799	1.797	3.868	5.781	5.607
CB_S_4	130	500	0.04	3.075	1.980	1.809	0.401	0.885	1.922	3.869	5.642	5.419
CB_S_5	170	500	0.10	2.964	1.999	2.014	0.323	0.788	1.946	3.823	5.820	5.679
CB_S_6	170	500	0.04	3.075	1.660	1.700	0.325	0.888	1.943	3.931	5.580	5.647
CB_S_7	170	200	0.04	3.085	1.917	1.724	0.222	0.731	1.824	3.816	6.031	5.491
CB_S_8	130	200	0.04	2.972	2.076	2.062	0.229	0.750	1.734	3.730	5.417	5.533
CB_S_9	150	350	0.07	3.030	2.062	2.056	0.302	0.807	1.835	3.754	5.586	5.749
CB_S_10	130	500	0.10	2.914	1.877	1.845	0.262	0.793	1.811	3.856	5.548	5.567
CB_S_11	130	200	0.10	3.058	1.865	1.957	0.291	0.796	1.861	3.919	5.680	5.498

B.2.7 Cylinder matrix (CY)

Table B.12: Cylinder matrix: factor settings and measured outer and inner diameters (mm).

Run	P_c	v_c	δ	A - OD	A - ID	B - OD	B - ID	C - OD	C - ID	D - OD	D - ID	E - OD	E - ID
CY 1	170	200	0.04	3.968	3.417	2.989	0.410	2.075	1.600	0.941	0.431	5.003	3.934
CY 2	150	350	0.07	3.884	3.534	2.901	0.530	1.960	1.704	0.905	0.575	4.918	4.023
CY 3	150	350	0.07	3.922	3.530	2.908	0.624	2.005	1.715	0.930	0.565	4.918	4.036
CY 4	130	500	0.10	3.807	3.564	2.824	0.614	1.926	1.739	0.825	0.592	4.809	4.113
CY 5	170	500	0.04	3.918	3.465	2.961	0.467	2.034	1.718	0.946	0.462	4.954	3.975
CY 6	170	500	0.10	3.785	3.529	2.823	0.564	1.923	1.735	0.861	0.525	4.848	4.126
CY 7	170	200	0.10	3.871	3.503	2.828	0.540	1.943	1.622	0.948	0.000	4.875	4.099
CY 8	130	200	0.04	3.943	3.440	3.021	0.485	2.067	1.708	0.970	0.489	5.006	3.945
CY 9	150	350	0.07	3.874	3.529	2.909	0.565	1.966	1.717	0.940	0.542	4.894	4.059
CY 10	130	500	0.04	3.926	3.451	2.931	0.378	1.985	1.718	0.911	0.335	4.953	3.970
CY 11	130	200	0.10	3.818	3.516	2.876	0.526	1.983	1.643	0.981	0.413	4.850	4.021
Nominal	–	–	–	4.00	3.50	3.00	0.50	2.00	1.75	1.00	0.50	5.00	4.00

Table B.13: Overhang struts: down-skin border parameters.

Specimen	P_c (W)	v_c (mm/s)	δ (mm)
OH_1	80	1200	0.10
OH_2	120	800	0.10
OH_3	100	1000	0.07
OH_4	80	1200	0.04
OH_5	100	1000	0.07
OH_6	120	800	0.04
OH_7	80	800	0.04
OH_8	120	1200	0.10
OH_9	80	800	0.10
OH_10	120	1200	0.04
OH_11	100	1000	0.07

B.2.8 Confocal surface measurement data

Table B.14: Upper tie plate: confocal areal surface parameters, with the factor settings of each measured run.

Sample	Surface	P_c	v_c	δ	n_b	S_a	S_z	S_{10z}	S_{dr}	S_{sk}
UT18	Wall	150	350	0.07	2	7.47	92.6	82.1	29.9	1.371
UT19	Wall	130	200	0.10	2	7.29	91.9	76.3	18.3	1.269
UT21	Wall	150	350	0.07	1	9.63	148.2	108.6	34.2	0.648
UT22	Wall	170	200	0.04	2	8.03	80.0	73.2	20.8	0.860
UT26	Wall	150	500	0.07	1	10.41	121.0	104.4	34.9	0.843
UT18	Bore ID	150	350	0.07	2	10.08	154.2	107.5	39.1	1.144
UT19	Bore ID	130	200	0.10	2	11.01	129.9	91.2	24.9	0.380
UT21	Bore ID	150	350	0.07	1	10.05	194.5	141.2	44.4	1.027
UT22	Bore ID	170	200	0.04	2	9.68	102.9	78.5	23.6	0.746
UT26	Bore ID	150	500	0.07	1	11.53	149.2	121.3	39.6	0.860

Table B.15: Thin walls: confocal areal surface parameters for each of the six wall thicknesses on five measured coupons.

Sample	Wall	P_c	v_c	δ	n_b	S_a	S_z	S_{10z}	S_{dr}	S_{sk}
TW1	0.5	130	500	0.04	1	12.69	149.7	128.6	54.0	0.477
TW1	0.7	130	500	0.04	1	13.65	188.3	159.7	50.0	0.466
TW1	0.9	130	500	0.04	1	13.99	170.6	142.2	61.3	0.178
TW1	1.1	130	500	0.04	1	14.17	193.9	159.5	54.5	0.042
TW1	1.3	130	500	0.04	1	14.22	224.4	189.9	60.9	−0.488
TW1	1.5	130	500	0.04	1	14.58	247.9	208.7	69.3	0.186
TW11	0.5	130	500	0.10	2	12.42	215.7	164.0	54.3	−0.371
TW11	0.7	130	500	0.10	2	14.26	238.9	206.0	67.8	0.497
TW11	0.9	130	500	0.10	2	12.86	179.6	126.8	57.9	0.647
TW11	1.1	130	500	0.10	2	13.56	246.2	221.9	60.3	−0.631
TW11	1.3	130	500	0.10	2	12.20	213.6	168.2	50.2	0.169
TW11	1.5	130	500	0.10	2	14.91	232.2	196.7	62.1	−0.082
TW15	0.5	170	200	0.04	2	7.19	184.5	110.2	27.6	1.542
TW15	0.7	170	200	0.04	2	7.22	75.1	70.2	26.1	0.765
TW15	0.9	170	200	0.04	2	7.08	79.7	65.9	26.6	0.733
TW15	1.1	170	200	0.04	2	7.79	94.8	73.9	30.0	0.960

continued

Table B.15 – continued

Sample	Wall	P_c	v_c	δ	n_b	S_a	S_z	S_{10z}	S_{dr}	S_{sk}
TW15	1.3	170	200	0.04	2	7.91	79.4	71.9	31.4	0.836
TW15	1.5	170	200	0.04	2	7.46	103.3	74.7	24.0	0.473
TW20	0.5	150	350	0.04	1	8.24	104.3	87.9	34.4	0.826
TW20	0.7	150	350	0.04	1	7.85	81.0	74.1	31.0	0.720
TW20	0.9	150	350	0.04	1	8.46	127.1	90.7	33.6	0.912
TW20	1.1	150	350	0.04	1	8.87	109.4	94.2	38.1	0.877
TW20	1.3	150	350	0.04	1	9.49	128.3	102.3	43.0	0.722
TW20	1.5	150	350	0.04	1	7.49	121.6	95.2	36.4	0.924
TW21	0.5	150	350	0.07	1	8.58	105.7	89.9	38.5	0.864
TW21	0.7	150	350	0.07	1	7.78	112.4	81.8	35.5	0.901
TW21	0.9	150	350	0.07	1	7.59	86.8	76.7	35.0	0.956
TW21	1.1	150	350	0.07	1	8.96	141.9	116.5	37.4	0.775
TW21	1.3	150	350	0.07	1	8.47	118.3	98.9	37.6	0.822
TW21	1.5	150	350	0.07	1	8.41	106.3	91.5	36.2	0.714

Table B.16: Overhang struts: confocal areal surface parameters on the down-skin surface.

Specimen	S_a	S_z	S_{10z}	S_{sk}
OH 1	30.40	254.2	230.2	0.314
OH 2	26.95	256.3	225.0	0.144
OH 3	27.81	264.8	245.3	0.286
OH 4	26.18	250.2	223.3	0.118
OH 5	28.81	246.2	230.5	−0.139
OH 6	33.69	289.6	258.8	−0.163
OH 7	33.02	288.9	263.9	−0.068
OH 8	27.55	247.1	220.8	0.071
OH 9	26.12	248.0	235.2	0.075
OH 10	31.06	266.4	248.6	0.055
OH 11	27.25	267.5	243.6	0.136

DEPARTMENT OF INDUSTRIAL AND MATERIALS SCIENCE
CHALMERS UNIVERSITY OF TECHNOLOGY
Gothenburg, Sweden
www.chalmers.se



CHALMERS
UNIVERSITY OF TECHNOLOGY